Los Alamos National Laboratory is operated by the University of California for the United States Department of Energy under contract W-7405-ENG-36.

Laser Shock Wave Generation, Propagation, and Interactions in Low Pressure Air

Los Alamos
Los Alamos National Laboratory
Los Alamos, New Mexico 87545

This thesis was accepted by the University of Colorado, Boulder, Colorado, Department of Physics, in partial fulfillment of the requirements for the degree of Doctor of Philosophy. It is the independent work of the author and has not been edited by the Technical Information staff.

This work was supported by the Northwest College and University Association for Science (NORCUS).

LA-9182-T
Thesis

UC-34
Issued: February 1982

Laser Shock Wave Generation, Propagation and Interactions in Low Pressure Air

Mark David Wilke

Los Alamos National Laboratory
Los Alamos, New Mexico 87545

TABLE OF CONTENTS

LIST OF FIGURES AND ILLUSTRATIONS

LASER SHOCK WAVE GENERATION, PROPAGATION, AND INTERACTIONS IN LOW PRESSURE AIR

by

Mark David Wilke

ABSTRACT

Strong spherical shock waves were generated in 1 to 50 torr air by irradiating 3.4-μg plastic-shell targets with 5 to 30 J, 300 psec Nd:glass laser pulses. The shock wave trajectories were measured with an electrostatic framing camera during the luminous phase and a shadowgraphy system during the nonluminous phase. A holographic, two-wavelength interferometer obtained both trajectory information and fringe patterns which, after Abel inversion, yielded electron and gas density profiles. The data taken during the early expansion when the target mass has a significant effect were compared with existing analytical calculations and with numerical calculations. A description of the early expansion is given, in which the target mass is taken to be an isentropically expanding gas that supplies energy to a variable-energy blast wave in the surrounding air. The description is consistent with the numerical calculations and not inconsistent with the data. Two-dimensional experiments were conducted by reflecting the spherical shock wave from a plane and by allowing two near-identical shocks to collide. The two-dimensional results are compared to a scaled nuclear shock and to two-dimensional numerical calculations.

INTRODUCTION

This thesis investigates the formation, propagation, and interaction of strong spherical shock waves in low-pressure air. The shocks were produced by high-power laser irradiation of microshell targets. The investigation includes single spherical shock waves, the compound shocks produced by reflection from a plane, and the interaction of two nearly identical shock waves. The majority of the data were taken in air at pressures of 1 and 50 torr. The hollow-shell plastic $(CH)_n$ targets had a mass of ~ 3.4 μg each and were irradiated by a 300-ps Nd:glass laser pulse with energies of ~ 5 to 30 J.

The one-dimensional and two-dimensional shock wave experiments are interrelated because the shock interaction investigations require an understanding of the structure of the individual shock waves during the period of time when the interactions are to take place. This understanding includes measuring peak gas densities and electron number densities. The density measurements are of special interest because, in previous experiments, there is a lack of agreement between measured densities and theoretically or numerically calculated densities.

The formation of the laser shock waves from the target plasma is also of interest in this thesis. There appears to be little previous information regarding this phase of the shock wave propagation for experiments using subnanosecond pulses and microgram targets.

Measurements were made with a variety of plasma and gas-dynamic techniques. High-speed electrostatic framing cameras were used to photograph the luminous shock and plasma at times as early as 50 ns after the Nd:glass laser pulse. Multiple-frame shadowgraphy photographs were taken during the period of time 1 to 30 μs after irradiation. The most detailed diagnostics were obtained with a two-wavelength ruby-laser holographic interferometer that recorded single holographic images at predetermined times. Measurements of maximum particle velocities in vacuum were also made, using ion detectors.

The photographs, shadowgraphs, and interferograms provided radius-vs-time data which were used to determine the energy content of the shock wave during the blast-wave phase of expansion for comparison with the laser energy that initiated it. The interferogram fringe patterns were digitized and inverted to determine the gas density and electron number density behind the shock.

An Abel inversion technique was developed and tested for best possible applicability to the type of interferometric data obtained. The method was found to give good results when compared with other techniques.

The early radius-vs-time data have been compared with a variety of analytical approximations and self-similar fluid solutions to facilitate understanding of the early expansion.

A pre-existing finite-difference Lagrangian hydrodynamic computer code was also used to simulate the experiments. The code already included radiation transport, and for these simulations it was modified to include electron heat transport.

Shock interaction experiments were carried out to investigate two-dimensional shock structures such as Mach stems. Scaling relations were used to compare the laser experiments with two-dimensional nuclear shock data. The experiments were also modeled, using an existing two-dimensional hydrodynamics code.

Interest in the type of self-similar fluid motion generated by a near-instantaneous, near-point release of energy or blast wave began in the early 1940s in conjunction with efforts to develop the atomic bomb. Self-similar motions (which are discussed more fully in later chapters) have the property that plots of a given flow variable at different times can be made identical by multiplying the axis by time-dependent values. G. I. Taylor and J. von Neumann were both approached with the problem and they presented their solutions nearly simultaneously (June 27, 1941 and June 30, 1941, respectively). Both solutions remained classified for several years, during which time Sedov [see Sedov (1959)] independently arrived at the same solution. Taylor's work was later published [Taylor (1950)], and von Neumann's appears in Bethe (1958). For self-similar fluid motion, the partial differential equations that describe spherically symmetric, inviscid, adiabatic flow convert to ordinary differential equations that can be integrated. One of the conditions of the conversion is that the shock radius be given by $R_s = At^{\alpha}$ where A is a dimensional constant, α is a number, and t is the time. The form of A and value of α can be determined from the dimensional constants describing the problem.

The Taylor-von Neumann-Sedov (TVS) solution is based on the dimensional relation $E_s = \xi(\gamma)\rho_o R_s^5/t^2$ where E_s is the energy

released in an ambient atmosphere of density ρ_0. The dimensionless variable $\xi(\gamma)$, a function of the specific heat ratio γ, is ~ 1. This relation has been shown to be a good approximation for nuclear shock waves [Glasstone (1962)] and to some extent for high-explosive shock waves [Baker (1973)].

The TVS instantaneous point source solution is a special case of a large class of self-similar motions partially investigated by Freeman (1968) where, in general, the energy is supplied to the shock front with a power-law dependence on time. These solutions are discussed in Chapter IV. The time dependence of the shock-wave energy is given by $E_s \propto t^{\beta}$, where $\beta = 0$ for the TVS solution. The general relation between β and α is $\alpha = (\beta + 2)/5$. Other special cases of variable-energy self-similar blast waves that have been studied include the shock formation in a circumstellar medium by a strong stellar wind where $\beta = 1$ [Avedisova (1972)] and in the air surrounding a uniformly expanding sphere where $\beta = 3$ [Taylor [1946)].

Several approximate expressions have been obtained for the case of spherical fluid motion from an instantaneous point-energy release. Chernyi [see Zel'dovich and Raizer (1967)] and Bethe (1958) developed similar approximate solutions by assuming the ambient air is swept up in a thin shell. Bethe's method of approximation can be extended to obtain approximate solutions for non-ideal situations exemplified by Fuchs' (1958) inclusion of source mass, which is described in Appendix C.

Early experimental observations of self-similar spherical shock expansions consist mainly of nuclear shock-wave data [Glasstone

(1962)] where the expansion is described very well by the TVS solution. These observations show that the TVS solution accurately describes the expansion for some period of time regardless of non-ideal initial conditions that may include much source mass from the crater and tower debris, and the extended source energy of the isothermal sphere, which does not represent a point energy release. TVS shock waves will result from non-instantaneous energy releases if the time and radius of energy deposition are small compared to the time and radius at which the shock expansion is observed.

Many experiments have now been performed using lasers as an energy source [see Hughes (1975) for a review] that indicate the laser-initiated fluid motion goes through a period of self-similar expansion where $R_s \propto t^{2/5}$. Again, the eventual $\alpha = 2/5$ expansion applies for a variety of initial conditions. Basov et al (1973) and Leonard and Mayer (1975) used this fact to determine laser-target coupling in fusion experiments by measuring $R_s(t)$ and relating it to E_s. In both cases, the influence of target mass on the early expansion was suggested, and Basov et al further suggest a possible influence from electron heat transport.

The capability of conveniently producing strong spherical shocks in the laboratory and of measuring not only $R_s(t)$ but also density profiles provides a research tool for spherical experiments that complements planar shock studies done with shock tubes. It may also be possible to study astrophysical problems as well as phenomena previously investigated only with high explosives and nuclear tests. For example, Barasch, Stone, and Wilke [see Wilke and Stone (1979)] demonstrated the use of laser-generated shocks for two-dimensional

shock-wave interaction studies previously done with high explosives [Dewey, McMillin, and Classen (1977)]. Properties of the laser-initiated shocks are also of interest for applications in inertial confinement fusion development. Booth et al. (1976), for instance, suggested the use of a "buffer" gas in the reactor chamber to protect the walls.

Although many measurements of the electron number density profiles and gas density profiles have been made, comparisons with calculations are typically not good. For example, Director (1975) and Guenther et al (1973) showed agreement in shape but not magnitude of the profiles. The discrepancies probably resulted from their method of Abel inversion [Pikalov and Preobrazhenskii (1974)].

Except for the Basov et al and Leonard and Mayer references for experiments with pulse lengths $\lesssim$ 1 ns, there is little information on the initial post-pulse expansion, when $\alpha > 2/5$. There have been investigations of the expansion of plasmas resulting from finite-length laser pulses focused in gases, where the plasma dimensions were measured during and after the pulse. Ramsden and Savic (1964) showed that the front toward the laser expands as a detonation wave ($\alpha = 3/5$) during the pulse. Director (1975) pulsed a target many times to simulate the $E_s \propto t$ ($\beta = 1$) situation. He found $\alpha \simeq 3/5$, as predicted by Freeman's theoretical result. More applicable to this thesis is Dabora's (1972) consideration of the results of Hall (1969). A 20-ns, 0.5-J ruby-laser pulse was focused onto a tantalum slab in ~ 1 torr of argon to produce a hemispherical blast wave. Hall found relationships between ρ_0, E_s, R_s, and t for $t < 1$ μs in reasonable agreement with the TVS solution. Dabora found even

better agreement was possible if he assumed the tantalum target continued to supply energy to the shock front after the laser pulse ended, with a $\beta = 0.1$ time dependence. Lampis and Brown (1968) observed periods during the early expansion of laser sparks where $\alpha \neq 2/5$. They attributed the $\alpha \neq 2/5$ expansion to geometrical effects. Finally, Leonard and Hammerling (private communication) compared the data of Leonard and Mayer with the approximate thin-shell theory of Freiwald and Axford (1975) that includes the source mass. The agreement is not very good.

The subject of two-dimensional planar-shock interactions has been extensively investigated, both experimentally and theoretically, by Ben-Dor (1968). Two-dimensional spherical shock interaction data exist for reflected nuclear shocks (Glasstone), but so far no convenient way has been developed to study interactions of strong spherical shock waves on a small scale.

The first chapter of this thesis describes the experiments and the diagnostics. Chapter II describes the measurement of radius-vs-time and how the shock energy is assigned based on the radius measurements at times when the data indicate $\alpha = 2/5$. Chapter III describes the interferometry method and compares the results with analytical predictions. Chapter IV considers the early expansion in analytical terms. A variable-energy blast wave interpretation of the data is suggested and qualitatively examined. Chapter V describes the one-dimensional computer modeling and compares model results with the data. Chapter VI describes the two-dimensional experiments. The results are scaled and compared with an equivalent nuclear shock. Modeling, using an existing two-dimensional code, is

described and the results are compared with the data. Appendices are included for description of the experimental design, the Abel-inversion formulation, and Fuch's solution.

CHAPTER I

EXPERIMENTAL APPARATUS AND PROCEDURE

This thesis deals with both individual spherical laser-generated shocks and two-dimensional laser-generated shock waves. The two-dimensional shock waves were generated by reflecting individual shocks off a plane surface, or by allowing two simultaneous laser shocks to collide. The techniques and overall diagnostic geometry were selected for their applicability to both single and double shock experiments. A single method of shock generation, as well as a standard diagnostic system, facilitated comparison of the one- and two-dimensional data.

Shock Wave Generation

The shock waves were generated by irradiating spherical shell targets with a high-power laser. The targets were mounted in a vacuum chamber that was first evacuated to < 0.1-torr pressure, then backfilled with dry air to the desired pressure (usually 1 or 50 torr). The chamber air was allowed to reach room temperature before each shot. The chamber was evacuated to $\sim 1 \times 10^{-5}$ torr with no backfill when ion time-of-flight measurements were made.

The Laser

The Los Alamos Scientific Laboratory (LASL) Nd:glass laser was used to irradiate the targets. The laser's current configuration consists of a single front-end beam, which is split into two beams that are amplified and expanded to produce 30- to 40-J maximum energy output per 86-mm beam. One beam was used to generate an individual shock wave, reserving the second beam for the double-shock experiments. Figure I-1a shows the diagnostic geometry and the alignment of the output beams with the targets for a double shock-wave experiment. To investigate reflected shocks, an 8x8x4-cm clear acrylic plastic block was supported 0.9 cm above the target. The faces of the block were aligned parallel and perpendicular to the interferometer "scene" beam in Fig. I-1a. The final beam focusing was done with ~ f/4, 10-cm diameter aspheric lenses and was essentially diffraction limited; however, the laser-beam divergence resulted in $\simeq$ 100-μm spot sizes.

The laser pulse was generated in a passive mode-locked cavity. A single pulse was extracted from the resulting pulse train using a Pockells cell. Pulse length was selectable from 70 ps to 1 ns by using different cavity etalons. I chose 300-ps pulse lengths exclusively for this experiment. They have the highest successful pulse yield (~ 70%) and lowest multipulse production, and they permit higher total energy outputs than 70-ps pulses. Moreover, numerical modeling showed little hydrodynamic motion prior to 300 ps, thus permitting the assumption that the energy is deposited instantaneously.

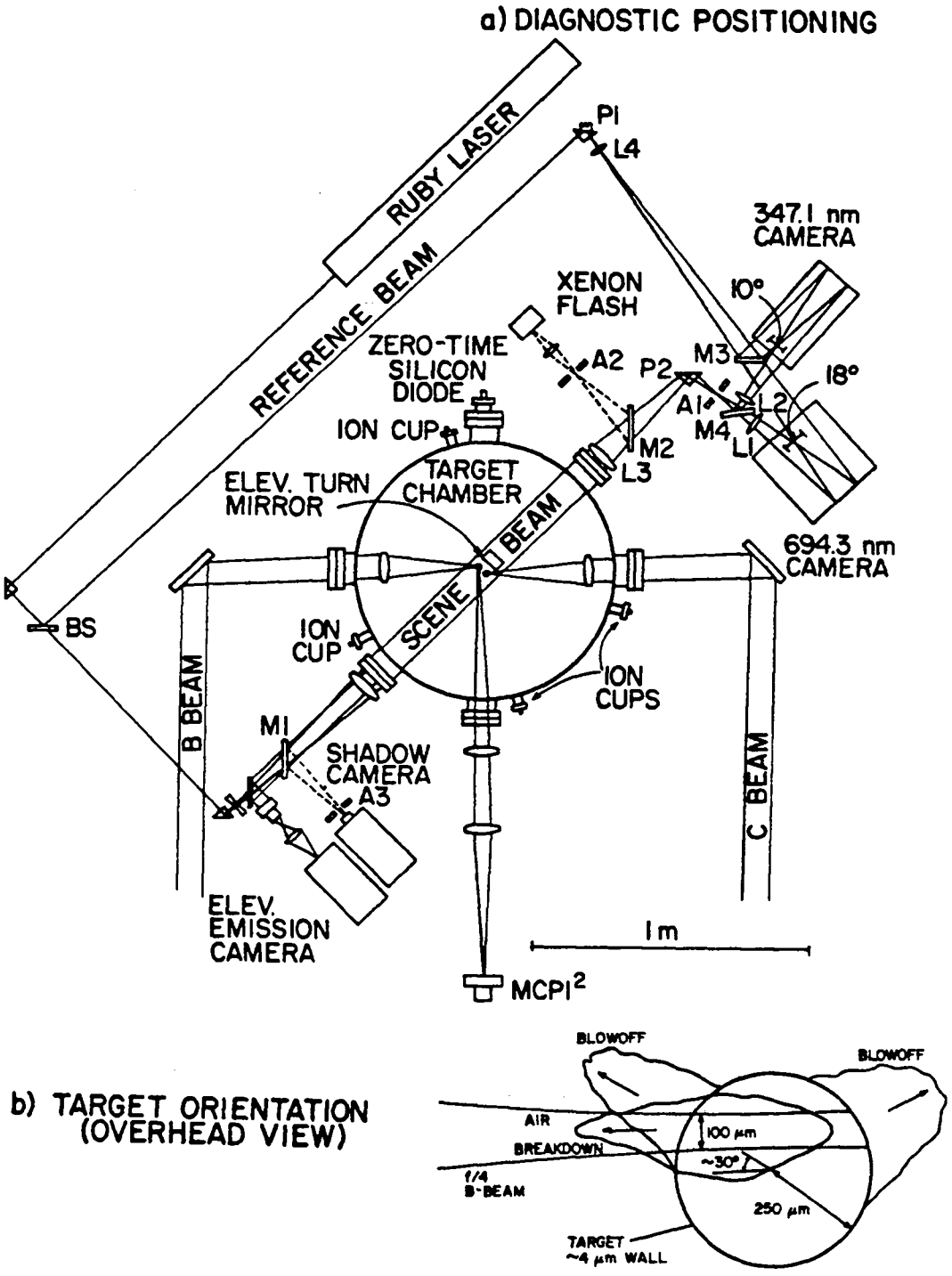

Fig. I-1. (a) Schematic layout of diagnostics and beam alignment for a double-shock experiment.

(b) Overhead view of B-target, showing irradiation scheme.

Calorimeters monitoring a fraction of each beam provided laser pulse energy measurements. The final output measurement was good to the larger of 10% or 1 J. The variation (due to electrical noise) was random. Both the oscillator-cavity pulse train and the switched-out pulse were monitored with high-speed silicon diodes to check for double pulses. The degree of focus was occasionally monitored by splitting off a fraction of the output beam, which was again split into equal parts. Each equal part was passed through a long focal-length lens and a different sized aperture. Calorimetry measurements of the throughputs determined the beam fraction within a given spot size. Degradation of the laser focusing could be checked by noting the oscillator-pulse spot size in the target-alignment microscope. The irradiances calculated from the measured pulse lengths, spot sizes, and maximum pulse energies were $\simeq 1 \times 10^{15}$ W/cm^2.

The Targets

Targets were provided by the Los Alamos target fabrication group (L-7). The targets were composed of polymerized para-xylene $(C_8H_8)_n$, with a density of 1.18 g/cm^3. Hollow spherical shells with 500 $\pm$ 25-μm diameters and 4 $\pm$ 0.5-μm thick walls were used. The mass was taken to be 3.4 μg. The shells were epoxied onto 10-μm glass stalks drawn from 2-mm OD, 0.7-mm ID glass tubing. The mass of the stalk tip is $\sim 1.6 \times 10^{-7}$ g/mm.

The hollow-shell targets were irradiated with a single laser beam, focused on the near side of the target. Some asphericity in shape and optical emission of the early plasmas occurred because of

"blowoff" outward from the front and back walls and from air breakdown. A sizeable fraction of the beam passed through the target, presumably before the plasma reached the critical electron density. This was indicated by burn marks on "footprint" paper at the opposite side of the chamber from the focusing lens.

The targets were irradiated ~ 30^{o} off center with respect to the laser beam. Irradiating the target along a chord permits differentiation between blowoff and beam-aligned air breakdown. The irradiation geometry for a B-beam shock wave experiment is shown in the overhead view of Fig. I-1b. The targets were irradiated along a similar chord on the opposite side for the ion measurements.

Diagnostic Systems

Figure I-1a shows the general layout of the diagnostic system. The schematic for the shadowgraphy and interferometry optical system are shown in Fig. I-2.

Jitter-free triggering of the electronic components and monitoring oscilloscopes was obtained by directly observing the laser oscillator output. A fraction of the oscillator output beam is split off, amplified, and sent directly to the target room, where it is detected by a high-speed silicon diode [McCall (1972)]. The diode provides a fast rise-time voltage trigger pulse which is used as a pre-trigger 200 ns before the main beam strikes the target. The trigger voltage pulse is split; and additional delays, when desired, were added for each instrument.

Zero-time is defined by the voltage pulse generated by another high-speed silicon detector that observes the laser light scattered

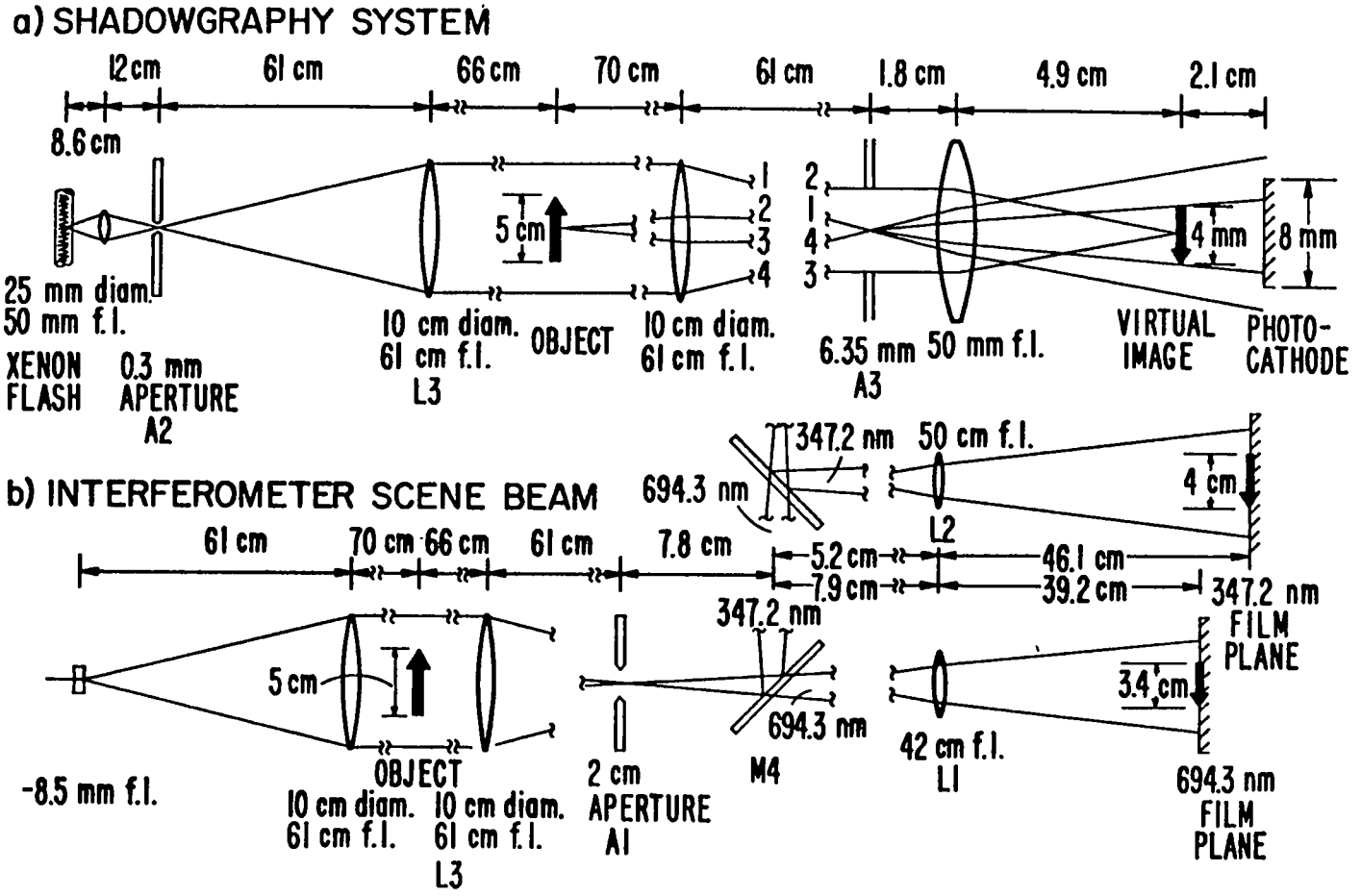

Fig. I-2. Optical layout of (a) shadowgraphy system, and (b) holographic interferometer scene beam.

from the target plasma. The pulse is supplied to the various oscilloscopes for a reference marker. The timing of the emission exposures, shadowgraphs, and interferograms is described in Chapter II.

Interferometer

The holographic interferometer is similar to that used by Jahoda and Siemon (1972), in which the object of study (in this case a shock wave) is imaged on the photographic plate. The interferometer may be operated in one of two modes: by itself at two wavelengths (694.3 and 347.2 nm), or with the shadowgraphy system at 694.3 nm only, by inserting mirrors M1 and M2. A single exposure (or simultaneous pair of exposures, if the two-wavelength mode is used) is taken of each shock wave at a selected time from 428 ns to 30 μs after target irradiation.

The ruby laser produces a 15-ns, 10-mJ pulse 1.5 mm in diameter in the lowest order transverse electromagnetic (TEM_{00}) mode. A temperature-tuned doubling crystal converts about 10% of the energy to 347.2-nm light. Beam-splitter BS is coated to reflect ~ 30% at each of the cross-polarized wavelengths for use as reference beams. In the two-wavelength mode, mirrors M1 and M2 are removed and both the 347.2 nm and 694.3 nm beams (scene beams) pass through the chamber. Lens L3 is used to project the target-plasma emitted light into a near-parallel beam and to focus the interferometer light through the 2-cm aperture, A1. The majority of the target light is blocked by the aperture so that it will not cause noise on the hologram. The calculation in Appendix A confirms that the apertures are large

enough not to block interferometer rays refracted through the shock. Mirrors M4 and M3 reflect near-uv light and pass red, therefore separating the 694.3- and 347.2-nm beams. The target is focused on the photographic plates by lenses L1 and L2 to yield 0.67X magnification for the red and 0.8X magnification for the uv images. All components that the 347.2-nm beam passes through are made of fused silica.

A red filter is mounted at the entrance to the 694.3-nm camera and an ultraviolet filter at the 347.2-nm camera entrance. The filters further limit target-emitted light and permit operation of the interferometer in subdued room light. Agfa-Gaveart 10E75 4 x 5-inch plates were used to record the 694.3-nm interferograms and Kodak 125-02 4 x 5-in plates recorded the 347.2-nm interferograms.

The resolution and spatial calibration were determined from interferograms of resolution targets at the laser-target position. The resolution was found to be 50 to 100 μm at 694.3 nm and 400 μm at 347.2 nm.

The interference fringes are actually a Moire pattern resulting from the double exposure of two sets of microscopic fringe patterns with slightly different fringe spacings. The microscopic fringe structure acts as a grating between the interference fringes. This makes it possible to reproduce the interferogram in white light. The exposures are purposely heavy so that the interferograms may be reproduced in reflection, eliminating the need for plate bleaching. The plate is illuminated with a slide projector, and the first-order spectrum is intercepted by a telephoto lens, bellows, and 35-mm camera.

Interferogram timing was provided by monitoring the output at the rear of the ruby laser and comparing it to the zero-time reference pulse on an oscilloscope.

Shadowgraphy

The shadow formation in this system can be understood in terms of the virtual image formed in front of the photocathode as shown in Fig. I-2a. The shadows are equivalent to those that would be produced by the shock wave if it were at the location of the image and backlighted by the divergent beam. A detailed ray tracing, assuming an approximate shock-wave density profile, is done through the entire shadowgraphy system in Appendix A. The appendix provides information for interpretation of the shadowgraphs.

The xenon flash lamp was imaged onto a 0.3-mm aperture (A2) to provide a 17-μs pinhole backlighting source. The 6.4-mm aperture (A3) was used to limit target-emitted light.

An electrostatic framing camera (Imacon 700) was used to record ten shadowgraphs per laser shot on Royal-X pan film. Resolution has been determined in the static mode to be 0.35 mm at the shock wave. The camera was framed at 10^6 frames per second with 200-ns exposure times. Therefore, shock velocities greater than 1. to 2. x 10^5 cm/s lead to image degradation comparable to the static image resolution. The 50-torr shocks in these experiments have a velocity of typically 3 x 10^5 cm/s at 1 μs, decelerating as $t^{-0.6}$. Typical 1-torr shocks have a three times larger velocity; hence, they are difficult to resolve. The poor resolution is compounded by the weaker refraction of light by the 1-torr shock waves.

Timing is determined by monitoring the voltages on the electrostatic deflection plates within the camera that sweep the electron image of the cathode across the phosphor to form the frames. The deflection voltage is compared with the voltage pulse from the zero-time detector on an oscilloscope. The time of exposure of the frames relative to the deflection voltage was later determined by monitoring the phosphor with a high-speed photodiode and comparing the diode's output to the deflection voltage while the camera photographed a high-intensity strobe. Spatial calibration was determined from shadowgraphs of two target stalks a known distance apart.

Emission Framing Camera

The emission-framing camera is mounted above the plane containing the Nd:glass laser beams. The shock waves are viewed from above through a chamber window over the interferometer-beam entrance window via a turning mirror suspended above the targets. Magnification is varied by relative positioning of a telephoto lens and a relay lens that are used to form the image.

An Imacon 700 electrostatic framing camera was used to record the image. The S20 photocathode was protected from scattered Nd:glass laser light by an infrared blocking filter which passed the majority of the visible spectrum. For each laser shot, eight to ten frames were formed on the P11 phosphor and recorded on Royal-X pan film. The camera could be framed at rates of 2×10^7, 1×10^7, and 1×10^6 frames per second. The corresponding exposure times were 10, 20, and 200 ns. Satisfactory exposures could generally be obtained only for times earlier than about 800 ns, due to the rapidly

decreasing source radiance. There were about 90 resolution elements across the field of view. This was determined from frames of strobe back-lighted resolution targets. For a 3-cm field-of-view and a 10-ns exposure, the resolution is degraded for plasma velocities $\gtrsim 3 \times 10^6$ cm/s.

Spatial calibration was obtained from static-mode photographs of scales mounted at the target position. The timing of the frames and timing calibration was identical to the shadowgraphy timing and calibration.

Microchannel Plate Image Intensifier

An ITT F4111 18-mm pulsed microchannel plate image-intensifier ($MCPI^2$) was used to generate a high-resolution picture of the luminous phase of the target expansion. The $MCPI^2$ viewed the targets perpendicular to both the vertical stalks and the Nd:glass laser beam. The $MCPI^2$ could be operated with a maximum luminous gain of about 10,000 and was therefore used to photograph the luminous plasma at late times (~ 5 μs) as well as during the early expansion. The magnification was 1X.

The $MCPI^2$ was pulsed with an avalanche transistor pulser [Lundy et al. (1978)], resulting in 8-ns exposures. Resolution at the shock wave was ~ 0.04 mm. This was degraded, for an 8-ns exposure, by any velocity over 5×10^5 cm/s. The S25 photocathode was protected by an infrared blocking filter. Gelatin neutral-density filters and the apertures on the multi-element camera lenses were used to control the cathode exposure. It was also possible to control the luminous gain of the $MCPI^2$. The P20 phosphor image was recorded on

Panatomic-X film pressed against the channel-plate coupler on the phosphor side of the tube.

The MCPI[2] was added during the last session on the laser and it was found afterward that a faulty trigger-delay circuit caused a slow risetime pulse on the avalanche pulser input. This resulted in exposure-timing jitter of $\pm$ 100 ns. However, accurate timing can be ascertained by comparison of radii with those measured from the framing camera. Spatial resolution and calibration was determined from photos of resolution targets.

Ion Detectors

Time-of-flight measurements of the thermal ions were made using charge-cup detectors. The detectors were placed 56 cm from the target at the four positions indicated in Fig. I-1a. Each charge cup had a 0.11-cm^2 detector area. The ion detectors were capacitively coupled to oscilloscopes and were biased at -180 V. For the time-of-flight measurements, the chamber was evacuated to, typically, 10^{-5} torr.

Summary

We have described an experiment for producing and observing laser-generated one-dimensional and two-dimensional shock waves in low pressure air. The shocks are initiated by irradiating 3.4 μg, 500 μm hollow plastic spheres with a high power Nd:glass laser. A two-wavelength holographic interferometer provides radius-vs-time and gas and electron density information from 400 ns to 30 μs after shock wave initiation. A multi-frame shadowgraphy system begins

coverage at 1 μs, and emission photographs are taken as early as 50 ns with an electrostatic framing camera and a gated microchannel plate camera. Charge cups were also used for measuring maximum plasma velocities in vacuum.

Appendix A describes the computer-aided optical design of the shadowgraphy system and provides help in interpreting the shadowgraphy images.

CHAPTER II

SHOCK WAVE EXPANSION AND ENERGY MEASUREMENT

Radius Measurements

Figure II-1 shows a set of data taken for a 50-torr shock wave, including an interferogram and sets of exposures from the emission and shadowgraphy framing cameras. Figure II-2 is an emission set for a 1-torr shock. Fig. II-3 is an example of a microchannel-plate image-intensifier ($MCPI^2$) exposure of a 50-torr shock wave. Because the targets are irradiated off-axis in the horizontal plane (see Fig. I-1b) and the "blowoff" is axial, the "blowoff" from the front and back is at an angle on the framing-camera image showing a view from above. Figure II-2 shows the angle between the rear and front blowoff at 1-torr Measurements of the emission radius are made from the photographic negative by taking the diameter along the line bisecting the angle between the front and rear blowoff and dividing by two, as shown in Fig. II-2.

Radius measurements for $MCPI^2$ data were taken perpendicular to the Nd:glass beam line as indicated in Fig. II-3. Again, to determine the radii, diameters were measured from the photographic negatives and divided by two.

The bulges produced by the uneven laser illumination disappear by 900 ns for the 50-torr shock waves and 600 ns for the 1-torr shock waves. The shocks are only slightly ellipsoidal at these times and become increasingly spherical. Due to the one-sided

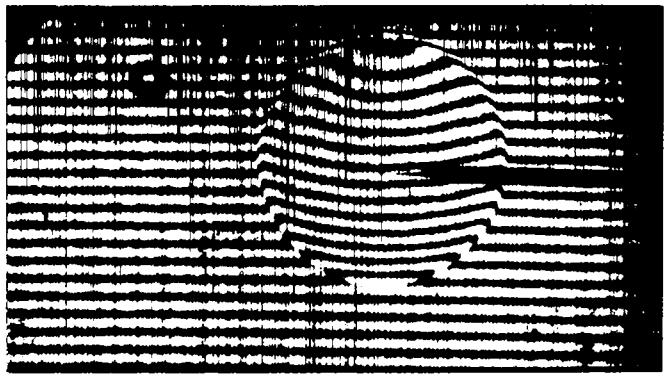

(a) Interferogram at 5.6 μs, R_s = 144 cm (stalk supported target from below).

(b) Emission framing camera result. Frames are ≈ 50 ns apart, beginning at 55 ns.

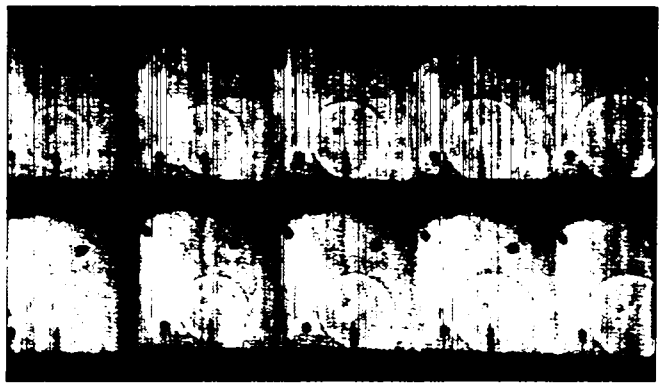

(c) Shadowgraphy framing camera result. Frames are ≈ 1 μs apart, with first exposure at 6.4 μs (B-beam from right).

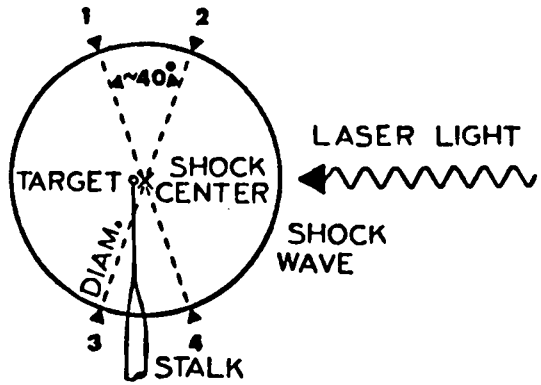

(d) Schematic showing interferometry and shadowgraphy radius measurement.

Fig. II-1. Typical 50-torr data set, E_L - 25.5 J.

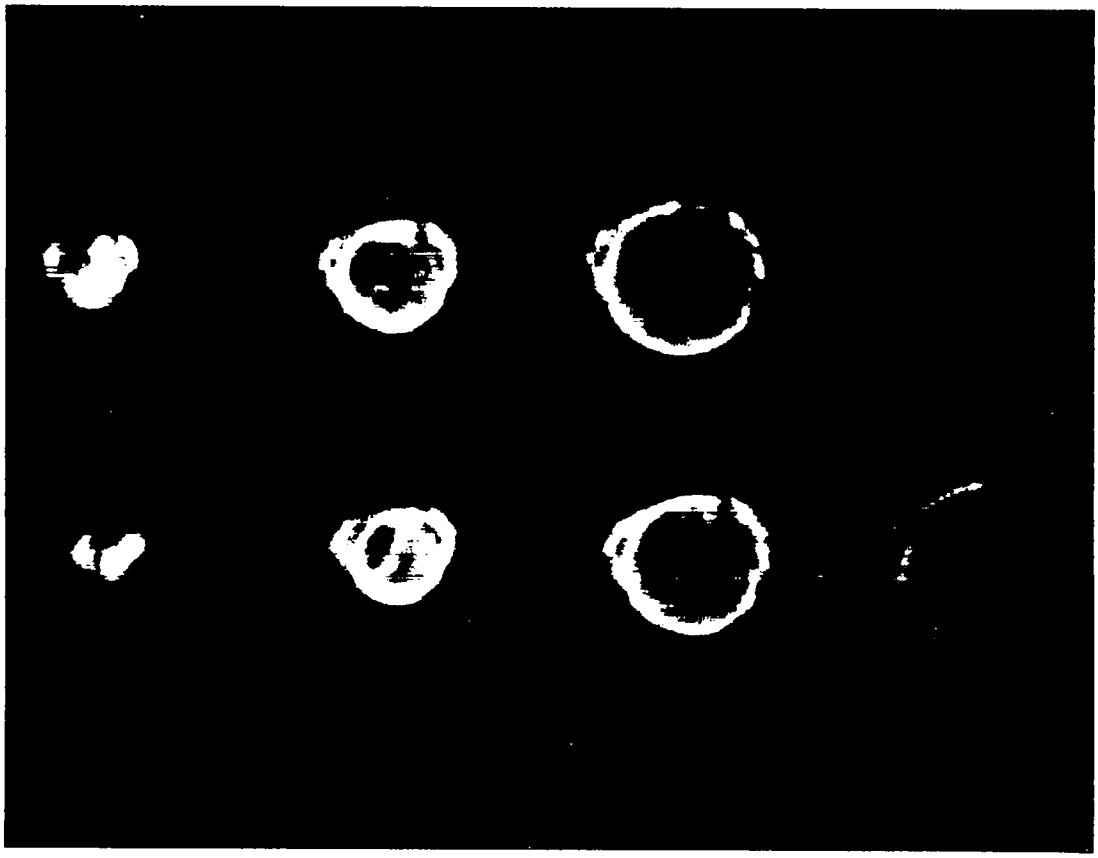

Fig. II-2. Emission framing data for 1 torr, E_L = 17 J, and schematic of diameter measurement.

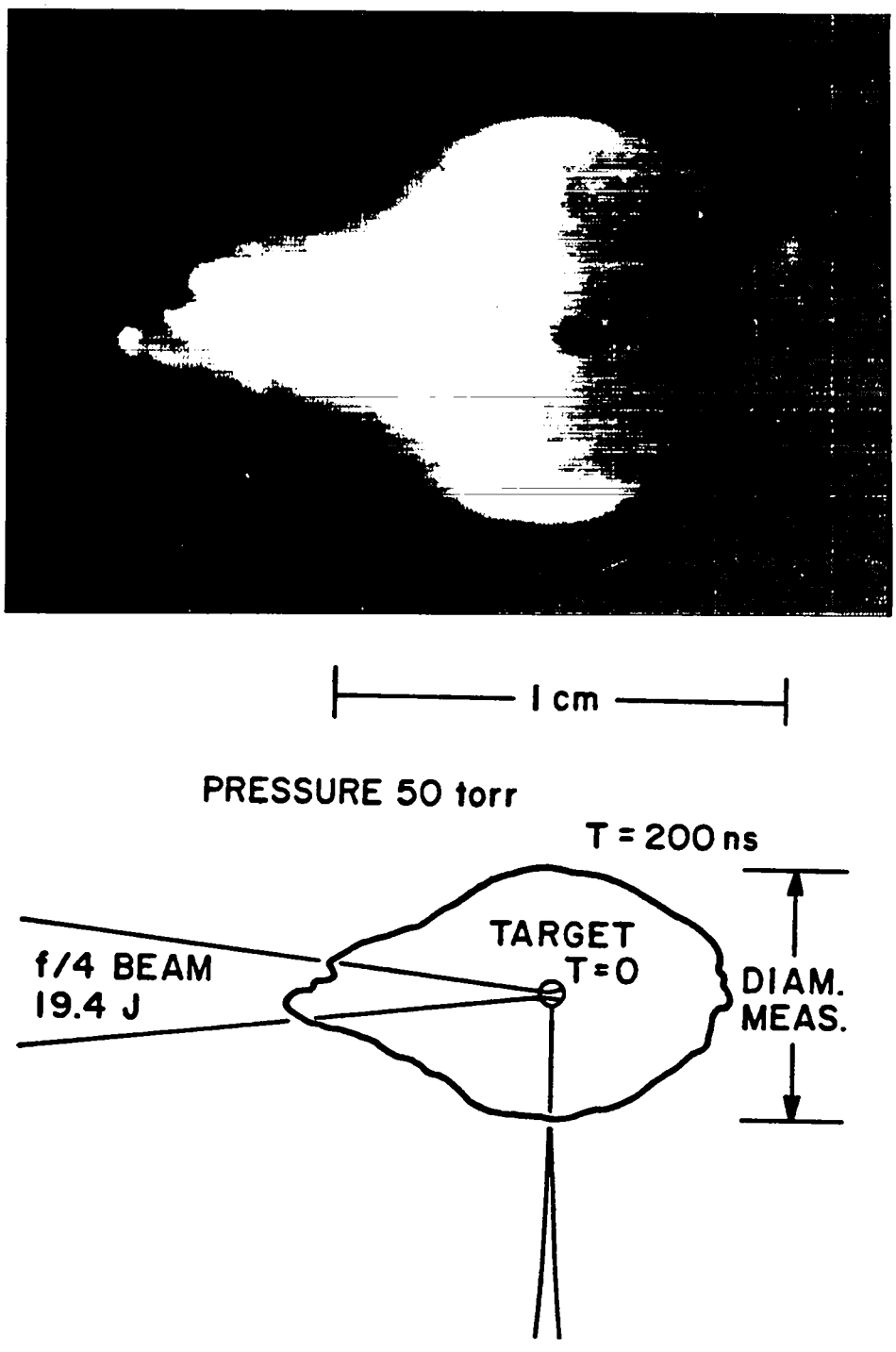

Fig. II-3. Microchannel plate image-intensifier picture and schematic of diameter measurement. Time "t = 200 ns" is highly approximate (see text).

illumination for all experiments and the slight air breakdown at 50 torr (to be discussed), the shock centers on the interferograms and shadowgraphs are slightly displaced from the target toward the Nd:glass laser. The displacement is actually greater than observed because of the 45^{o} viewing angle with respect to the Nd:glass laser beam (Fig. I-1a). The interferogram shock radii are determined by fitting circles to four points positioned on the shock boundary as shown in Fig. II-1. The digitization and fitting processes are described in Chapt. III.

The shadowgraphy radius measurements are made in a manner similar to the holographic interferogram measurements. Shadowgraphs result when light is refracted by the shock to produce an uneven illumination on the recording medium. Because of the refraction (discussed in Appendix A), it becomes difficult to determine what part of the image of a strong shock corresponds to the shock radius. For the case where the interferogram is taken during the shadowgraph sequence (true in most cases), the shadowgraph measurements give good agreement with the interferogram measurement.

Basov et al. (1976) measured the radii by relating them to the volume of ellipsoids determined from their elliptical shock images. Due to the asymmetric illumination and the ratio of the small spot size to target radius in our experiment, the lobes produced at very early times preclude the use of this technique. Our radius measurement technique must be kept in mind when comparing the data with analytical and numerical solutions assuming spherical symmetry, particularly at early times. An estimate of the error can be made by comparing the volume of a sphere with the measured radius to

the actual volume of the luminous region. The result for Fig. II-3 is 0.78. The image is most intense in the irregular areas, as would be expected from the way the target is irradiated. Therefore, it is likely that most of the energy is in the protrusions, further complicating the early expansion.

Data Reduction

1 torr

There is essentially no adjustment necessary for the 1-torr data. At low pressures (< 10 torr), the data are well-behaved and reproducible. No shadowgraphy data are available; the shock does not refract light sufficiently to give a clear image of the boundary for reliable measurement, and quickly leaves the field of view.

The emission and interferometric radius-vs-time data for $t < 1$ μs and 1-torr pressure are plotted in Fig. II-4 for several shots of varying energies.

50 torr

The 50-torr data are handled somewhat differently. The interferometric data provide by far the most accurate measurements of the shock radius during the nonluminous phase. This is true mainly because of their higher resolution and sharper image of the shock wave boundary. However, only one interferogram was taken per laser shot and comparison of radii for different shots is difficult because of a $\pm$ 10% random variation in laser energy from shot to shot. The method for overcoming this problem is explained in a following section.

There is a second problem at 50 torr. Air breakdown occurs at the laser focus and acts as a shutter, unpredictably scattering some of the laser energy. This breakdown leads to nonreproducibility in the early luminous expansion for shots of the same laser energy. For the energy ranges used in this experiment, more energy is delivered to the target-generated shock than to the breakdown-generated shock. This was determined by measuring the radius of the shock produced by breakdown alone at a given time and comparing it to the radius of a target-generated shock at the same time and laser energy. The times considered were 5 and 10 μs when the expansion is Taylor-von Neumann-Sedov. The similarity law for a Taylor-von Neumann-Sedov shock implies

$$\frac{E_1}{E_2} = \left(\frac{R_1}{R_2}\right)^5 , \qquad \text{(II-1)}$$

where subscript 1 is with no target, subscript 2 is with a target, E is the shock wave energy, and R is the shock radius. Comparison of eight different shock radii yielded an average energy ratio of 0.32. Therefore, the energy coupled to the breakdown-generated shock is about one-third of the energy in the shock resulting when a target is present.

Superposition of emission pictures of laser shots with and without targets also show that the breakdown is nearly centered at the focus of the laser. At higher pressures, the center of breakdown moves from the focus toward the focusing lens. The luminous radii of the air-breakdown shocks are always less than the target-generated luminous radii at a given time.

There is a third problem involving the luminous radii measurements. Several 50-torr shots show an atypical luminous expansion, but the differences disappear at times greater than 1 μs. An example is shown in Fig. II-4. Two explanations are possible. The luminous phase at 50 torr is short-lived, with a large variation in total emission. The emission framing camera has poor dynamic range, and it is necessary to expose early frames heavily in order to obtain normal exposures at later times. Heavy exposures cause image distortion (the image "pincushions" and shrinks). It is also likely that the breakdown causes the early luminous-expansion rates of the 50-torr shocks to be a sensitive function of the laser beam characteristics (e.g., degree of focus). This could possibly cause highly aspherical energy deposition and irregular initial expansion, but would have little effect on the later shock-wave expansion.

The atypical data showed random initial expansion rates at velocities which are always less than the typical data. For this reason, the atypical luminous data were not used.

To overcome the problem of getting only one interferogram per shot, interferograms for several shots were taken with a constant time and different laser energies between $\simeq$ 5 and 30 J. This was repeated for exposure delay times of 0.425, 0.700, 1.0, 2.5, 5, 10, 20, and 30 μs.

For each time, a log-log plot was made of the shock radius at a given time [$R_s(t)$] vs laser energy on target (E_L). This process was likewise applied to the MCPI[2] photographs, which are also taken one per shot.

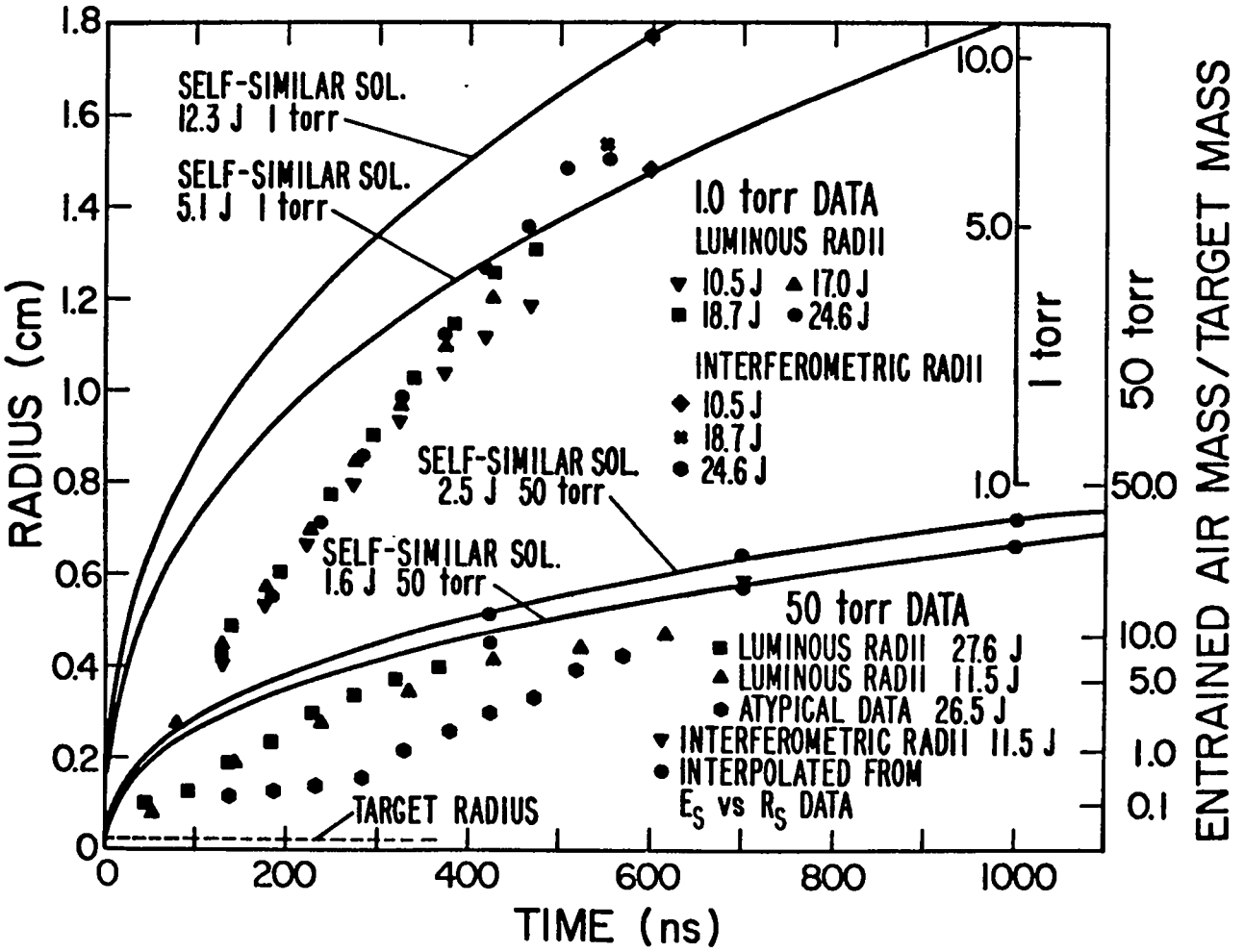

Fig. II-4. Linear plot of radius-vs-time data from several experiments, compared with similarity calculations.

Figure II-5 shows a log-log plot of E_L vs $R_s(t)$ taken from interferograms for several shots at a common time t = 10 μs. Note that the points fall on a fairly straight line of large slope; the major source of error in the data is the uncertainty in E_L. I assumed that

$$E_L = a\, R_s(t)^b \quad , \tag{II-2}$$

where a and b can be determined by a fit to the data. There is no a priori reason to believe the 50-torr data should obey a functional form of Eq. (II-2); coupling of the laser energy to the targets is not a simple process, and the air breakdown at 50 torr complicates it further. However, linear correlation of the interferogram data points for a given time on log-log plots of R_s vs E_L is very good (> 0.9 for four or more points in the interval 0.7 μs $\lesssim$ t $\lesssim$ 10 μs). Therefore, fitting Eq. (II-2) as described below provides adequate interpolation for the energy range of this experiment (5 $\lesssim E_L \lesssim$ 30 J).

Fit of $R_s(t)$ vs E_L Data

The fit to Eq. (II-2) was done in a straightforward manner [Bevington (1969)]. Taking the log of both sides, one obtains

$$\log_{10}E_L = b \log_{10}R_s + \log_{10}a \quad . \tag{II-3}$$

The equation takes the form of a straight line of intercept A and slope b with the correspondence $A = \log_{10}a$, $y = \log_{10}E_L$, and

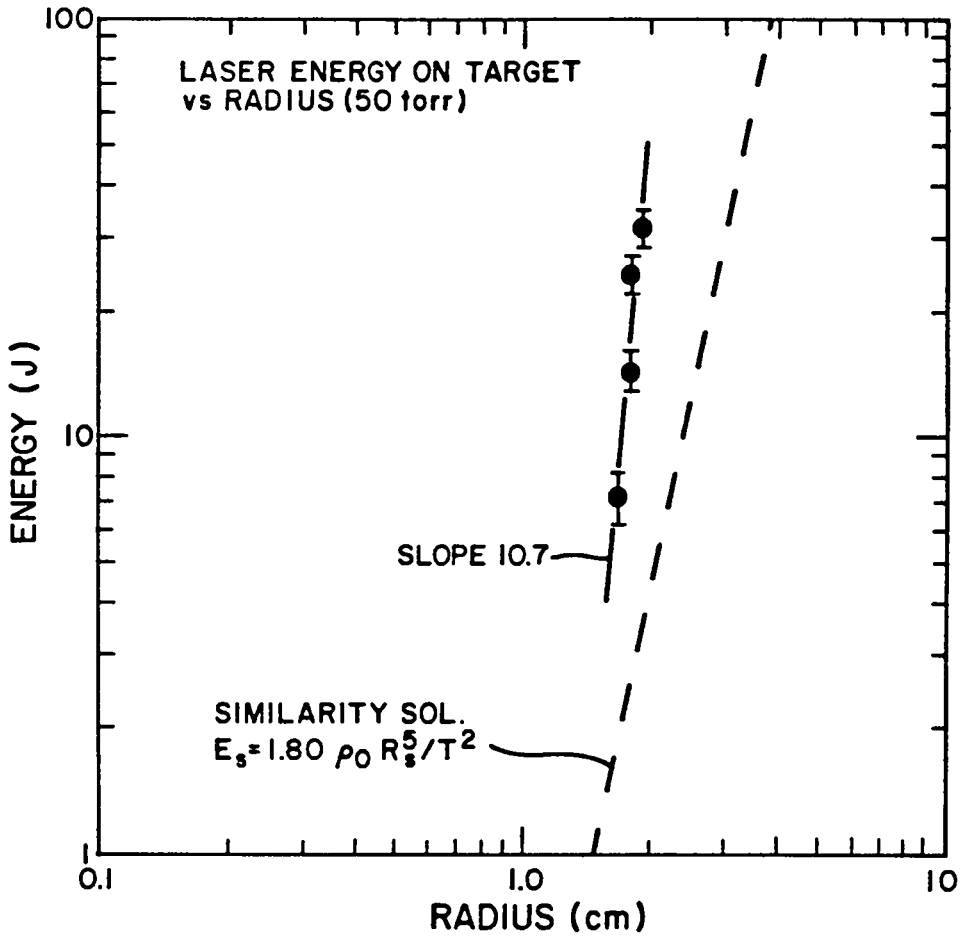

Fig. II-5. Radii of experimental 50-torr shock waves taken from interferograms at 10 μs, as functions of laser energy (E_L) on target. Solid line is a fit to the data, and dashed line is a similarity curve assuming 100% laser-shock energy coupling and $\gamma = 1.2$.

$x = \log_{10} R_s$. Weights for the fit $\sigma_{E_L}{}'$ are obtained from the uncertainties in E_L, (σ_{E_L}) by

$$\sigma'_{E_L} = \frac{d(y)}{dE_L}\,\sigma_{E_L} = \frac{\log_{10} e}{E_L}\,\sigma_{E_L} \quad . \tag{II-4}$$

Once A and b and their associated uncertainties σ_A and σ_b are obtained from standard linear least-squares fitting, the uncertainty in a, (σ_a) is given by

$$\sigma_a = \frac{\sigma_A}{\frac{dA}{da}} = \frac{a}{\log_{10} e}\,\sigma_A \quad . \tag{II-5}$$

Interpolation can be used to obtain R_s for a given E_L at some time t, as well as the probable error (σ_R) in R_s. That is,

$$R_s = \left(\frac{1}{a}\right)^{1/b} \cdot (E_L)^{1/b} \text{ and } \sigma_R = \sqrt{\left(\frac{\partial R_s}{\partial b}\,\sigma_b\right)^2 + \left(\frac{\partial R_s}{\partial a}\,\sigma_a\right)^2}. \tag{II-6}$$

Figure II-4 shows a plot of R_s-vs-t data for two shots in 50-torr air, with 11.5 and 27.6 J laser energy on target. An interferogram point was taken at 0.7 μs for the 11.5-J shot and is plotted. The points interpolated as described above from the E_L-vs-R_s(t) data are plotted for t = 0.7 and 1.0 μs, using E_L = 11.5 and 27.6 J.

Figure II-6 is a plot of radius points for E_L = 25 J and 50 torr, interpolated from plots such as Fig. II-5 for both the MCPI^2 and interferometry data. The large error bars for the MCPI^2 data are due to the random error in timing of the MCPI^2 exposures created by the previously mentioned trigger jitter. This results in scatter

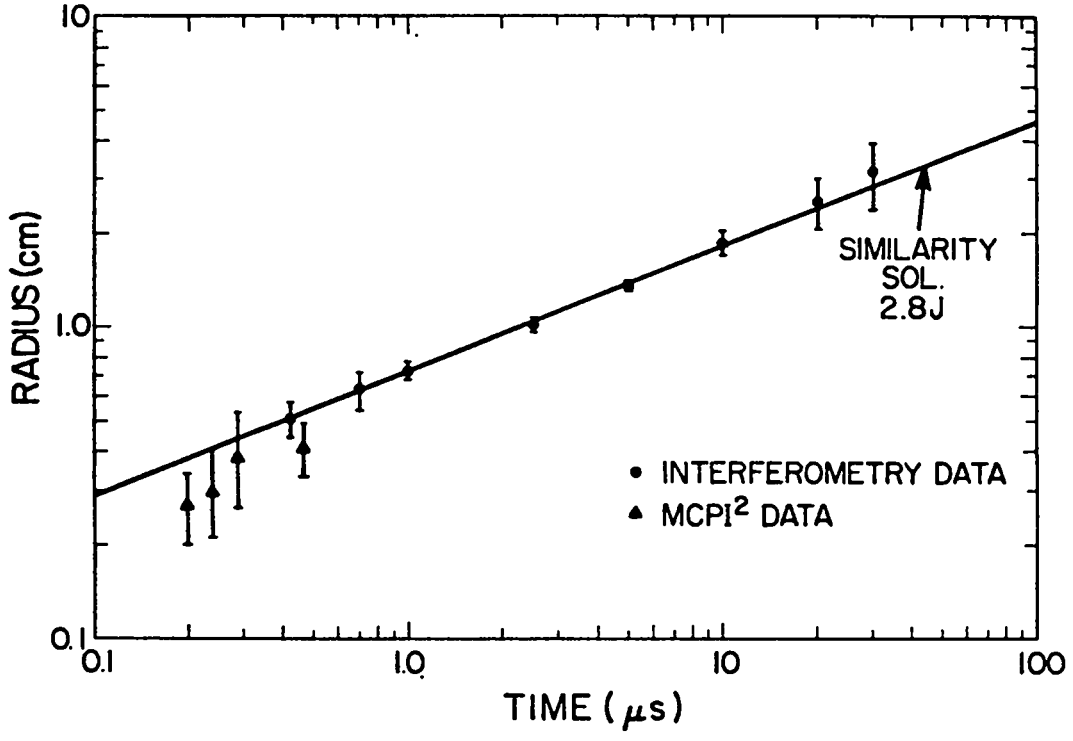

Fig. II-6. Radius-vs-time points interpolated from the radius-vs-E_L MCPI^2 and interferometry data, assuming E_L = 25 J, compared with a 2.8-J similarity curve.

of the radius measurements in the E_L-vs-$R_s(t)$ plots, which are assumed to have no error in t.

Assignment of Shock Energy

The shadowgraphy sequences and the interferometry and MCPI^2 data of Fig. II-6 show that, from about 1 to 15 μs, the 50-torr

shock expands at a rate approximately obeying the $R_s \propto t^{0.4}$ ideal, instantaneous point-source blast law. A fit to the 1-, 2.5-, 5-, and 10-μs points of Figs. II-6, using the method described in the previous section and ignoring the error bars, gives $R_s \propto t^{0.41\pm0.01}$. The linear correlation coefficient is 0.993. It is therefore reasonable to assume that in this range of times, E_s can be determined from the similarity equation for a point explosion. Here E_s is the energy of the shock wave as distinguished from E_L, the energy of the illuminating laser beam.

For the experiments at 1 torr, Fig. II-4 indicates that, at about 600 ns, the luminous expansion of the shock begins to slow and the luminous radius falls below the measured interferometric radius. At this point, the shocks have entrained 5 to 10 target masses of air. An examination of the corresponding point in the 50-torr shock data shows that the 50-torr shocks have begun to expand as $R_s \propto t^{0.4}$. Furthermore, fitting Eq. (II-2) to the 1-torr interferometer data at 600 ns yields $b = 4.7\pm0.8$, close to the value of 5 expected from the point-source similarity solution. Breakdown does not occur at 1 torr, so it can be assumed that the fraction of E_L coupled to E_s is approximately constant and independent of E_L. Therefore, it is reasonable to assume that the 1-torr interferometric radii at $t \gtrsim 600$ ns as well as the 50-torr radii at $0.5 \lesssim t \lesssim 10$ μs can be used to assign a shock energy, E_s, to the shot using the self-similar equation relating R_s and t to E_s.

Chernyi's approximate expression, as given by Zel'dovich and Raizer (1966), was used to assign a shock-wave energy E_s:

$$E_s = \xi \rho_o \frac{R_s^5}{t^2} = \frac{16\pi}{75} \frac{3\gamma - 1}{(\gamma - 1)(\gamma + 1)^2} \rho_o \frac{R_s^5}{t^2} \quad , \qquad \text{(II-7)}$$

where ρ_o is the ambient density and t the time. This approximate expression for ξ yields values close to those given by Sedov's (1959) expression (especially when the heat capacity ratio $c_p/c_v = \gamma = 1.2$), and is much simpler than Sedov's equation.

The value of γ for air at temperatures below about 3000 K is 1.4. Above this temperature, dissociation and eventually ionization lower γ to $\sim$ 1.2. The values for ξ from the approximate expression in Eq. (II-7) (exact calculation) are 1.8 (1.8) for $\gamma = 1.2$ and .93 (.85) for $\gamma = 1.4$, so the error in ξ calculated from the expression in Eq. (II-7) is at most less than 9%. The critical feature is that ξ, and therefore E_s, varies by a factor of nearly 2 for a choice of $\gamma = 1.2$ to 1.4. Therefore, calculating E_s from a value of R_s measured at some t can lead to considerable error, depending on the choice of γ. The value of γ, and therefore ξ, will vary for a strong shock as it expands and weakens. The true value of E_s is constant (neglecting radiative losses), and therefore the $R_s \propto t^{2/5}$ relation does not strictly hold. The influence of the variation of ξ on the $R_s \propto t^{2/5}$ relation, however, is small because $R_s \propto \xi^{-1/5}$. A factor of 2 variation in ξ implies R_s is modified at most by ~13%. (This is discussed in more detail in Chapt. IV, in considering the target equation-of-state.) Some radius-vs-time curves derived from Eq. (II-7) with $\gamma = 1.2$ are plotted in Figs. II-4 and -6 for values of E_s that best fit the appropriate interferometry data. The

50-torr, 2.5-J curve in Fig. II-4 was selected based on the fit to the interferometer radius of the 27.6-J shot measured at 2.5 μs.

Other Features of the Radius-vs-Time Data

We are interested in the fraction of laser energy coupled to the shock wave, $f_c = E_s/E_L$. Although the physical processes that determine f_c are outside the scope of this thesis, the values obtained here are worth comparing with other works where the shock energy was used as a diagnostic to determine f_c.

The fact that $E_L \propto R_s^b$ [Eq. (II-2)] with $b = 4.7 \pm 0.8$ for 1-torr data makes it reasonable to assume that $E_s = f_c E_L$, with f_c independent of E_L. The R_s-vs-t data yield values of $f_c = 0.4$ to 0.5. In the 1-torr case with $t \simeq 600$ ns, E_s was calculated from Eq. (II-7) with $\gamma = 1.2$. The estimate for the shock front temperature in Chapt. III indicates $\gamma = 1.2$ is probably very good. Actually, f_c might be expected to depend on the irradiance of the beam, since reflectivity should vary with irradiance. For the target geometry and irradiance range of about 0.3 to 1 x 10^{15} W/cm^2 used here, f_c appears to be independent of E_L for the 1-torr data.

Using a multibeam Nd:glass laser, Basov et al. (1976) found $f_c \simeq 0.40$ for $(CH_2)_n$ spherical targets irradiated with 300 J at irradiances of 1 x 10^{15} W/cm^2 with 1.5-ns pulses in 8- to 12-torr deuterium. They used Chernyi's approximation to get E_s. Leonard and Mayer (1975) found values of about 5 to 10% from shocks in 20-torr helium generated from 140-ng 100-μm glass-shell targets irradiated by two 90-J 900-ps Nd:glass lasers. Leonard and Mayer used a different approximation to find E_s.

Unlike the 1-torr data, the 50-torr data show a dependence of f_c on E_L. The average value of b in Eq. (II-2) for the 50-torr data between 1 and 10 μs is 10.3 ± 0.5. The shock expands as $R_s \propto t^{0.4}$. Assuming the motion is self-similar, Eq. (II-7) holds and $E_s \propto R_s^5$. With R_s also proportional to $E_L^{1/b}$, we have $f_c = E_s/E_L \propto R_s^5/E_L \propto E_L^{5/b}/E_L$, or

$$f_c \propto E_L^{(5-b)/b} \quad . \tag{II-8}$$

With $b \cong 10$, this implies that $f_c \propto 1/\sqrt{E_L}$ and gives the energy dependence of the "shuttering" effect due to air breakdown in front of the target under the conditions of the experiment. E_s-vs-R_s at 10 μs and 50 torr, derived from Eq. (II-7) with $\gamma = 1.2$, is plotted in Fig. II-5 for comparison with E_L-vs-R_s. Comparison of the similarity curve and interpolated data of Fig. II-6 indicates $f_c = 0.1$ for $E_L = 25$ J and a pressure of 50 torr.

There are several phenomenological features of the radius-vs-time data that can be compared to analytical and numerical predictions. The self-similar expansion at moderate times ($t \gtrsim 600$ ns for 1 torr, and $1 \lesssim t \lesssim 10$ μs for 50 torr) has already been mentioned. We will point out several more features of the data here.

Figure II-4, as well as other data, show that the velocity of the transverse luminous expansion is at most weakly dependent on E_s, being nearly always constant at about 10^6 cm/s in the 50-torr case and always constant at 3×10^6 cm/s in the 1-torr case. Two sets of data, taken at 0.5 torr, gave initial velocities of 4 and 4.2×10^6 cm. Finally, a maximum transverse thermal plasma-expansion velocity

of $1.0\pm0.1 \times 10^7$ cm/s for E_L = 25 J was found in vacuum, using the charge cups.

The luminous region expands at a nearly constant velocity ($R_s \propto t^{0.92\pm0.1}$ at 50 torr, $R_s \propto t^{0.95\pm0.06}$ at 1 torr) until about 300 ns for the 50-torr data and about 400 ns for the 1-torr data. At these times, the luminous expansion slows and extrapolation indicates the shock breaks away from the luminous region, eventually expanding with $R_s \propto t^{0.4}$ The transition to a blast wave from $R_s \propto t$ to $R_s \propto t^{0.4}$ is apparently abrupt. The radius of this transition will be called the radius of maximum deceleration (R_D) of the shock front and is equivalent to the value of R_s where the curvature of the R_s-vs-t curve is maximum, or equivalently $\ddot{R}_s = 0$. R_D can be estimated by taking the intercept of an R-vs-t curve of constant velocity V_0 and a self-similar curve of given energy E_s. Using $R_s = V_0 t$ to eliminate t in Eq. (II-7) yields

$$R_D = \left(\frac{E_s}{\xi \rho_0 V_0^2} \right)^{1/3} . \qquad \text{(II-9)}$$

If V_0 were proportional to $\sqrt{E_s}$, R_D would be independent of E_s. This would be in accordance with several theoretical models considered in Chapt. IV that include source mass.

The data of Basov et al. (1973) indicate a period of time when $R_s \propto t^{\alpha}$, with $\alpha > .4$ and an initial velocity of 5×10^7 cm/s. In their case, deuterium gas was used with $\rho_0 \sim 1.4 \times 10^{-6}$ g/cm^3. Laser energies of ~ 300 J and solid spherical $(CD_2)_n$ target masses of ~ 10 μg were used. They measured shock-wave energies of 50 to 100 J. The shock-energy to target-mass ratio is therefore typically 5×10^6

to 10 x 10^6 J/g, as compared to the ratio of 0.7 to 3.3 x 10^6 J/g in the present experiment.

The data considered by Leonard and Hammerling (private communication, to be published) were obtained by irradiating glass microballoons with an Nd:glass laser in a background of helium at 4.4 x 10^{-6} g/cm^3. Laser energies of 20 to 200 J resulted in shock energies of 10 to 20 J. In one set of data for a 137-ng target, a time-independent velocity of ~ 7 x 10^7 cm/s can be inferred, corresponding to a shock-wave energy of 10 J. However, an experiment using an 812-ng target apparently has an $R_s \propto t^{\sim 0.7}$ relationship. Leonard and Hammerling used emission cameras, whereas Basov derived his measurements by shadowgraphy

Once the shock wave has broken free from the luminous region and begun to expand as a blast wave, the expansion velocity of the luminous region itself abruptly decreases. Assigning a maximum radius is difficult; the edge becomes indistinct and is, to a large extent, a function of the camera sensitivity. Empirical formulas for nuclear explosions near sea level [Glasstone (1962)] give the maximum radius of the "fireball" as $R_{FB} \propto (E_s)^{0.4}$. Extrapolation of the luminous 1-torr data in Fig. II-4 as the expansion slows would seem to indicate a somewhat smaller power. The breaking away of the shock from the luminous region shows that care must be taken when assigning shock energies to radius-vs-time measurements made in emission [e.g., Leonard and Mayer (1975)].

Summary

This chapter has presented the shock wave radius-vs-time data and describes the methods of data reduction that were used.

The shock wave expansion exhibits two phases. The later phase has a strong-shock ($R_s \propto t^{2/5}$) expansion rate, which begins at about 1 μs for the 50-torr data and at about 600 ns for the 1-torr data. The early phase, which is luminous, exhibits considerable asphericity due to non-uniform target irradiation and (in the 50-torr case) air breakdown. The early radial expansion velocity, transverse to the Nd:glass laser beam, is nearly constant. The initial near-constant velocity is 3×10^6 cm/s in 1-torr air and 1×10^6 cm/s in 50-torr air.

The $R_s \propto t^{2/5}$ relation, during the later phase expansion, is used to assign an energy to the shock wave by comparing the data with an approximate similarity relation. The shock wave energy is then compared to the laser energy to determine coupling efficiencies for comparison with similar previous experiments.

The energy dependence of the "shuttering" effect caused by the air breakdown was also considered. Coupling efficiency was 45% for shocks in 1-torr air, independent of laser energy, and 10% for shocks in 50-torr air with $E_L = 25$ J. Coupling efficiency for 50-torr experiments exhibited a $1/\sqrt{E_L}$ energy dependence.

Other features of the radius-vs-time data are pointed out for comparison with analytical and numerical calculations in following chapters. Features include the abrupt transition to the self-similar expansion and the energy dependence of the radius of shock breakaway from the luminous region.

CHAPTER III

INTERFEROGRAM REDUCTION

Interferogram Interpretation

The holographic interferograms are equivalent to those of a standard interferometer such as a Mach-Zehnder type. The background fringe pattern of a standard interferogram is created by a slight misalignment of the optical system. The background fringes of a holographic interferogram result from a slight displacement of one of the optical components (prism P1 in Fig. I-1a) at some time between the preliminary reference exposure and the event exposure.

The scene beam in Fig. III-1 travels parallel to the z-axis through a hypothetical spherical shock wave of radius R_s. The nearest approach of a beam with position (x_1,y_1) to the shock-wave center is

$$r_{z1} = (x_1^2 + y_1^2)^{1/2} \quad . \tag{III-1}$$

The incremental optical path length, ds, in units of wavelength, is related to the increment of travel, dz, by

$$ds(\vec{r}) = \frac{1}{\lambda}\, \eta(\vec{r})\, dz \quad . \tag{III-2}$$

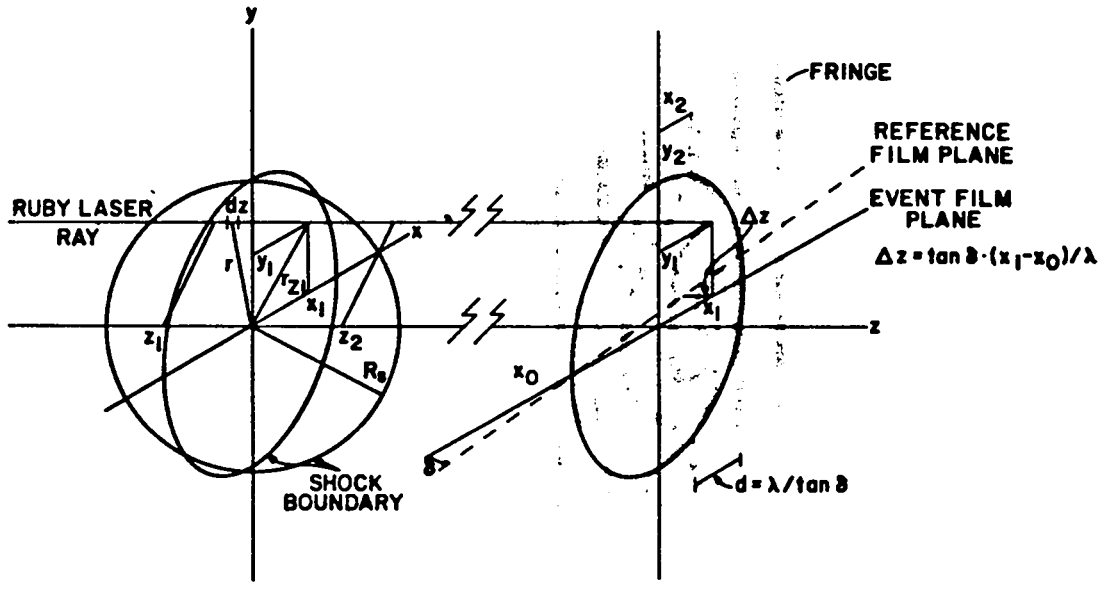

Fig. III-1. Schematic of holographic interferometry process.

$\vec{r}$ is the position of dz relative to the shock center and $\eta(\vec{r})$ is the index of refraction at $\vec{r}$. By spherical symmetry, $\eta(\vec{r}) = \eta(r)$. If refraction by the shock wave is disregarded, each ray traversed the same geometrical path during the reference exposure. The corresponding optical path was

$$ds_a(\vec{r}) = \frac{1}{\lambda} \eta_a \, dz \quad , \qquad \text{(III-3)}$$

where η_a is the index of refraction of the undisturbed gas. Each hologram exposure is a record of the wave front at the time of

exposure and the double exposure compares the two wave fronts. The result is a record of the total path difference in units of wavelength. The path difference due to the shock wave is

$$s(x_1,y_1) = \frac{1}{\lambda}\int_{z_1}^{z_2}[n(x_1,y_1,z) - n_a]dz \quad , \qquad \text{(III-4)}$$

where z_1 and z_2 are the z-values at the points the ray enters and leaves the shock region. With the origin defined as the shock center, $z_1 = -z_2$.

To first approximation, the effect of displacing P1 in Fig. I-1a between exposures is equivalent to a translation along z and rotation of the photographic plate in the x-z plane by an angle δ. The resulting path difference in wavelengths is $\Delta z = \tan\delta(x_1 - x_0)/\lambda$. δ and x_0 are defined in Fig. III-1. The ray chosen for analysis in Fig. III-1 falls on a fringe so the total path difference in units of wavelength between the reference exposure ray and event exposure ray is

$$s(x_1,y_1) + \tan\delta(x_1 - x_0)/\lambda = (2n + 1)/2 \quad , \qquad \text{(III-5)}$$

where n is an integer. The difference in path length between a reference exposure ray and event exposure ray passing outside of the shock and striking the plate on the same fringe at (x_2,y_2) is

$$\tan\delta(x_2 - x_0)/\lambda = (2n + 1)/2 \quad . \qquad \text{(III-6)}$$

The result of subtracting Eq. (III-6) from Eq. (III-5) is

$$s(x_1,y_1) + \tan\delta(x_1 - x_2)/\lambda = 0 \quad . \qquad \text{(III-7)}$$

The difference in path length for rays incident on two adjacent background fringes is one wavelength or $\lambda = d\tan\delta$ where d is the background fringe spacing. Substituting this expression for λ into Eq. (III-7) gives

$$s(x_1,y_1) = \frac{\tan\delta(x_2 - x_1)}{d\tan\delta} = \frac{x_2 - x_1}{d} = f(x_1,y_1) \quad . \qquad \text{(III-8)}$$

Therefore (as in the case of a conventional interferogram), the difference in optical path length is equal to the measured quantity $f(x_1,y_1)$, which is just the fringe shift in units of background fringe spacing.

The relation

$$dz = \frac{rdr}{\sqrt{r^2 - (x^2 + y^2)}} \qquad \text{(III-9)}$$

and Eq. (III-1) are used in Eq. (III-4) to eliminate z in favor of r and r_z, where r_z is the distance of an arbitrary ray from the z-axis.

The integration limits of Eq. (III-4) for an arbitrary ray at (x,y) transform as

$$\int_{z_1}^{z_2} = \int_{-z_2}^{z_2} = 2\int_{0}^{z_2} \rightarrow 2\int_{r_z}^{R_s} \quad . \qquad \text{(III-10)}$$

where $r_z = \sqrt{x^2 + y^2}$.

Substitution of Eq. (III-9) into Eq. (III-4) gives

$$f(r_z) = 2 \int_{r_z}^{R_s} \frac{g(r)\, r}{\sqrt{r^2 - r_z^2}}\, dr \quad , \qquad \text{(III-11)}$$

where

$$g(r) = [n(r) - n_a]/\lambda \quad . \qquad \text{(III-12)}$$

This is an Abel integral equation, whose inverse is given by

$$g(r) = -\frac{1}{\pi} \int_{r}^{R_s} \frac{f'(r_z)dr_z}{\sqrt{r_z^2 - r^2}} \quad . \qquad \text{(III-13)}$$

where f' is the derivative of f with respect to r_z. Either $n(r)$ can be obtained from measured values of $f(r_z)$ using Eqs. (III-12) and (III-13), or $f(r_z)$ can be calculated from a theoretical $n(r)$ using Eq. (III-11) and compared directly with the data. The former procedure, i.e., direct inversion of the integral equation, is numerically the most difficult. The combination of noise in the data that produces variations in f' and the weighting in the denominator of Eq. (III-13) causes a large noise amplification in g(r). The integral equation inversion techniques are described in Appendix B.

Measurement of Fringe Shift

To obtain $n(r)$, it is necessary to measure the fringe shift in units of background fringe spacing, $f(r_z)$ at a number of points between $r_z = r$ and $r_z = R_s$.

The 35-mm film reproductions of the interferograms are projected onto a computer-coupled graphics tablet. The tablet transmits Cartesian coordinates of a cursor placed on its surface to a computer for storage. The coordinates can be sent one at a time or continuously with 0.01" resolution at the tablet surface. If the resolution of the interferograms is 100 μm at the shock wave, then an image of a 1-cm diameter shock must be projected to a diameter of $\gtrsim$ 1." on the tablet surface to obtain comparable tablet resolution. The shocks are typically projected to about 10" in diameter in order to make it easier to trace the fringes; points are digitized at the densities found to be optimum in Appendix B.

Typically, 10 points are digitized on each of the background fringes (five on each side of the shock wave). Least-squares straight lines are then fit to these points and a record of the fringe number, slope, and intercept are made. Points are continuously digitized along the disturbed portion of the fringe. The fringe shift for each point is calculated using the fringe number and the background-fringe line data. The result is a set of f(x,y) along each fringe. A limited number of fringes are used, preferably ones that are transverse to the Nd:laser direction and pass nearest the shock center.

The f(x,y) values are next converted to $f(r_z)$. First, a point is digitized at the intersections of each fringe and the shock-wave boundary. The process generates at least four shock-boundary points that are least-squares fitted to a circle using a parameter-space searching routine [Chandler (1975)]. Once the circle center

(x_c,y_c) is obtained, the coordinate conversion is completed, using $r_z = \sqrt{(x - x_c)^2 + (y - y_c)^2}$.

The smallest value of r_z for a given fringe is > 0.0 unless the fringe passes directly through (x_c,y_c). The smallest value of r_z is found for each fringe and is used to divide the fringe into a "left" and "right" profile extending from the minimum r_z to R_s. These profiles are then inverted using Eq. (III-13) and the method of Appendix B to get $\eta(r)$, the index of refraction, as a function of r.

Index of Refraction Interpretation

The result of Abel-inverting a fringe profile is the radial index of refraction function $\eta(r,\lambda)$ where the wavelength dependence is noted. The index of refraction can be related to the density of the various chemical components of the gas using the Gladstone-Dale relation, or to the polarizability and number density of the components by

$$\eta(r,\lambda) - 1 = \sum_i K_i(\lambda)\rho_i(r) = 2\pi \sum_i \alpha_i(\lambda)n_i(r) \quad , \qquad \text{(III-14)}$$

where $\alpha_i(\lambda)$ is the polarizability in cubic centimeters of the ith component with number density $n_i(r)$ per cubic centimeter. The density is $\rho_i(r)$ grams per cubic centimeter, and the specific refractivity, $K_i(\lambda)$, is in cubic centimeters per gram. A value of K(694.3 nm) = 0.2247 cm^3/g for nondissociated air [calculated from Cauchy's formula for air in Forsythe (1956) Table 553] has been used to make estimates of refractive effects. This value shows only a slight dependence on wavelength with K(347.2 nm) = 0.2330 cm^3/g.

The values of K at 546.1 nm for O_2 and N_2 are 0.19 and 0.24 cm^3/g, respectively.

Equilibrium calculations for air at one atmosphere [e.g., Zinn and Sutherland (1975)] show that oxygen begins to dissociate at ~ 0.2 eV and both nitrogen and oxygen are dissociated by ~ 0.6 eV. It is therefore necessary to consider the change in the index of refraction of air as the air components dissociate.

Shock-tube interferometric measurements of OI and NI by Alpher and White (1959) at λ = 412.2 to 544.6 nm gave K = 0.18 $\pm$ 0.02 cm^3/g for OI and 0.31 $\pm$ 0.02 cm^3/g for NI. Finite perturbation calculations of the static polarizabilities by Werner and Mayer (1976) have been estimated to be 2% accurate for OI and NI. These values (α = 1.10 x 10^{-24} cm^3 for NI and 0.802 x 10^{-24} cm^3 for OI) yield K = 0.297 cm^3/g for NI and 0.189 cm^3/g for OI. The agreement of the static calculations and dynamic measurements indicates little dependence on wavelength. These values indicate that K should vary from 0.22 or 0.23 cm^3/g for nondissociated air to 0.275 cm^3/g for completely dissociated air.

There is a further dependence of α and K on excitation, but this appears to be slight, at least for the lower state of OI and NI [Nesbet (1977)]. Slight effects of anomalous dispersion by excited N^+ will be considered in a following section.

Ionization becomes important for shock velocities where the shock front temperature is $T_s \simeq 1.0$ eV. Values of K or α for N^+ and O^+ do not appear to be available in the literature. The ratio of static values of α for the ion B^+ and the parent atom B [Mukherjee and Moitra (1978); Werner and Meyer (1976)] give

$\alpha(B^+)/\alpha(B) = 1.69 \times 10^{-24}\ cm^3/3.03 \times 10^{-24}\ cm^3 = 0.56$. This ratio is not very different from 1. The presence of the electrons is much more important in determining α. Therefore the α of N^+ and O^+ will be taken to be the same as the α of NI and OI. It will be assumed that there is little variation in α of O^+ and N^+ from λ = 347.2 to 694.3 nm.

The contribution to η from the electrons can be calculated from $\eta = ck/\omega$ (where k is the wave number, ω the angular frequency, and c the speed of light), using the dispersion relation for a transverse electromagnetic wave in a field-free plasma. The result is

$$\eta_e(\lambda)-1 = \sqrt{1 - (\omega_p/\omega)^2} - 1 \simeq -\frac{1}{2}\left(\frac{\omega_p}{\omega}\right)^2 = -\frac{1}{2\pi}\frac{\lambda^2 n_e e^2}{c^2 m_e}$$

$$= -4.48 \times 10^{-14}\ \lambda^2 n_e, \quad \text{(cgs)} \qquad \text{(III-15)}$$

with n_e the electron number density, m_e the electron mass, e the electron charge, ω_p the plasma frequency, and $\omega_p \ll \omega$. The right-hand side is negative and shows a squared-wavelength dependence. The factor multiplying n_e is 10 to 50 times larger than typical atomic and molecular values of $2\pi\alpha$ [see Eq. (III-14)]. If $\eta(r,\lambda)$ is available for two wavelengths, $n_e(r)$ can be determined for all r regardless of conditions by assuming the α_i for the atomic, ionic, and molecular components are independent of λ. The number density of electrons, $n_e(r)$, is then determined from Eqs. (III-14) and (III-15) to be

$$n_e(r) = \frac{\eta(r,\lambda_2) - \eta(r,\lambda_1)}{-4.48 \times 10^{-14} (\lambda_2^2 - \lambda_1^2)} \text{ , (cgs) .} \qquad \text{(III-16a)}$$

or

$$n_e(r) = 6.17 \times 10^{21}[\eta(r,\lambda_1) - \eta(r,\lambda_2)] \qquad \text{(III-16b)}$$

for a doubled ruby laser with λ_1 = 347.2 nm and λ_2 = 694.3 nm. By assuming a value for K, $\rho(r)$ can then be found using Eq. (III-14) and is given by

$$K\rho(r) = \eta(r,\lambda) - 1 - 2\pi\alpha(\lambda)n_e \text{ ,} \qquad \text{(III-17)}$$

where $2\pi\alpha = -2.16 \times 10^{-22}$ cm^3 for λ = 694.3 nm and $2\pi\alpha = -5.40 \times 10^{-23}$ cm^3 for λ = 347.2 nm.

Equations (III-16) and (III-17) can be used for determining n_e and ρ if there are no perturbing influences due to anomalous dispersion from nearby absorption lines.

The largest contribution to $\eta - 1$ from anomalous dispersion comes from an absorption line of N^+ at 694.367 nm [Moore (1971)], which originates from a transition between the $3d^3P_2^0$ (23.42 eV) and the $4p^3P_2$ (25.20 eV above the ground state) levels. The oscillator strength is f_{if} = 0.0473 [Wiese et al. (1966)]. The amount of anomalous dispersion depends on the extent of overlap between the absorption line and the laser line. The ruby laser wavelength is a function of rod temperature, which was maintained at 19°C by a circulating water bath. Pressley (1971) has compiled data for the

wavelength of ruby laser emission in the atmosphere vs rod temperature. If the data are assumed to be for a standard atmosphere, the ruby emission in vacuum from a 19°C rod is 694.447 nm.

The value of $\eta - 1$ for light with wavelength $\lambda = c/\nu$ near a transition from an initial state (i) to a final state (f) with wavelength $\lambda_{if} = c/\nu_{if}$ is given in cgs units by [see for example Thorne (1974)]

$$\eta - 1 = \frac{e^2}{4\pi m_e} \frac{n_i f_{if}}{\nu_{if}} \frac{\nu_{if} - \nu}{(\nu_{if} - \nu)^2 + (\frac{\delta\nu}{2})^2} \quad . \qquad \text{(III-18)}$$

Here, n_i is the number density of ions or atoms in the lower initial state and $\delta\nu$ is the full-width at half-maximum (FWHM) of the Lorentzian absorption profile with central frequency ν_{if}.

The dominant contribution to the line width is Stark broadening by electron impact. The Stark-broadening line width is larger than the Doppler width and there is a shift in ν_{if} as well. Stark N^+ line-width calculations by Hey (1976) using Griem's (1968) semi-empirical method have given values acceptably close to experimental values. Hey and Bryan (1977) suggest that an effective Gaunt factor of 0.26 be used to calculate the line widths in N^+ which gave better than 10% agreement between calculated and measured values for lines that they considered. An application of Griem's semi-empirical method with Hey and Bryan's Gaunt factor to the 694.367-nm line yields values for the line-width of

$$\delta\lambda_s = 3.28 \times 10^{-15} \, n_e / \sqrt{T\,(K)} \quad . \qquad \text{(III-19)}$$

This implies $\delta\lambda_s$ = 0.23 nm for $n_e = 10^{17}$ and T = 20000 K, somewhat larger than other N^+ line-widths calculated by Hey. The tabulated value given by Griem (1964) for the 694.367-nm line of N^+ is $\delta\lambda_s$ = 0.14 nm with $n_e = 10^{17}$ and T = 20000 K. The value of Griem will be used to calculate $\delta\nu$ in Eq. (III-18) assuming $\delta\lambda$ proportional to n_e and $1/\sqrt{T}$. The line center is also shifted toward the red. The red shift (d) in λ is given by d = 0.764 $\delta\lambda_s/2$ for the same value T. This quantity $2d/\delta\lambda_s$ is independent of n_e and will again be taken proportional to $1/\sqrt{T}$ based on a 10% fit to the tabulated values of Griem from 2500 to 80000 K.

To find the population of the ith level (n_i), equilibrium is assumed so that

$$n_i = n_{N^+} \frac{g_i \exp(-E_i/kT)}{\sum_j g_j \exp(-E_j/kT)} , \qquad \text{(III-20)}$$

where E_i is the energy (above ground state) and g_i the statistical weight of the ith level. The g_j and E_j values are taken from Moore (1971). n_{N^+} is the number density of N^+ and can be found in Gilmore's (1955,1967) equation-of-state (EOS) tables.

We can make an estimate of the contribution to the total η - 1 from anomalous dispersion by assuming a typical 1-torr shock density of 1.29 x 10^{-5} g/cm^3. The EOS tables indicate that n_{N+} increases with temperature to about 25000 K and decreases sharply at 30000 K (due to ionization of N^+) where it has a value of $n_{N+} \sim 3 \times 10^{17}$. Equation (III-18) is a maximum when $\nu_{if} - \nu = \delta\nu/2$. At 30000 K (2.6 eV) and ρ = 1.29 x 10^{-5} g/cm^3, $n_e \sim 6 \times 10^{17}$ and therefore

$\delta\nu/2 = 2.13 \times 10^{11}$. Equation (III-18) then becomes $n - 1 = 1.04 \times 10^{-20} n_i$. The constant multiplying n_i is a factor of 50 greater than the corresponding constant in Eq. (III-15) with $\lambda = 6.943 \times 10^{-5}$ cm. However, n_i calculated from Eq. (III-20) is a small fraction of n_{N+}. For kT = 2.6 eV, Eq. (III-20) yields $n_i/n_{N+} \sim 1 \times 10^{-4}$. Therefore, the contribution to $\eta - 1$ from anomalous dispersion is at most 0.5% of the electron contribution and is negligible. This value is confirmed in a following section that compares a measured 1-torr $\eta - 1$ profile to an analytical profile for which a detailed calculation of the anomalous $\eta - 1$ was made. The calculation also showed that the anomalous contribution to $\eta - 1$ is at most 20% of the contribution to $\eta - 1$ from the other atoms and ions.

An approximate knowledge of the structure of the shock wave is an aid in relating densities to the measured index of refraction. When the shock expands self-similarly, it is possible to estimate the velocities for which dissociation is significant in the shock front. In cases where the shock is strong enough for dissociation effects to be important, the ambient pressure can be assumed to be negligible compared to the pressure of the shock front. That is, the "strong shock" approximations for the Rankine-Hugoniot jump conditions across the shock discontinuity can be used. For strong shocks, the shock-front density, ρ_s, is related to the ambient density, ρ_o, and the heat capacity ratio, $\gamma = C_p/C_v$, by

$$\rho_s = \frac{\gamma + 1}{\gamma - 1} \rho_o \quad . \qquad \text{(III-21)}$$

The shock-front pressure, p_s, is given by

$$p_s = \frac{2}{\gamma + 1} \dot{R}_s^2 \rho_o \quad , \tag{III-22}$$

where $\dot{R}_s$ is the shock-front velocity. If we take the gram molecular weight (M_w) of air to be 28.9 g/mole, (appropriate for not-too-strong shocks, where the air is not dissociated) the shock-front temperature, T_s (in K), is related to the pressure and density (in cgs) by

$$T_s = \frac{M_w}{k_B N_A} \frac{p_s}{\rho_s} = 3.48 \times 10^{-7} \frac{p_s}{\rho_s} \quad , \tag{III-23}$$

where k_B is Boltzmann's constant and N_A is Avogadro's number. From Eq. (II-7), the velocity of the shock front is

$$\dot{R}_s = \frac{2}{5} R_s/t \quad . \tag{III-24}$$

Combining Eqs. (III-21) through (III-24) results in

$$T_s = 3.48 \times 10^{-7} \frac{4}{25} \frac{2(\gamma - 1)}{(\gamma + 1)^2} \left(\frac{R_s}{t}\right)^2 = 1.11 \times 10^{-7} \frac{\gamma - 1}{(\gamma + 1)^2} \left(\frac{R_s}{t}\right)^2 \tag{III-25}$$

Equation (III-25) holds for strong but not too strong shocks where $T_s \lesssim 0.5$ eV, such that dissociation is not significant and $\gamma = 1.4$. The equivalent of Eqs. (III-23) to (III-25) can also be used to provide estimates of T_s above this temperature if the proper M_w and γ-values are used. To obtain M_w and γ we must use a detailed equation of state.

For typical 50-torr R_s-vs-t data of Chapt. II at times between 1 and 2 μs, Eq. (III-25) predicts that the shock-front temperature varies from 5000 K (~ 0.4 eV) to 2200 K (~ 0.2 eV). In this temperature range there is little dissociation. Therefore, for purposes of obtaining density information from the interferometric data, we can assume $K = 0.23\ cm^3/g$.

For the shocks in 1-torr air, all interferometric data were taken at $t \simeq 0.6$ μs. For a typical $R_s = 1.78$ cm and assuming $\gamma = 1.2$ and $M_w = 28.9$ g/mole, Eq. (III-25) gives $T_s \simeq 40{,}000$ K (3.5 eV). At this temperature not only would the air be dissociated (and $M_w \neq 28.9$ g/mole), it would also be ionized.

For temperatures above 0.5 eV, both the average molecular weight and γ decrease as the result of dissociation and ionization. That is, the equation of state becomes more complicated than it is at lower temperatures. A convenient representation of the equation of state of high-temperature air is shown in Figs. III-2a, and b [from Zinn and Anderson, (1973)]. For present purposes, we wish to find T when p and ρ are known. This can be accomplished by first forming p/ρ and ρ/ρ_o (where $\rho_o = 1.23 \times 10^{-3}\ g/cm^3$), using Fig. III-2a iteratively to find ε, and then finding T from Fig. III-2b.

All 1-torr interferograms were made with a single wavelength, $\lambda = 694.3$ nm. It is therefore not possible to determine both the gas density and electron density in the shock front at the times of the data. However, the shock $T_s \gtrsim 2$ eV and the results of the anomalous $n - 1$ calculation show that, by far, the main contribution to the index of refraction under the 1-torr conditions is from the electrons.

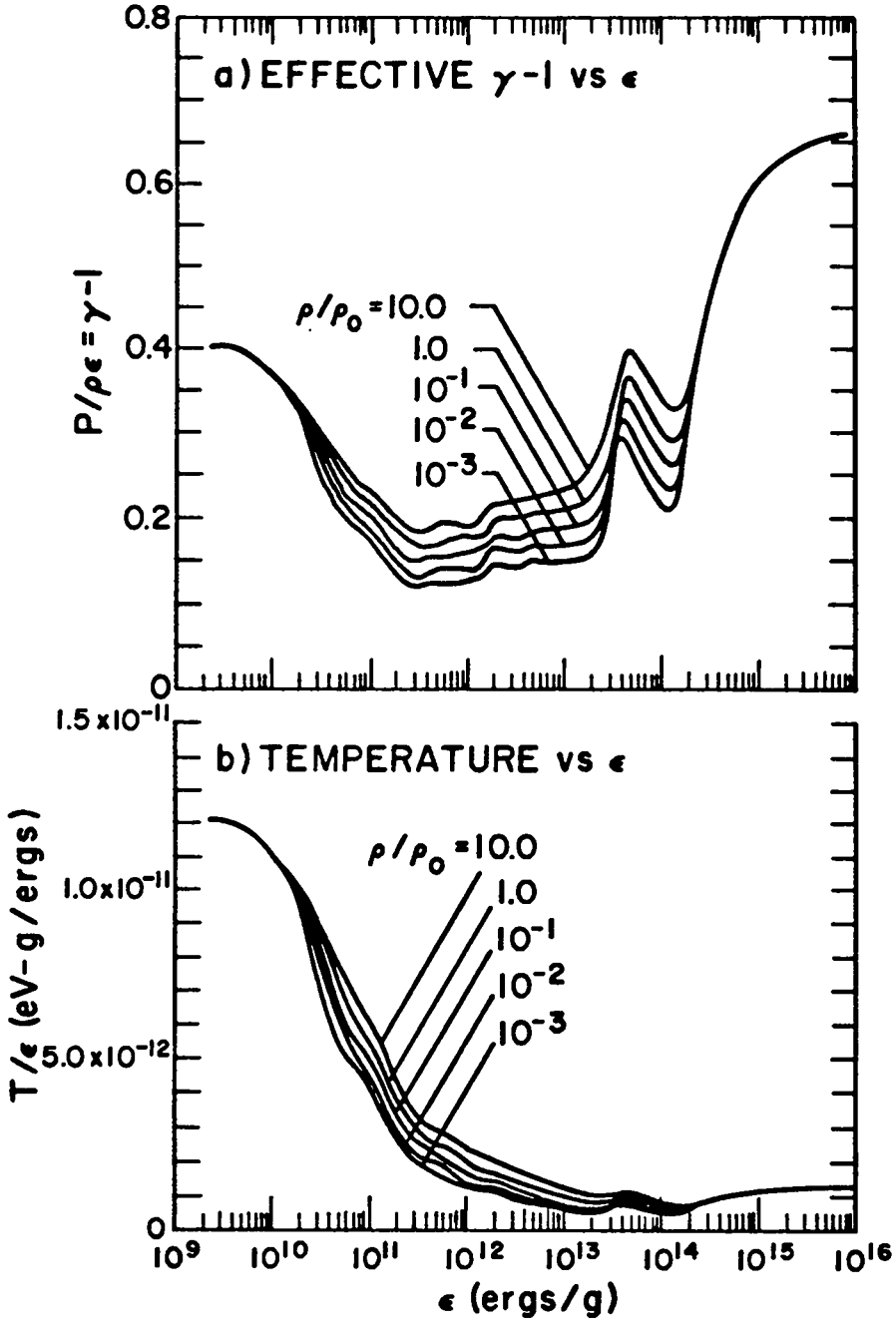

Fig. III-2. Equation-of-state data for air used in numerical and analytical calculations. $\rho_0 = 1.29 \times 10^{-3}$ g/cm^3.

The approximate density profile of Taylor (1950) derived from the self-similarity assumption is given by Eq. (A-3). The gas density approaches zero at the center. The solution also yields a finite pressure at the center, implying that the central temperature is very high. The gas that is present should therefore be highly ionized, resulting in a negative index of refraction. If the measured index of refraction is negative at the center, then it can be interpreted as solely due to electrons, with a negligible neutral gas component.

The following rules can be used for interpreting $\eta(r,\lambda)$. If the shock velocity is below Mach 5, it is a good approximation to assume $K \simeq 0.23$ for purposes of determining the density in the shock front and only a single interferogram is needed to do so. As the shock-front temperature approaches ~ 1 eV (Mach 10 to 20), dissociation becomes important and K approaches $\simeq 0.28$. For $1 \text{ eV} \lesssim T_s \lesssim 2 \text{ eV}$, the presence of electrons becomes important and two interferograms of different wavelengths are needed to determine the gas and electron densities. If $T_s \gtrsim 2$ eV, the gas contribution to $\eta - 1$ at 694.3 nm is small compared to the electron contribution and therefore $\eta - 1$ from a 694.3-nm interferogram is sufficient to determine n_e using Eq. (III-15). A single-wavelength interferogram should also be sufficient to determine n_e at the shock center where $\rho \simeq 0$ and the temperature (and therefore ionization) is high. It is difficult to obtain information from single-wavelength $\eta(r,\lambda)$ from 50-torr data for $0 \lesssim r \lesssim R_s$ and at early times ($t \lesssim 1$ μs) because both the neutral gas contribution and electron contribution to η are significant.

Results

50-torr Results, $t > 1$ μs

The digitizing and inversion process for a 694.3-nm interferogram for a shock wave resulting from a 25.3-J laser shot in 50-torr air at 5 μs is shown in Fig. III-3. The right and left sides of the fringe indicated in Fig. III-3a have been plotted in Fig. III-3b after conversion from the graphics tablet coordinates to the radial coordinates. About 90 points were digitized in each half of the fringe. The left fringe was then smoothed and plotted in Fig. III-3c. Figure III-3d is a plot of $\eta - 1$ (where η is the index of refraction) after inversion of the curve in Fig. III-3c.

We can now determine the time evolution of the peak gas density and central electron number density for 50-torr shocks during $t \gtrsim 1$ μs, using interferograms from several shots where $E_L = 25 \pm 5$ J. Both histories are useful for comparison to the numerical calculations described in Chapt. V.

The previous section indicates that these shocks at this time have slowed to the point where dissociation of air in the shock front does not occur. Values of $K(694.3\ nm) = 0.225\ cm^3/g$ and $K(347.2\ nm) = 0.233\ cm^3/g$ are therefore appropriate when determining the gas densities in the shock front from the peak index of refraction. The assumption of negligible gas in the shock center should also hold at this time, making it possible to unambiguously determine the central electron density using Eq. (III-15).

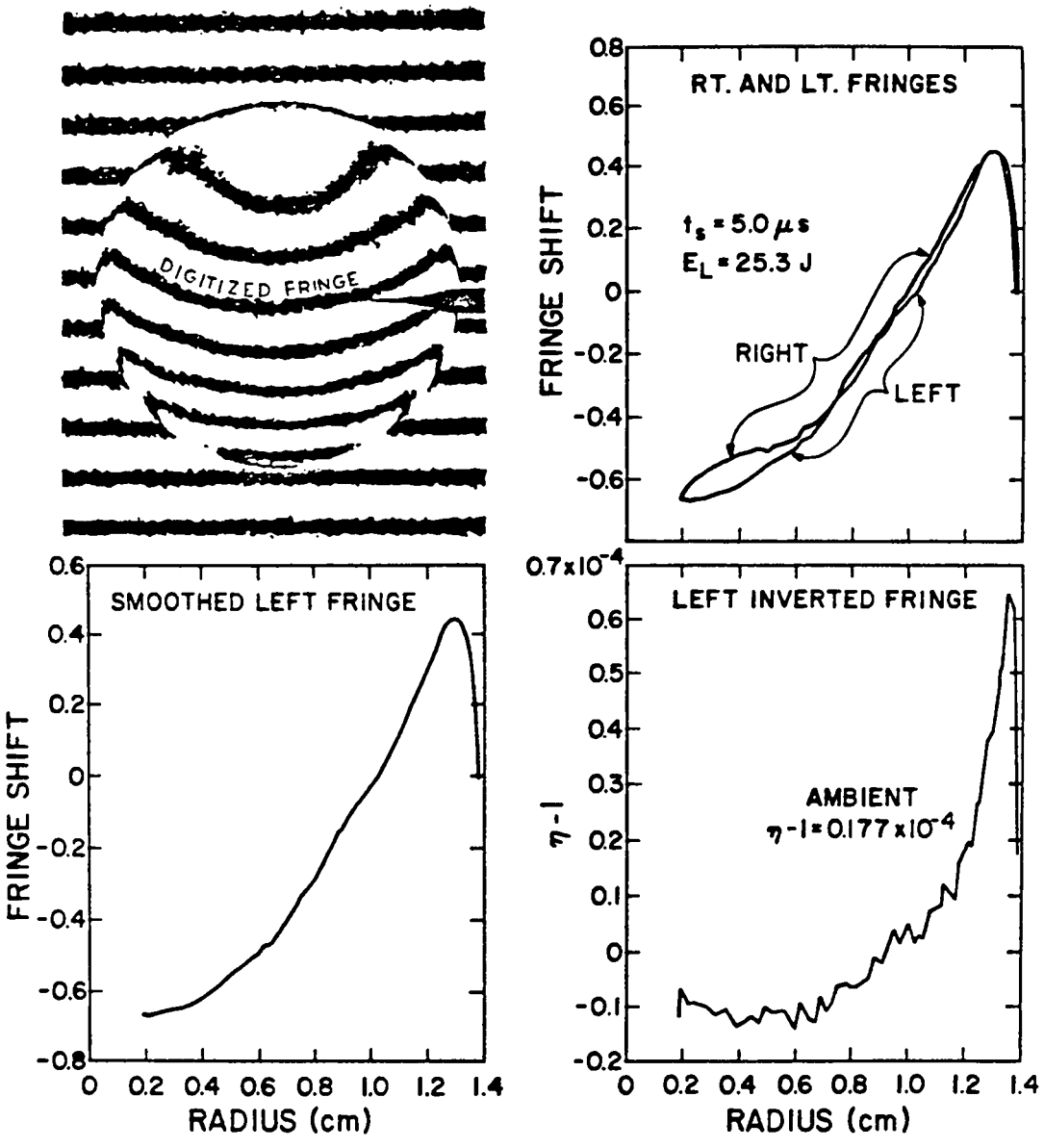

Fig. III-3. Example of interferogram reduction procedure, applied to a 694.3-nm interferogram of a 50-torr, E_L = 25.3 J shock at t = 5 μs:

(a) Fringe pattern.

(b) Superposition of left and right sides of digitized fringe.

(c) Smoothed left side.

(d) Abel-inverted left side.

If the determination of the density-evolutions from interferograms of shocks where $E_L = 25 \pm 5$ J is to be valid, we must first show that the densities at a given time are not strong functions of E_L over the range 20 to 30 J. Plots of the peak gas density and the central electron density at 2.5 μs vs laser energy, determined using the nondissociated-air values of K and Eq. (III-15), are given in Figs. III-4a and b. All values were obtained from 694.3-nm interferograms. The error bars were determined by the variation in the values obtained from several fringes of a given interferogram passing through the shock near its center. The peak gas density varies only slightly for laser energies between 0.5 and 27.6 J. The central electron density varies nearly linearly with laser energy up to ~ 15 J and levels off for $20 \lesssim E_L \lesssim 30$ J. In both cases the densities are independent of E_L in the range of 20 to 30 J at t = 2.5 μs. We will assume that the peak gas density and central electron densities are independent of E_L in the range of 20 J to 30 J for $1 < t < 30$ μs. This allows comparison of density data at different times, obtained from several laser shots of slightly different E_L. If at times other than 2.5 μs there is as much as a linear variation in the densities with E_L, then the error in the densities over $E_L = 25 \pm 5$ J is still only ± 20% and the assumption is still not too bad.

The evolution of the peak gas density and central electron number density are plotted in Figs. III-5a and b, respectively, as determined independently from both 347.2-nm and 694.3-nm interferograms. The relation $\rho = (n - 1)/K(\lambda)$ (assuming no electrons present) was used to determine the peak gas density and

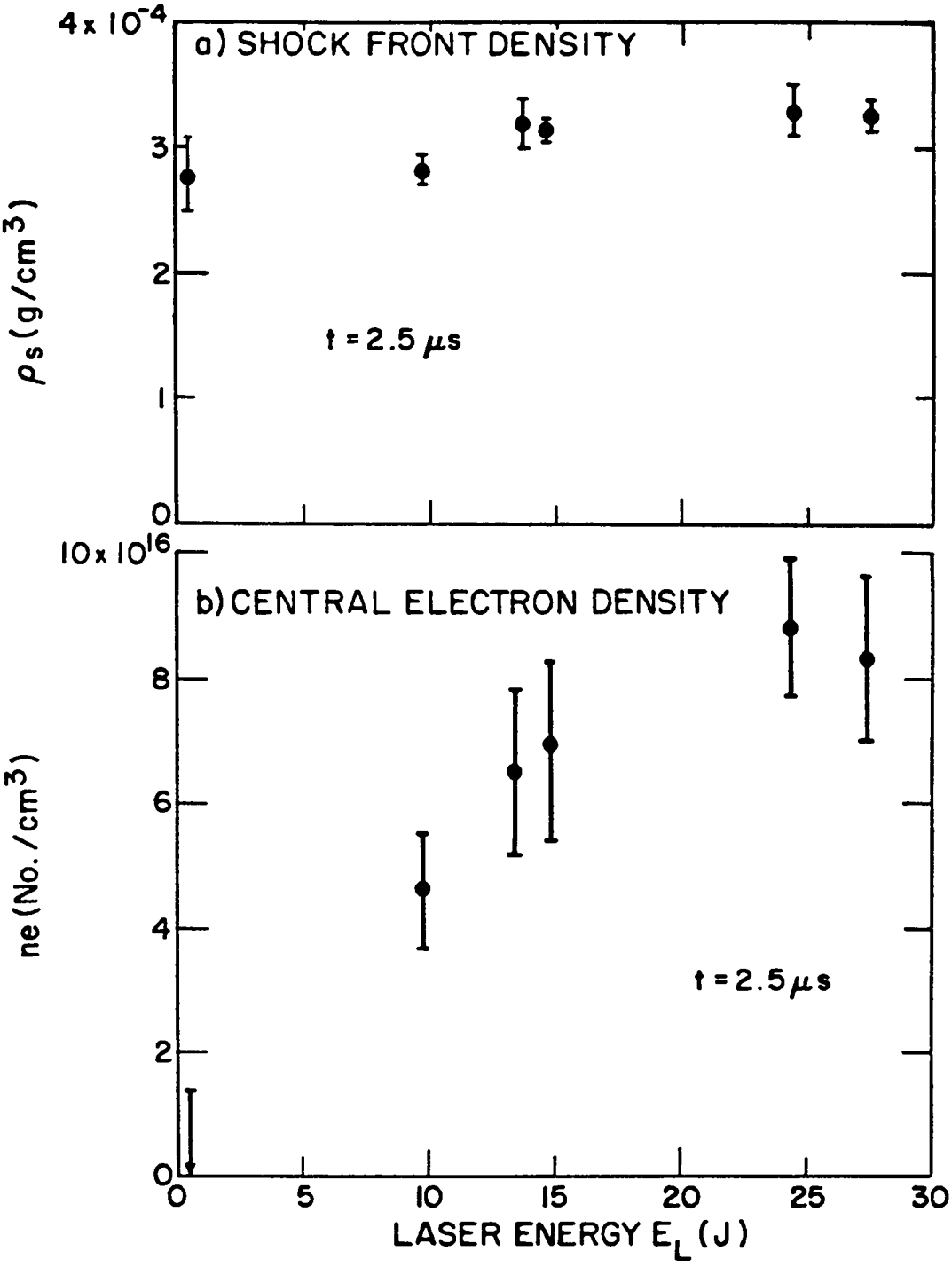

Fig. III-4. Plots showing measured variation of (a) shock front density, and (b) central electron number density of 50-torr, 2.5 μs shocks as functions of laser energy.

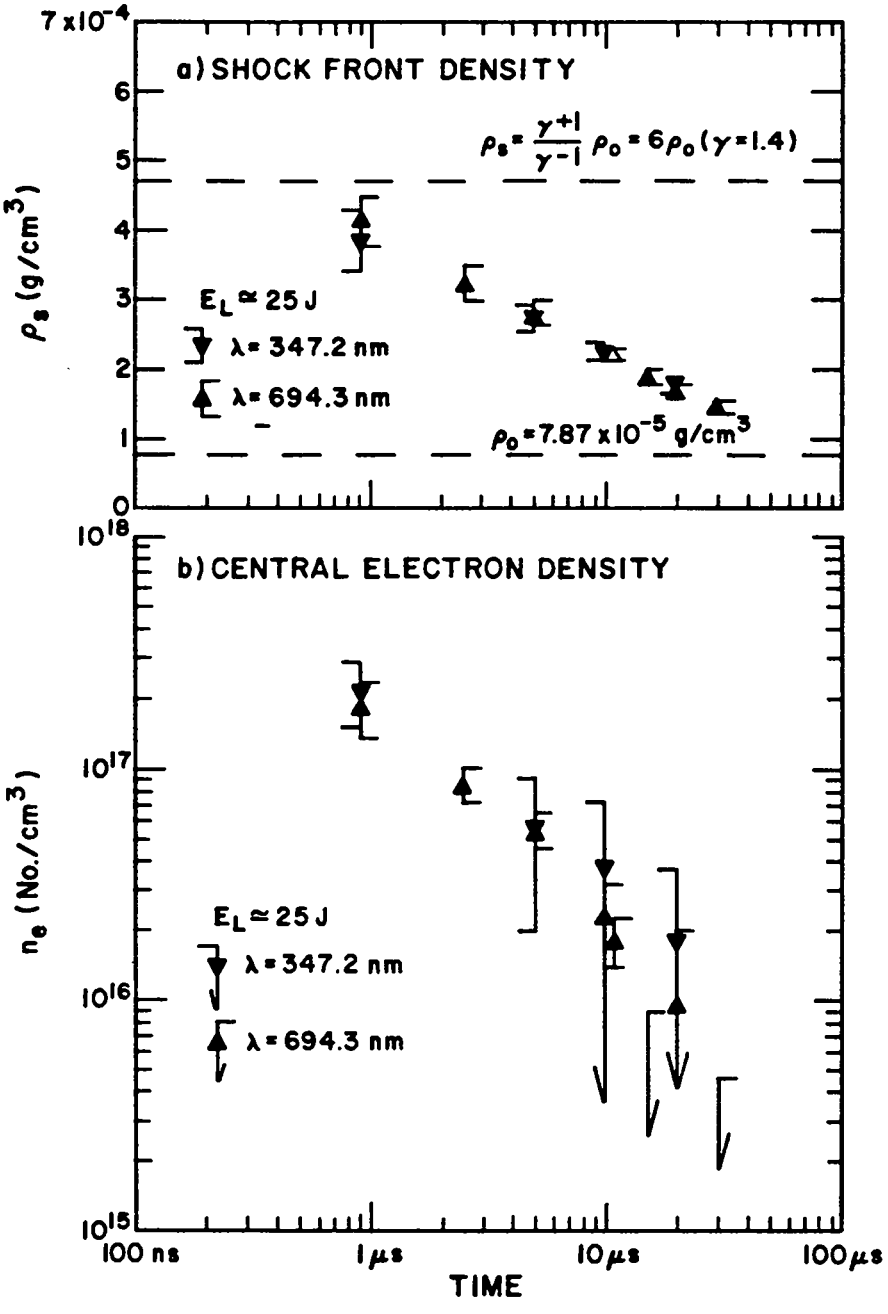

Fig. III-5. Composite of two-wavelength interferogram measurements of (a) shock front gas density, and (b) central electron number density for 50-torr shocks with $E_L = 25 \pm 5$ J.

Eq. (III-15) (assuming negligible atomic and ionic contributions to $\eta - 1$) was used to determine the central electron number densities. The assumptions are supported by the agreement between the 347.2-nm and 694.3-nm density determinations.

It is notable that after 1 μs, the measured peak gas densities are well below $6\rho_0$ predicted by Eq. (III-21) with $\gamma = 1.4$. This confirms the assumption that the effects of dissociation can be ignored after 1 μs. It is also interesting that $\rho_s < 6\rho_0$ for 1 μs $\leq t \leq$ 10 μs because it was found in Chapt. II that $R_s \propto t^{0.4}$ over this time period. Although the assumption of a strong shock therefore does not hold, the dimensional relatioinship between t, R_s, ρ_0, and E_s apparently does still hold. That is, the shock can be weak in terms of the shock-front density and still expand self-similarly.

50-torr Results, $t < 1$ μs

The 50-torr data at times earlier than ~ 1 μs are difficult to interpret. The shock is somewhat ellipsoidal (we still fit circles to the shock boundaries during interferogram reduction) and fringes crossing the side of the shock toward the Nd:glass laser beam are noticeably different than those crossing the opposite side.

Fringes crossing the side of the shock away from the Nd:glass laser, when inverted, yield radial index-of-refraction profiles similar to those for times greater than 1 μs. The peak gas density at t = 430 ns of a 50-torr shock with E_L = 20 J determined from two-wavelength interferograms using Eq. (III-17) with K = 0.275 was $\rho_s = 5.4 \pm 0.4 \times 10^{-4}$ g/cm^3. Therefore $\rho_s \simeq 7\rho_0$. From Eq. (III-16), the electron density at the shock front was determined to be

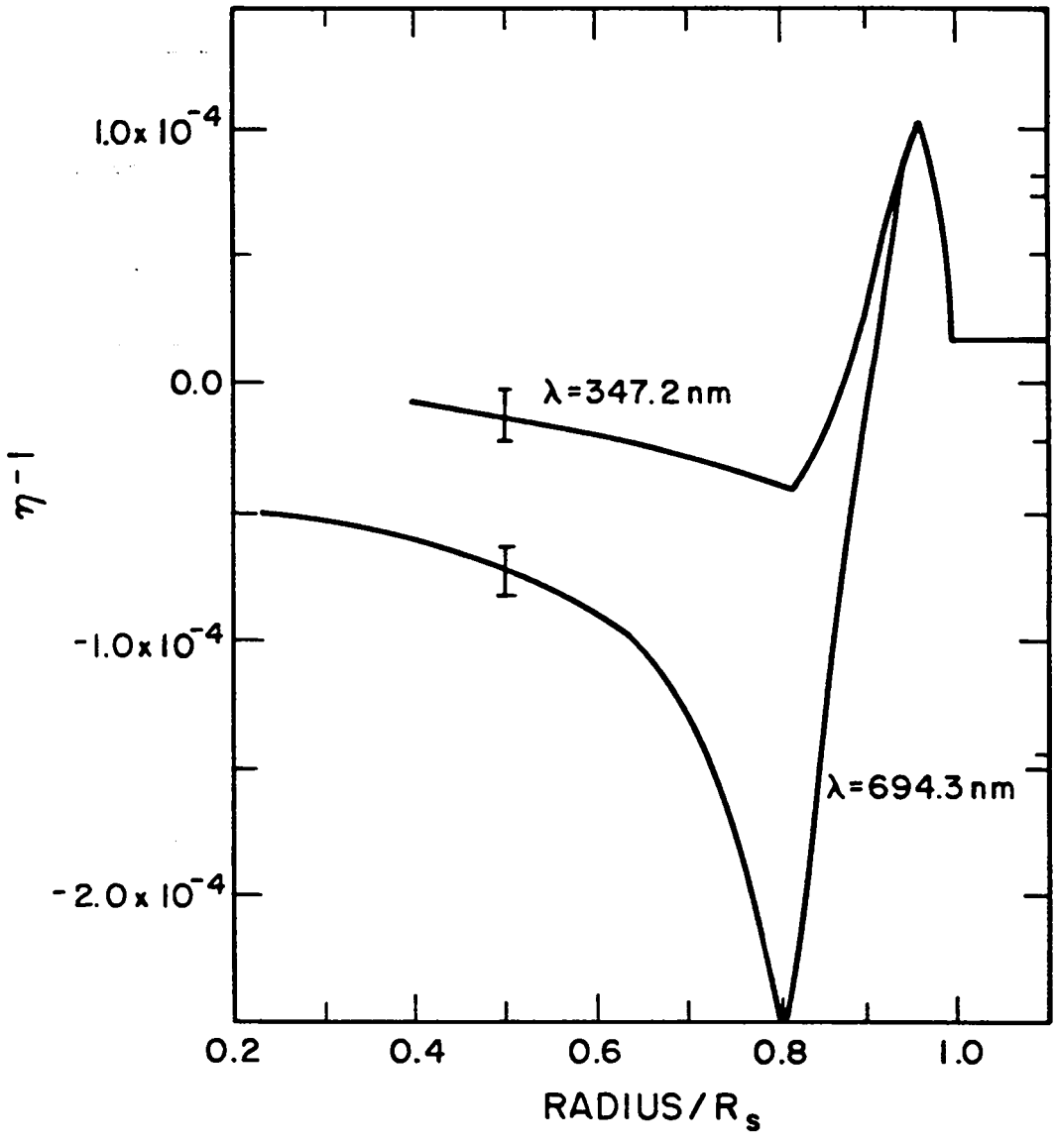

Fig. III-6. Results of Abel-inverting 347.2-nm and 694.3-nm fringes of a 50-torr shock with E_L = 20.3 J at t = 428 ns. R_s = 0.51 cm.

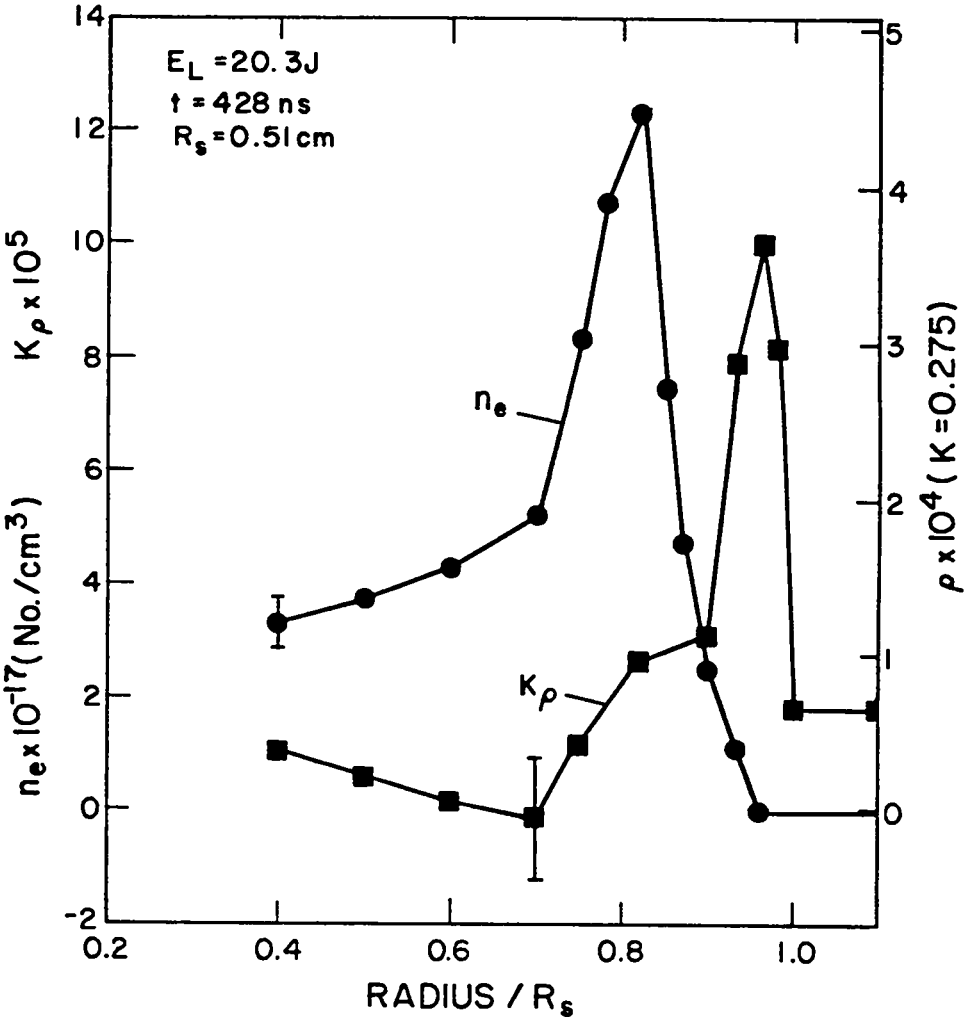

Fig. III-7. Profiles of electron number density (dots) and gas density (squares) that result from unfolding the η-1 profiles of Fig. III-6.

$1.7 \pm 0.8 \times 10^{17}/cm^3$. The central gas density was below measurable limits, and the central electron density was $4.66 \pm 0.23 \times 10^{17}$.

The shock velocity at t = 430 ns for the E_L = 20 J shock was determined to be 4.6×10^5 cm/s. With $\dot{R}_s = 4.6 \times 10^5$ cm/s, Gilmore's (1955) graphs of Hugoniot curves for shocks in 50-torr air yield $T_s \simeq 0.5$ eV and $\rho_s \simeq 10\rho_0$. The Hugoniot density ratio is higher than the measured value and there is little ionization of air at T_s = 0.5 eV, indicating that the measured shock front value of n_e is much higher than is consistent with the velocity measurement.

A possible cause of the discrepancy is the loss in accuracy of the Abel inversion technique and the error in the fringe shift measurement resulting from the asphericity in the shock. The central electron number density value is probably accurate because the change in fringe shift with radius is not as great in the center, minimizing the effects of any error in the radius value for a given fringe-shift measurement. The use of Gilmore's curves for determining the shock temperature is also questionable at 430 ns because the shock wave is stil forming from the target plasma. The 50-torr shocks do not show self-similar R_s-vs-t expansion until ~ 1 μs.

There is also a possibility that the air surrounding the target is preheated either by the scattered Nd:glass laser beam or by radiation from the target plasma, thus accounting for the elevated ionization levels. Spherical numerical calculations in Chapter V indicate very little radiation preheat; however, scattered Nd:glass laser beam preheat is not ruled out.

Fringes crossing the side of the shock toward the Nd:glass laser yield the radial index-of-refraction curves plotted in Fig. III-6. These curves have been smoothed by eye after comparing results from several inverted fringes. Figure III-7 gives n_e and $K\rho$ calculated from the data of Fig. III-6 using Eqs. (III-16) and (III-17). The right-hand side in Fig. III-7 is the density assuming a constant K = .275. Again, there may be a considerable underestimate in the value of the peak gas density due to inversion inaccuracy caused by asphericity at early times.

The shock density-profile on the shock-side toward the Nd:glass laser does not resemble that of an $R_s \propto t^{0.4}$ self-similar shock wave. Once again, this is not in disagreement with the radius-vs-time data of Fig. II-7 that indicate the shock expansion is just beginning to show an $R_s \propto t^{0.4}$ dependence. Particularly notable is the bump on the back of the density peak at r/R_s = 0.7 to 0.9. The portion of the shock away from the Nd:glass laser does not show this bump. Both sides of the shock have electron densities near the center of 3 to 5 x $10^{17}/cm^3$. The side towards the Nd:glass laser, however, exhibits a peak in electron density at about 0.8 R_s of 1.2 x $10^{18}/cm^3$. These features may be due to the laser-air breakdown or the manner in which the target material expands and forms the air-shock as discussed in Chapts. IV and V. Errors from the Abel inversion technique may also be significant.

1-torr Data

A 1-torr 694.3-nm interferogram of an E_L = 18.7-J laser shock at t = 0.6 μs is reproduced in Fig. III-8. The orientation of the

Fig. III-8. 694.3-nm interferogram of a 1-torr, E_L = 18.7 J shock at t = 600 ns.

picture is such that the B-beam enters from above. The fringe shift pattern is similar to the 50-torr pattern; however, the fringe shift is in the negative direction (compare with Fig. II-1a).

Results from inverting the 1-torr fringes near the target stalk are different than results for fringes away from the stalk. The variation is the result of the distortion of the shock front by the target stalk. The shock front away from the stalk also appears slightly irregular as seen in Fig. III-8. If only fringes that are unperturbed by the stalk are used, the average peak value of $\eta - 1$ from several 20-J laser shots is $-4.4 \pm 0.7 \times 10^{-5}$. The expected contribution to $\eta - 1$ at the shock front from the air atoms and ions is $\sim 4 \times 10^{-6}$ assuming $\rho_s = 10\rho_o$. The electron contribution is 10 times greater and negative and therefore dominant as expected. The central value of $\eta - 1$ is $-1 \pm 1 \times 10^{-6}$, corresponding to a central n_e of $4.6 \pm 4.6 \times 10^{15}/cm^3$.

The higher degree of ionization is due to the higher temperature resulting from a larger shock velocity at a given time in lower density air for the same E_s. This is seen by comparing Eqs. (III-21) to (III-24) that show $T_s \propto \dot{R}_s^2 \propto R_s^2 \propto 1/\rho_o^{2/5}$. Decreasing the density by a factor of 50 increases T_s by 4.8.

We can also make a purely theoretical calculation of $\eta - 1$ through the shock front for comparison with the experimental data. The comparison is useful because the calculation will be based on ideal density and pressure profiles from the solution for an instantaneous point energy release.

To calculate an analytical $\eta - 1$ profile we first assume that the strong shock Hugoniot equations [Eqs. (III-21) and (III-22)]

hold for some effective γ and that $R_s \propto t^{2/5}$. We have measured values of R_s and t and therefore [by Eq. (III-24)] $\dot{R}_s$. To find the value of γ that is consistent with the R_s and t data and the EOS tables, we combine Eqs. (III-21) to (III-24) and get

$$\frac{p_s}{\rho_s} = \frac{4}{25} \frac{2(\gamma - 1)}{(\gamma + 1)^2} \left(\frac{R_s}{t}\right)^2 = (\gamma - 1)\varepsilon \quad . \qquad \text{(III-26)}$$

The second equality is simply the result of $(\gamma - 1) = p/\rho\varepsilon$. Equation (III-26) permits us to calculate ε for R_s, t, and γ. We first assume $\gamma = 1.2$ to calculate ε from Eq. (III-26) and ρ from Eq. (III-21). With the calculated ε and ρ values, we can find a new value of γ using Fig. III-2a. We then repeat the process with the new value for γ. After several iterations we obtain a value of γ consistent with the R_s and t data as well as the EOS table. For R_s = 1.78 and t = 0.6 μs, $\gamma - 1 = 0.145$. The last value of ε can be used with Fig. III-2b to find T_s. The final values after the iteration are $\rho_s = 14.8\ \rho_0 = 2.34 \times 10^{-5}$ g/cm^3, $p_s = 2.08 \times 10^6$ dynes/cm^2, and T_s = 13200 K.

The values of p, ρ, and T behind the shock front can now be calculated. Equation (A-3) can be used for an approximation to $\rho(r)$. Taylor (1950) similarly derives an approximate expression for p(r) given by

$$p(r) = cf(r)/\gamma \quad , \qquad \text{(III-27)}$$

where

$$f(r) = \exp\left[\ell n\left(\frac{2\gamma}{\gamma + 1}\right) - \left(\frac{2\gamma^2 + 7\gamma - 3}{7 - \gamma}\right)\ell n\left(\frac{\gamma + 1 - r^{h-1}}{\gamma}\right)\right] \quad . \quad \text{(III-28)}$$

Here r and h have the same meanings as in Eq. (A-3). The constant c in Eq. (III-27) is determined by evaluating f at r = 1 and setting Eq. (III-27) equal to p_s, derived from Eq. (III-26). Both ρ and p are plotted in Fig. III-9a for normalized radii of $0.85 \leq r \leq 1.0$, $\gamma = 1.145$, $p_s = 2.08 \times 10^6$ dyne/cm^2 and $\rho_o = 1.58 \times 10^{-6}$ g/cm^3. By assuming γ is constant through the shock front, ε can be determined from $\varepsilon = p/\rho(\gamma - 1)$ and Fig. III-2b can then be used to determine T(r) from ε and ρ. T(r) and the quantity $p/\rho(\gamma - 1)$ are plotted in Fig. III-9b. The assumption that γ is constant throughout the plotted range of ε is justified because the value of γ derived from Fig. III-2a for values of ε and ρ at r = .86 is 1.153. Despite the constancy of γ, the values of $T \gtrsim 5$ eV ($r \lesssim .9$) are probably not believable.

Equation-of-state tables can now be used to find the electron number density, n_e, from the curves in Fig. III-9. Tables from Gilmore (1955) and Gilmore (1967) were used to find the electron densities. The electron density was also calculated from $p = (n_e + n_p)kT$ where n_p is the heavy particle (N, O, N^+, etc.) number density calculated from $n_p = 2 N_A\rho/M_w$. The calculated n_e agree with the EOS value within ~ 30% over $0.87 \leq r \leq 1.0$. Both the calculated and EOS values of n_e are plotted in Fig. III-10 along with n_p.

The electron contribution to $\eta - 1$ can now be calculated from Eq. (III-15). The contribution from the air atoms and ions is $\eta - 1 = K\rho$ where K was taken as 0.275 for dissociated air. Because the air

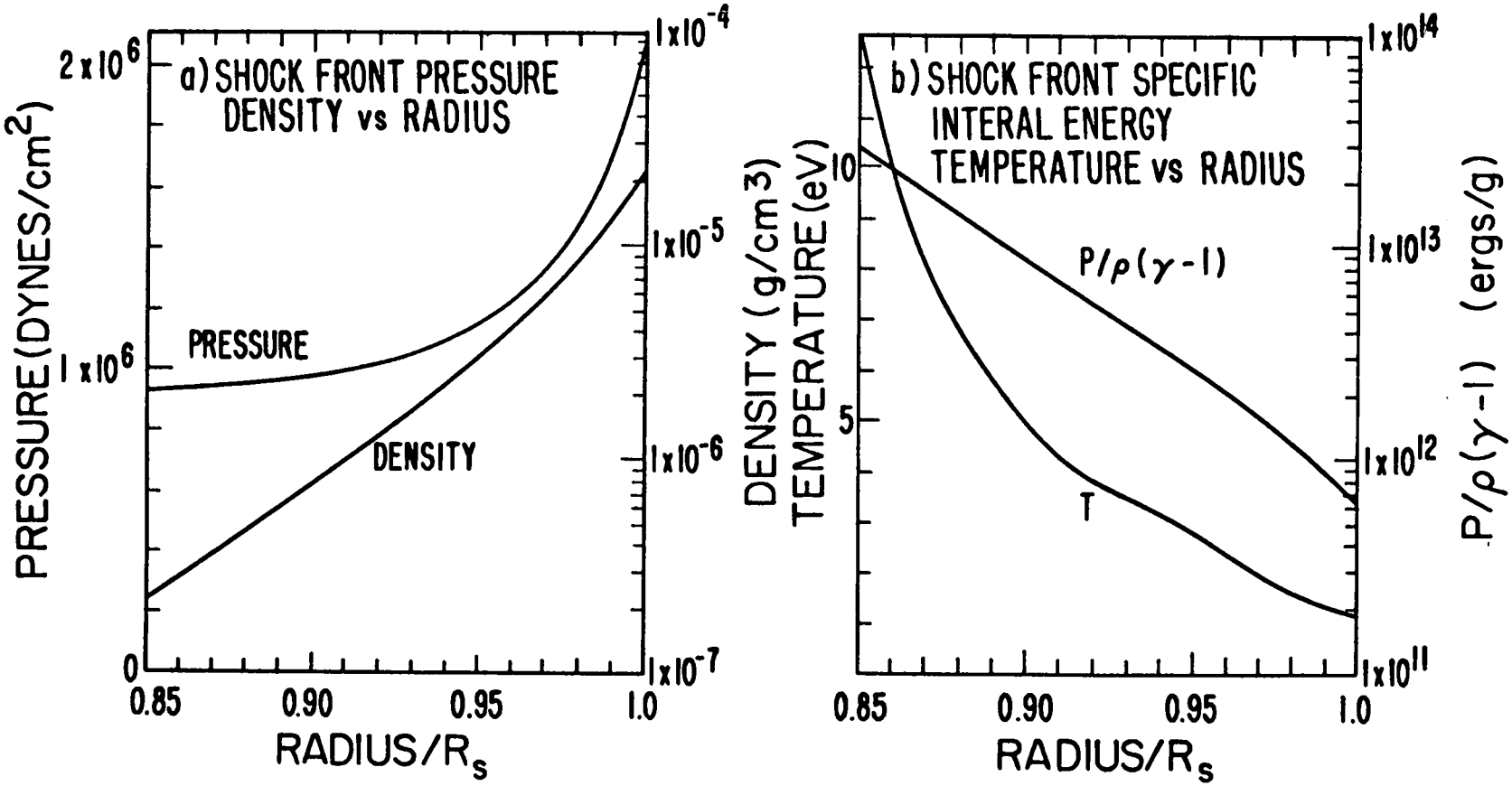

Fig. III-9. (a) Pressure and density profiles through a 1-torr shock front, calculated from Taylor's approximate equations.

(b) Specific internal energy, ε, through the shock front, calculated from results of (a) above and temperature T taken from EOS tables.

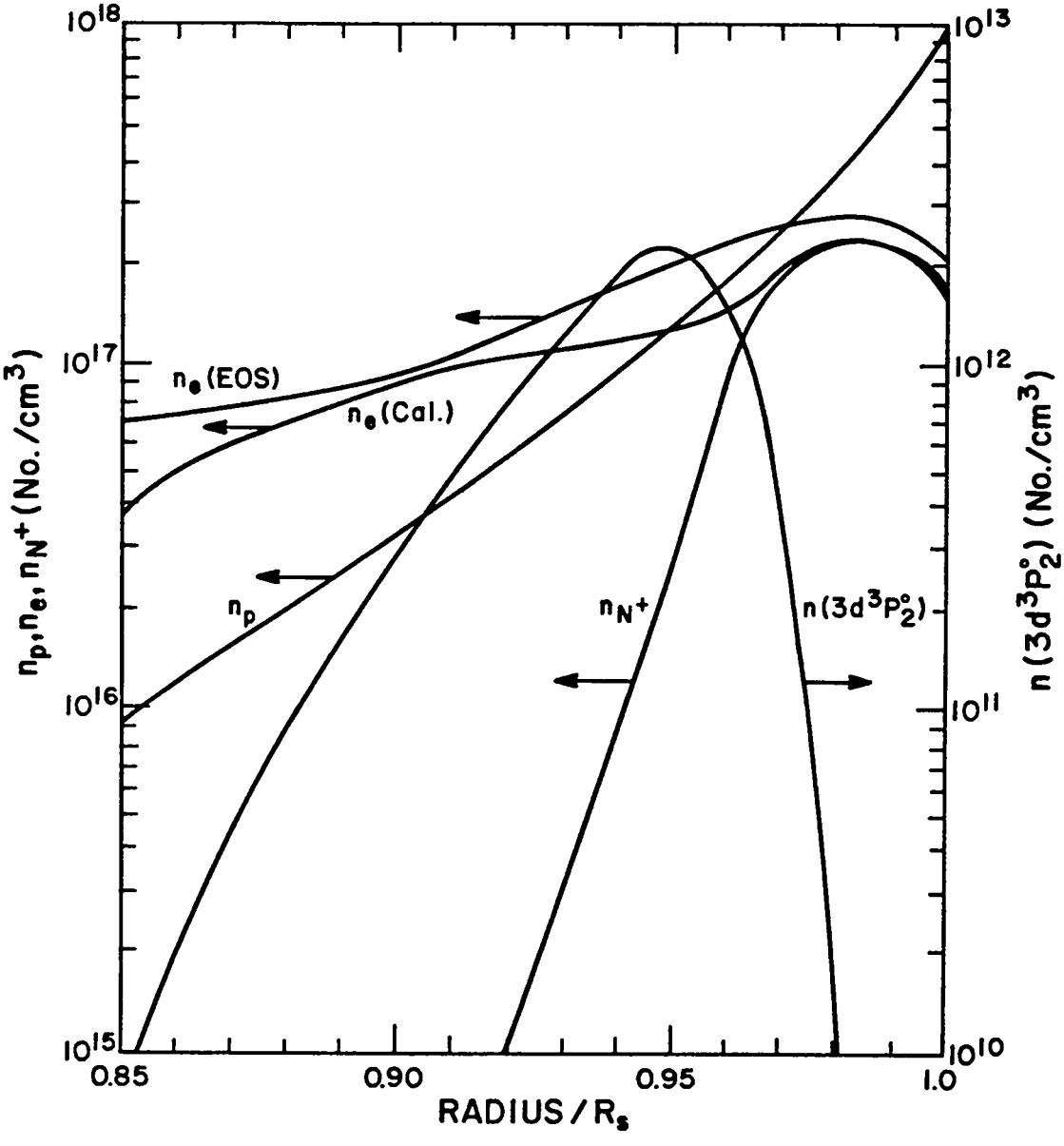

Fig. III-10. Number densities of components in the shock front that affect the index of refraction.

atoms are ionized, this value is probably not quite correct. The number density of the N^+ ions in the $3d^3P_2^o$ level was also determined from Eq. (III-20) and the profile is plotted in Fig. III-10. This permitted the addition of $\eta - 1$ due to anomalous dispersion although it is slight.

The total $\eta - 1$ is taken as the sum of these three contributions and is plotted in Fig. III-11 along with the experimental points from an inverted fringe of Fig. III-7. The values of n_e calculated from $p = nkT$ were used in compiling $\eta - 1$. The agreement is good even without the error bars. The error bars were determined from the variation in the measured peak $\eta - 1$, and are probably an overestimate for the rest of the experimental curve. If the EOS values for n_e were used, $\eta - 1$ would typically be 15% more negative than the values from the calculated n_e.

Summary

Chapter III and Appendix B describe the procedures used to interpret and reduce the interferograms. Spline fitting and smoothing tecnniques are applied to the fringe shift-vs-position data acquired by tracing the fringes on a computer-coupled graphics tablet. The profiles are then Abel-inverted to obtain the index of refraction-vs-radius.

Analytical shock predictions and equation-of-state tables are used to indicate the need for interferograms at two wavelengths in separably determining the gas and electron densities--that is, when both electron density and gas density are significant in the same region of the shock.

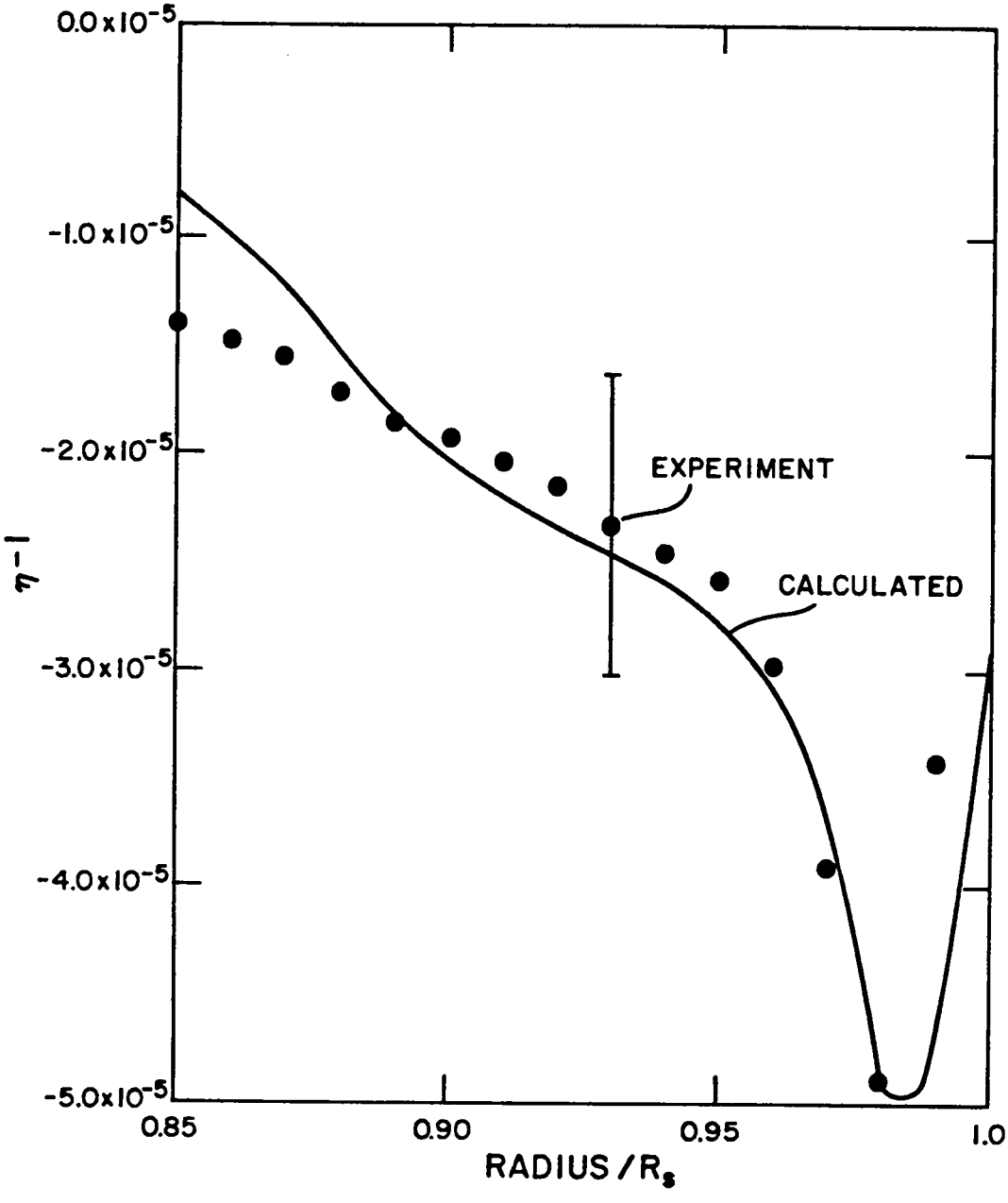

Fig. III-11. Comparison of the η-1 calculated from the number densities of Fig. III-10 (solid line) and the measured η-1 (dots).

The 50-torr data at times greater than 1 μs give peak densities which appear to be consistent with the radius-vs-time data. The 50-torr value of ρ_s/ρ_0 at 1 μs is about 5, in approximate agreement with $(\gamma + 1)/(\gamma - 1) = 6$ for $\gamma = 1.4$ as predicted for a strong shock. The value $\gamma = 1.4$ for nondissociated air is consistent with the shock-front temperatures inferred from the 50-torr shock-wave velocities for $t \gtrsim 1$ μs. The 50-torr shocks no longer expand in a self-similar way after ~ 10 μs. At t = 10 μs, the data give ρ_s/ρ_0 ~ 3, and at later times ρ_s/ρ_0 approaches 1 (t ~ 30 μs).

The values for the index of refraction at the 50-torr shock center indicate that there is little gas at the shock center ($\lesssim 1 \times 10^{-5}$ g/cm^3) over the time span of 1 to 30 μs and the electron density is as high as 2×10^{17}/cm^3 at 1 μs. If the electrons resulted from singly ionized air atoms, the central gas density would be ~ 0.5×10^{-5} g/cm^3, which is below the detectable limit and therefore consistent.

Data at 50 torr and times earlier than 1 μs indicate asymmetries caused by the laser-air breakdown and one-sided target illumination are still present. The gas density profile is broader and not as peaked as expected from the self-similarity solution. The error in the peak value is probably due to a combination of asphericity and the Abel inversion process. If the shock is still forming, this would also result in a broader shock front. This agrees with the radius-vs-time data, which show that the shock is not yet expanding as $R_s \propto t^{0.4}$. Central electron densities are 3 to 4 $\times 10^{17}$/cm^3 for data at t = 428 ns, so that any air atoms in the center are probably ionized.

The 1-torr data taken at 600 ns is at a single wavelength (694.3 nm); however, the high degree of ionization makes it possible to determine $n_e(r)$. Theoretical index-of-refraction profiles constructed from the shock radius at a given time, equation-of-state tables for air, strong-shock Hugoniot pressure and density relations, and the approximate density and pressure profiles of Taylor agree well with the experimental profile over the outer 15% of the shock radius.

CHAPTER IV

INITIAL TARGET EXPANSION AND SHOCK FORMATION

In this chapter, we will consider several features of the plasma during the early expansion that tend to make the expansion deviate from that of the instantaneous point-energy release described by the Taylor-von Neumann-Sedov solution.

We will first consider the suggestion of Basov et al. (1973), regarding experiments similar to ours, that nonlinear electron heat transport may be influential in the early expansion. The effect is found to be slight. The difference between the target material equation of state and the air equation of state are also considered and are found to produce only slight differences in the initial expansion.

With the finding that electron heat transport and target equation-of-state (EOS) can have only a slight effect on the shock formation, we assume that the early expansion is simply ideal-gas fluid motion. We also assume that the target EOS is identical to that of air. Deviations from the Taylor-von Neumann-Sedov solution are therefore assumed to be due to the presence of the target mass.

The experimental results are then compared with several existing analytical approximations that include source mass. The comparisons are made in terms of overall R_s-vs-t agreement, convergence to the

Taylor-von Neumann-Sedov solution at large R_s and/or negligible source mass, and the radius of maximum deceleration, R_D, previously defined in Chapt. II.

Finally, a description of the shock formation is given in terms of variable-energy blast waves. This description is expanded upon by assuming a special case where the uniformly heated target mass forms an isentropic gas that supplies the shock front with energy.

The features of target mass and heat transport will be examined in spherical symmetry; the existence of asymmetry must be kept in mind when comparing theory and data.

Electron Heat Transport

When nonlinear diffusive transport of heat is significant, a plasma volume can expand very quickly. Although the boundaries of the plasma volume expand, the fluid does not have time to be accelerated and remains essentially motionless. The temperature of the target material after laser irradiation is too low for much diffusive radiation transport to occur, however, the initial plasma expansion by diffusive electron heat transport into the surrounding air has been suggested by Basov et al (1973). We will therefore examine the influence of nonlinear electron heat transport here.

The radius of the front of a spherical nonlinear thermal conduction wave propagating in a uniform medium may be estimated from the similarity solution given by Zel'dovich and Raizer (1966) as

$$R_f = 0.953(aQ^{5/2}t)^{2/19} \quad . \qquad \text{(IV-1)}$$

Equation (IV-1) assumes that the coefficient of thermal diffusivity is $\chi_e = aT^{5/2}$, where a is a proportionality constant. R_f is the radius of the thermal front, and $Q = E/\rho C_v$ is the released energy divided by the density and heat capacity at constant volume. The heat flux due to electron transport is $F_s = -K_e \nabla T_e = \sigma \delta_T K_L \nabla T_e$ [Spitzer (1962)] where $\sigma \simeq 0.4$ and K_L is the conductivity of a Lorentz gas. δ_T can be fit by [Edwards, et al (1973)]

$$\delta_T = \left(1 + \frac{3.44 + 0.26 \ln Z}{Z}\right)^{-1} \qquad \text{(IV-2)}$$

where Z is the average ion charge. After substituting for K_L (from Spitzer),

$$F_s = -7.81 \times 10^{-5} \frac{T_e^{5/2} \nabla T_e}{\ln \Lambda (Z + 3.44 + 0.26 \ln Z)} \text{ (ergs/cm-s-deg)} \qquad \text{(IV-3)}$$

where Λ is the Coulomb logarithm and T_e is in Kelvins. The value of a is determined from $a = \chi_e / T^{5/2} = K_e / C_e T^{5/2}$ by comparing Eq. (IV-3) with $F_s = -K_e \nabla T_e$, where C_e is the specific heat of the electron gas per unit volume at constant volume. Equation (IV-1) then becomes

$$R_f = 2.11 \times 10^5 \left[\frac{E^{5/2}}{\ln \Lambda (Z + 3.44 + 0.26 \ln Z) Z (Z+1)^{5/2}}\right]^{2/19} \left(\frac{t}{n_p^{7/2}}\right)^{2/19} \qquad \text{(IV-4)}$$

I have used $C_v = 3n_t k/2\rho$, $C_e = 3n_e k/2$, and the total particle density $n_t = n_p = n_e = (Z + 1)n_p$, where n_p is the heavy particle number density (atoms and ions) and n_e is the electron number

density, which is assumed to be independent of temperature for the purpose of approximation.

We can use Eq. (IV-4) to estimate R_f vs t for typical conditions of our experiment. Assuming a pressure of 10-torr air, $n_p = 6.6 \times 10^{17}$, and assuming $E = 10^8$ ergs, $Z = 1$ and $\ell n\, \Lambda \sim 10$, then $R_f = 0.5$ cm at 1 ns.

For comparison with the experimental data, Eq. (IV-4) gives an overestimate of the wave-front radius because the energy is deposited in the massive target, not the ambient air, and therefore Q is initially lower. Furthermore, Eq. (IV-4) implicitly assumes that n_e is constant throughout the entire chamber instead of just in the region of the target.

For large ∇T_e, Eq. (IV-3) can yield flux values that are larger than the maximum flux that can be carried by a given number of electrons. Assuming the electron velocities v_e fit a Maxwellian distribution, the limiting flux is given by

$$F_L = \sigma \bar{\mu} n_e \langle 0.5\, v_e m_e v_e^2 \rangle = 2\sigma \bar{\mu} n_e \sqrt{8/\pi m_e}\, (kT_e)^{3/2}$$
$$= 3.42 \times 10^{-11} n_e T_e^{3/2} \qquad \text{(IV-5)}$$

where $\sigma = 0.4$ and $\bar{\mu}$, the average cosine of the angular distribution, has been taken to be 1/2.

The EOS tables indicate that depositing 10 J in the target mass leads to $T_e \sim 3.5 \times 10^5$ K and $n_e \sim 10^{22}$ to 10^{23}. The large electron density in the target implies that the surrounding air is immediately heated to 3.5×10^5 K. The maximum electron density in the air is only $\sim 10^{19}$ if it is totally ionized and from Eq. (IV-5), $F_L \sim 7 \times$

10^{16} ergs/cm^2-s. If the plasma radius is about 0.025 cm, then in 1 ns only $\sim 6 \times 10^5$ ergs or 0.5% of E is transferred away from the plasma. It would therefore take tens of nanoseconds for the plasma volume to double by heat transport. However, a fluid velocity of only $\sim 2 \times 10^5$ cm/s is necessary to double the volume in the same time by plasma motion.

This discussion indicates the electron heat transport does not play an important role in the expansion. It may be important for initial transport of energy within the target material, but this period is short lived.

Target EOS

It was pointed out in relation to Eq. (II-7) that, although the "effective γ" of air is a function of temperature, the variation of γ has little effect on the R_s-vs-t relation. The R_s-vs-t relation is also insensitive to any differences between the effective γ of the $(CH)_n$ and that of air. Figure IV-1 is a comparison of the air EOS for $\rho = 1.29 \times 10^{-3}$ g/cm^3 taken from Fig. III-2a and the EOS for polystyrene obtained from the Los Alamos Equation-of-State Library [Bennett et al. (1978)] for $\rho = 1.29 \times 10^{-3}$ g/cm^3. The agreement is good in the regime of the experiment ($\varepsilon \gtrsim 3 \times 10^{12}$ ergs/g, where ε is the specific internal energy).

The approximate curve in Fig. IV-1, and several variations where the ε-value of the $\gamma - 1 = 0.4$ cross-over was shifted, were tried for the target EOS using the numerical model of Chapter V. The results were nearly identical to calculations that assumed an air

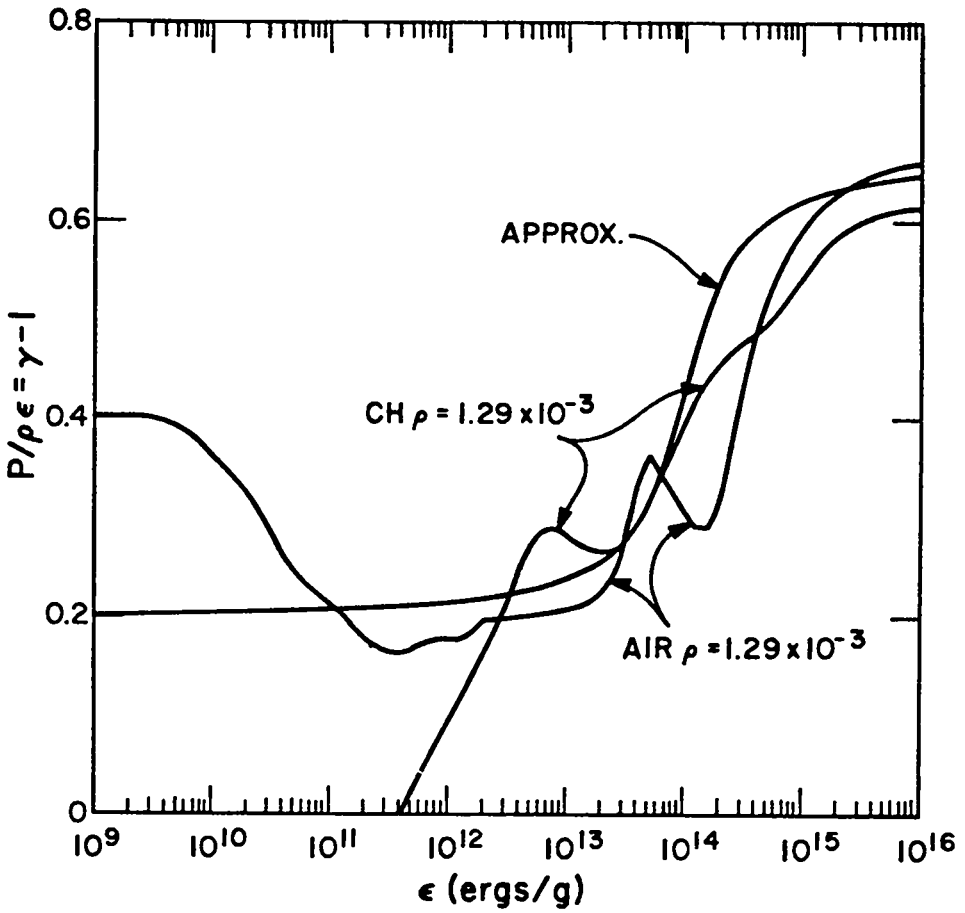

Fig. IV-1. Comparison of EOS for CH with the EOS for air and the approximate EOS for the target material used in the numerical calculations.

EOS for the target. Therefore, the target EOS was taken to be that of air for the numerical calculations of Chapter V.

We can conclude that the target material behaves essentially like air in the region of the equation-of-state that is of interest in this experiment.

Approximations That Include Target Mass

The mass can affect the expansion in two ways. After the energy is deposited, the mass can expand outward, pushing the ambient air ahead of it (or "snowplowing" it). In the second effect, the shock develops within a distribution of mass and propagates through the distribution into the ambient air, whether the mass itself is expanding or stationary.

In the case of a simple momentum-conserving snowplow with initial target mass M_T and velocity V_o, it is easy to show that the relation between R_s and t for a uniform ambient atmosphere is

$$R_s + \frac{\pi}{3}\frac{\rho_o}{M_T} R_s^4 = V_o t \quad , \qquad \text{(IV-6)}$$

or, in terms of the initial kinetic energy, $E_k = (1/2)M_T V_o^2$,

$$R_s + \frac{\pi}{3}\frac{\rho_o}{M_T} R_s^4 = \sqrt{\frac{2E_k}{M_T}}\, t \quad . \qquad \text{(IV-7)}$$

When R_s is small, the first term will dominate until R_s^4 becomes large enough to overcome it; thus, the expansion will be approximately linear for early times. It is also possible to consider the snowplow passing through an arbitrary ambient density distribution,

as in the case of a portion of the target mass being dispersed and the snowplow passing through it. This would add an additional term to Eq. (IV-7). The initial velocity is proportional to $\sqrt{E_k}$ for this solution. The main problem with this solution occurs at late times, when $R_s \propto t^{1/4}$, in disagreement with the $t^{2/5}$ dependence indicated by the data and the self-similar solution for a point explosion. The momentum conserving snowplow solution is further deficient in not considering the internal energy. The data shows E_k/E_s is at most 30%, assuming the target and shocked air mass are in a shell moving with the shock wave expansion velocity. It can be < 10%, so this is a significant omission.

The internal energy can be taken into account and a self-similar solution derived for a shock propagating through a particular density distribution of the form $\rho = \rho_0/r^w$, where ρ_0 is a constant, w a number, and r the radial distance. This approach is discussed by Sedov (1959), and yields the R-vs-t relation

$$R_s = \lambda \left(\frac{E_s}{\rho_0}\right)^{1/(5-w)} t^{2/(5-w)} \quad , \qquad \text{(IV-8)}$$

where λ is the similarity variable. For $w > 3$, the shock radius actually accelerates and the total mass in the density distribution is finite. For a constant velocity (where $w = 3$), the velocity is again proportional to $\sqrt{E_s}$. It is conceivable that, if the target mass was dispersed and a shock generated within, the shock would show little change in velocity as it broke through the density gradient. Because this solution is applicable to special distributions, it can provide only qualitative information.

Two approximate solutions [Freiwald and Axford (1975) and Fuchs (1947)] will be compared to the data. Both solutions assume that the shocked material is in a shell which is thin compared to the radius of the shock wave, and further assume zero counterpressure. They both have the property that they approach the $R_s \propto t^{2/5}$ dependence at large distances.

The Freiwald/Axford Approximation

The first approximation [Freiwald and Axford (1975)] assumes that the heated mass expands as a contact surface, pushing air ahead of it in a thin shell. It was developed to determine the effect of filling a hypothetical laser-fusion reactor chamber with a background gas to protect the chamber walls from target debris.

The usual strong-shock Hugoniot jump conditions for pressure p, density ρ, and flow velocity u are taken across the intereface at position R_s between the shocked and ambient air. The jump conditions at the contact surface inside R_s at position R_c ($R_c \simeq R_s$) are

$$u_d = u_s = \frac{2}{\gamma + 1} \dot{R}_s \text{ and } p_d = p_s = \frac{2}{\gamma + 1} \dot{R}_s^2 \rho_o \ . \qquad \text{(IV-9)}$$

Here the subscript s refers to the shocked gas, d refers to target debris, and o refers to ambient conditions. The total internal and kinetic energies are then related to the initial energy as

$$E_s = \int_0^{R_c} \left(\frac{1}{2} u_d^2 + \varepsilon_d\right) \rho_d 4\pi r^2 dr + \int_{R_c}^{R_s} \left(\frac{1}{2} u_s^2 + \varepsilon_s\right) \rho_s 4\pi r^2 dr \ , \qquad \text{(IV-10)}$$

where ε (ergs/g) is the specific internal energy given by

$$\varepsilon = \frac{1}{\gamma - 1} \frac{p}{\rho} \quad . \tag{IV-11}$$

The strong-shock Hugoniot relation for the densities across the ambient- to shocked-air interface is

$$\rho_s = \rho_o \left(\frac{\gamma + 1}{\gamma - 1}\right) \quad . \tag{IV-12}$$

The debris density is assumed uniform for $r \leq R_c$, therefore,

$$\rho_d = \frac{3M_T}{4\pi R_c^3} \simeq \frac{3M_T}{4\pi R_s^3} \quad . \tag{IV-13}$$

The thin-shell approximation assumes that within $\Delta r = R_s - R_c$, ρ_s is uniform and due to the mass of air originally in the sphere of radius R_s, so that

$$\rho_s = \frac{R_s}{3} \frac{\rho_o}{\Delta r} \quad . \tag{IV-14}$$

With these substitutions and the assumption of uniform pressures in the debris and thin shell,

$$E_s = \dot{R}_s^2 \left(C_1 + C_2 R_s^3\right) \quad , \tag{IV-15}$$

where

$$C_2 = \frac{8\pi}{3} \rho_o \left(\frac{2}{(\gamma + 1)^2} + \frac{1}{\gamma^2 - 1}\right) \text{ and } C_1 = \frac{2}{(\gamma + 1)^2} M_T \quad . \tag{IV-16}$$

Equation (IV-15) can be integrated analytically, in terms of elliptic integrals, or numerically to yield a radius-vs-time relation for comparison with the data.

If $M_T \to 0$ or $R_s \to \infty$, the first term in Eq. (IV-15) becomes negligible. In both cases, Eq. (IV-15) should converge to the Taylor-von Neumann-Sedov solution. However, a comparison of Eq. (II-7) with Eq. (IV-15) for $C_1 = 0$ shows that C_2 is a factor of 2 too large. The factor of 2 is mainly the result of assuming the interior pressure is equal to p_s instead of 0.5 p_s (see Appendix C) as was found in deriving Eq. (II-7) [Zel'dovich and Raizer (1966)]. There is also a small contribution to C_2 from the internal energy of the shell, which is assumed to be zero in deriving Eq. (II-7). The factor of 2 in C_2 decreases R_s by a factor of $2^{1/5}$ for large R_s. Therefore, a value of $C_2/2$ will be used for calculating R_s vs t.

We further justify a decreased C_2 by noting that at some time in the expansion, based on the assumptions leading to Eq. (IV-15), $\rho_s = \rho_d$, $p_s = p_d$, and therefore the shocked region is isothermal. Empirical evidence from nuclear explosions, which certainly include source debris and which are known to start as isothermal spheres, indicates that the resulting shocks are identical to Taylor-von Neumann-Sedov shocks at large R_s. Therefore, if the Freiwald/Axford approximation is to be consistent with Eq. (II-7) at late times, we must use $C_2/2$ in Eq. (IV-15).

Several points can be noted from the derivation and from Eqs. (IV-15) and (IV-16). The initial expansion velocity obtained by letting $R_s \to 0$ in Eq. (IV-15) is linear, with a velocity that depends only on the target mass and the energy E_s and not on ambient

gas density. The velocity is proportional to the square root of the energy. These two points are contradicted by the laser shock data. For our experimental conditions, Eq. (IV-15) yields values of the initial velocity only slightly less than free expansion velocities measured from arrival time of ions in vacuum at the charge collectors (see the end of this chapter). The calculated velocity is much greater than the initial transverse velocities measured in 1 and 50 torr atmospheres. Equation (IV-15) also yields an initial velocity approximately a factor of three higher than can be inferred from the data of Leonard and Mayer (1975) in 20-torr helium using 140-ng targets, assuming E_s = 15 J and γ = 1.67.

The previously defined radius of maximum deceleration, R_D, for the Freiwald/Axford solution can be found by setting $\dddot{R}_s = 0$. That is,

$$\dddot{R}_s = \dot{R}_s \frac{d}{dR_s}\left(\dot{R}_s \frac{dR_s}{dR_s}\right) = 0 \quad . \qquad \text{(IV-17)}$$

This implies a radius for maximum deceleration of

$$R_D = \left(\frac{C_1}{2C_2}\right)^{1/3} = \left(\frac{3M_T}{4\pi\rho_0}\right)^{1/3}\left(\frac{\gamma - 1}{6\gamma - 2}\right)^{1/3} \qquad \text{(IV-18)}$$

where Eq. (IV-16) has been used for C_1 and C_2. It can be seen from Eq. (IV-18) that the shock boundary goes through its maximum deceleration when the ratio of entrained air mass to target mass is $(\gamma - 1)/(6\gamma - 2)$ [or $2(\gamma - 1)/(6\gamma - 2)$ if one-half the value of Eq. (IV-16) is used for C_2]. This is a very small ratio of 1/26 (or

1/13) for $\gamma = 1.2$. The data presented in Chapt. II indicate a much larger ratio; namely, ~ 5 to 10.

Eq. (IV-15) was numerically integrated, assuming one-half the value of C_2 given by Eq. (IV-16), to obtain the curves in Fig. IV-2 for comparison with the E_s = 12.3-J, 1-torr data and the E_s = 2.5-J, 50-torr data. It was assumed that $M_T = 3.4$ μg and $\gamma = 1.2$. Equation (II-7) is plotted for the same values.

The curves generated by integrating Eq. (IV-15) begin with an initial velocity determined by C_1 in Eq. (IV-16), and they very slowly approach the self-similar curves of Eq. (II-7). From C_1, it can be seen that if $\gamma \to 1$, the initial velocity is simply given by $\dot{R}_s = \sqrt{2E_s/M_T}$. The measured radius-vs-time curves show a sudden break from the linear to self-similar behavior, as well as a much slower initial velocity. The comparison between data and the Freiwald/Axford theory, therefore, shows only slight similarities.

Application of Fuchs' Solution

Fuchs' solution is derived in Appendix C in order to clarify notation, and because the original Fuchs report (1947) was not widely circulated, not having been declassified until 1973.

From Eq. (IV-17) and the form of Eq. (C-24), the radius of maximum deceleration [i.e., the radius where $\dddot{R}_s(R_D) = 0$] can be seen to be independent of any of the factors in Eq. (C-24) that are not functions of R_s. This includes the energy, E_s, and γ. Equation (C-21) indicates that $\ell n\bar{R}$ is only the logarithmic average of the excess material and has little influence on $f(R_s)$, given by Eq. (C-23) for $R_s > R$. Therefore, the radius of maximum deceleration

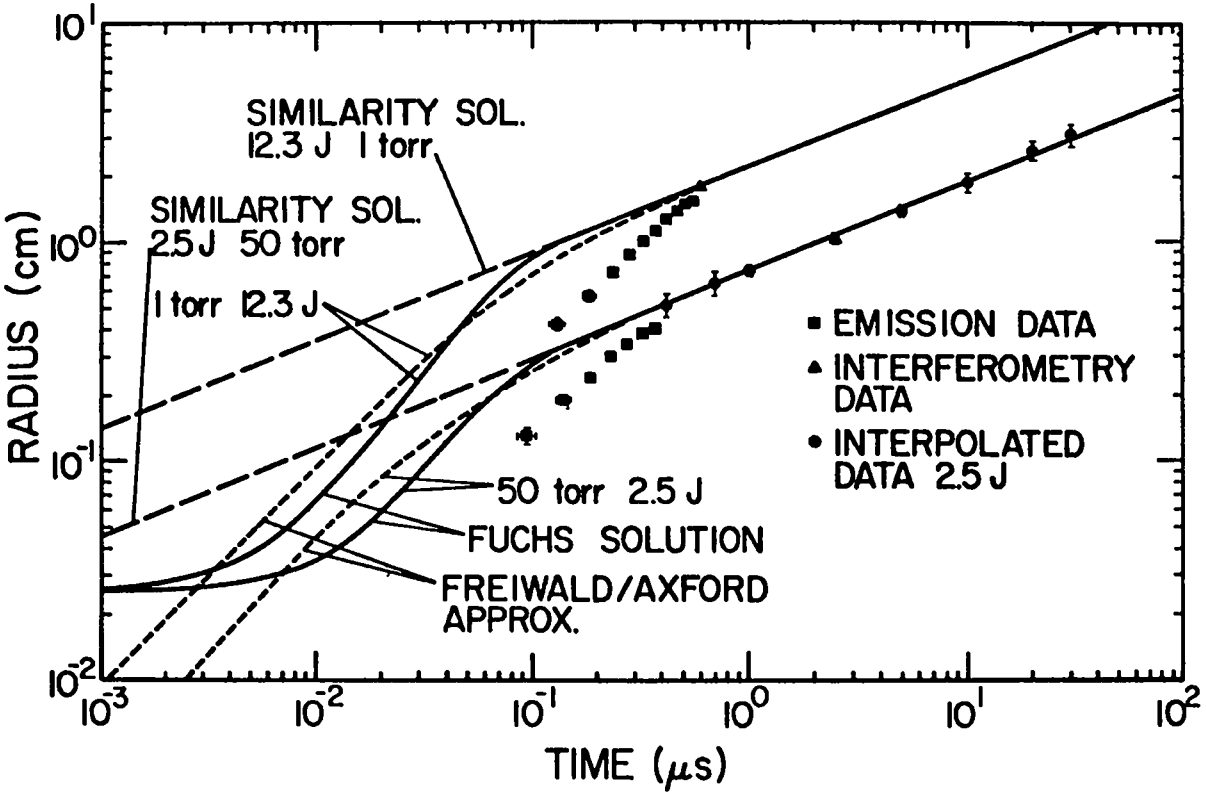

Fig. IV-2. Comparison of two approximate analytical solutions with data. Emission and interferometry data at 1 torr are for an E_L = 24.6 J experiment; emission and interferometry data at 50 torr are for an E_L = 27.6 J experiment. Interpolated 50-torr data assume E_L = 25 J.

depends only on R_0 in Eq. (C-18), the equal-mass radius. Solution of Eq. (C-25) with various initial conditions indicates that the maximum deceleration radius is $\sim R_0$. Because $\bar{R}$ is small, the exact initial distribution of the target mass has little effect on the initial velocity or on the point where the shock becomes self-similar. It is not important to know the exact mass distribution right after the energy release.

Numerical computations have been done by Whitaker and Horak (private communication) for massive sea-level nuclear detonations in the range of 100-kt TNT equivalent with several hundred tons of surrounding mass. To test Fuchs' approximation before applying it to the laser-generated shocks, the solution was compared with those computer calculations and found to be in fair agreement.

R_0 can be determined simply for the case where the density distribution is a step function, as it is for the targets. If $\rho(r)$ is constant and greater than ρ_0 for $R_1 > r > R_i$ where R_i is the inner radius of the shell, that is $R_1 > R_i \geq 0$, then Eq. (C-18) yields

$$R_0 = \left[\frac{3}{4\pi}\frac{M_T}{\rho_0} - (R_1^3 - R_i^3)\right]^{1/3} . \qquad \text{(IV-19)}$$

For the case of the laser targets, $M_T = 3.4\ \mu g$, $R_i = 0.0250$ cm, and $R_1 = 0.0254$ cm. For room-temperature air, 1-torr pressure corresponds to $\rho_0 = 1.57 \times 10^{-6}\ g/cm^3$, while $\rho_0 = 7.87 \times 10^{-5}$ for 50-torr pressure. Therefore, Eq. (IV-19) yields $R_0(1\ torr) = 0.802$ cm and $R_0(50\ torr) = 0.218$ cm.

Assuming a density step function of the form used to obtain Eq. (IV-19), Eq. (C-21) can be used to calculate $\bar{R}$:

$$\ell n\bar{R} = \frac{\left(r^3 \ell nr - \frac{r^3}{3}\right)\Big|_{R_i}^{R_1}}{R_1^3 - R_i^3} \quad . \tag{IV-20}$$

If $\ell n\bar{R}$ is taken literally, the given target parameters yield $\bar{R}$ = 0.02539. The significance of $\bar{R}$ is that it determines the approximate lower limit for which Eq. (C-25) is integrable.

To compare the data with Fuchs' solution, the values given above for R_o and $\bar{R}$ were substituted in Eq. (C-25). The value of the integrand was calculated at 5000 evenly spaced radii from 0.0 to 2.5 cm, and the function was numerically integrated to yield approximately 5000 different values of t, using Simpson's method. The lower limit of the integration was taken to be the lowest of the 5000 values of Z' for which the denominator of the integrand is not imaginary. This represents an error in t slightly greater than 1 ns. The value of E_s was 12.3 J for the 1-torr case and 2.5 J for the 50-torr case, corresponding to the 1-torr E_L = 24.6-J and 50-torr E_L = 27.6-J data of Fig. II-4. The values of E_s were again chosen using Eq. (II-7) fit to the interferometric data points. A strong-shock γ of 1.2 was assumed for both cases. The resulting curves are plotted in Fig. IV-2.

This figure shows that the expansion is approximately linear for a period of time. During this period, the calculated velocities are higher than the measured transverse velocities by a factor of 3. At a given radius during the linear expansion, Eq. (C-24) indicates the

value of E_s used in the solution should be correspondingly lower by a factor of nine to match the data, because $\dot{R}_s \propto \sqrt{E_s}$.

There is an inconsistency between the results of Fuchs' solution for low pressures and its assumptions. The initial velocity for a 50-torr 2.5-J calculation is about 2.7×10^6 cm/s. The solution assumes the target and shocked-air masses are in a thin shell traveling at this velocity. The kinetic energy of the target mass alone is 1.2 J or about 50% of E_s, contradicting the assumption of negligible kinetic energy.

The ratio of energy to source mass for a typical nuclear explosion is close to that of these experiments. Fuchs' solution showed good agreement in the nuclear case because ρ_0 was the sea-level value. The initial expansion is slower for sea-level values of ρ_0 than it is for ρ_0 at 50-torr pressure and room temperature. Accordingly, the kinetic energy in the case of the nuclear detonation is less than 0.1%.

Another difference between the experiment and Fuchs' solution is the energy release distribution. In the experiment, it was asymmetrically distributed throughout the highly extended mass. The solution assumes a point release at the center of a spherical mass distribution.

Fuchs' solution shows one qualitative feature seen in the data. The decrease in velocity is abrupt when the shock reaches the radius where self-similar expansion begins. The Freiwald/Axford solution shows a more gradual approach.

It is interesting to note with respect to Eq. (II-9) that, if the initial velocity is proportional to $\sqrt{E_s}$ (as it is in the Fuchs and Freiwald/Axford approximations), then R_D is independent of E_s. R_D is then proportional to the ratio of target mass to entrained air mass. We note that the measured initial transverse velocity is independent of E_s, in which case R_D is determined by the ratio of E_s to entrained air mass. That is, by Eq. (II-9),

$$\frac{E_s}{M_A} = \frac{E_s}{\rho_o \frac{4}{3} \pi R_D^3} = \frac{3}{4\pi} \xi V_o^2 = \text{constant} \quad , \qquad \text{(IV-21)}$$

where M_A is the entrained air mass at radius R_D.

Initially, the energy is deposited in the target material This target energy is transferred to the surrounding air as the air becomes entrained. After the energy to entrained-air-mass ratio reaches approximately the value given by Eq. (IV-21), the shock expands self-similarly as a Taylor-von Neumann-Sedov shock wave.

Variable-Energy Blast Wave Interpretation of the Early Expansion

In this section, we propose an alternative model of the early expansion in which the shock wave is regarded as a variable-energy blast wave. It will be assumed that the laser energy is uniformly deposited in the target material, which then expands as an isentropic gas supplying energy to a surrounding shock wave. The shock expands as a blast wave with a steadily increasing energy.

Although the description does not provide explicit radius-vs-time solutions or explicit density profiles at the shock front, it

is useful for interpreting numerical calculations. The model also explains several features of the data.

This description is somewhat of a limiting case because the energy is asymmetrically deposited in the target. The rate at which the target material supplies energy to the transverse expansion is also determined by the rate of redistribution of the energy over the shock interior. It can be expected that the transverse expansion is slower than that which would occur for a symmetric energy distribution.

As mentioned in the introduction, variable-energy blast waves expand such that $R_s \propto t^{\alpha}$ when energy is supplied to the shock front at the rate $E_s = Wt^{\beta}$. The relationship between the constants α and β is $\alpha = (\beta + 2)/5$. In the following argument, we will assume β and therefore α are only approximately constant with a slight time dependence, but the relation between α and β still holds.

The rate at which energy is supplied to the transverse shock front is apparently independent of the total energy deposited by the laser because $\alpha \sim 1$ within experimental error regardless of the value of E_s determined during the later expansion when $\alpha = 2/5$. The situation might be viewed as follows. The target mass acts as a reservoir for the laser energy; however, the rate at which the energy is supplied to the transverse shock front is unaffected by how full the reservoir is. For example, a larger deposit of energy might result in larger and/or hotter longitudinal bulges but the transfer of energy from the bulges to the transverse expansion is nearly constant regardless of the condition of the bulges.

The value of β may actually have some energy dependence (and time dependence as well). However, β is determined by measuring α and from the relation $\alpha = (2 + \beta)/5$. From the α-β relation, $\Delta\beta \simeq 5\Delta\alpha$, so a value of $\alpha = 0.95 \pm 0.06$ translates to a value of $\beta = 2.75 \pm 0.3$ and the value of β could vary with energy as much as 20 to 25% and still not show a measurable variation in α. The value of β may also be time dependent for this experiment within the experimental error.

There is some empirical evidence to support the variable-energy blast wave model. In Fig. III-6, there is a suggestion of a second density increase behind the shock front. The surface between the secondary and main density front is at 0.9 of R_s. The secondary density increase suggests an accumulation of shocked target material behind the main shock front and is consistent with the assumption that the target material is expanding and supplying energy to the front. Another observation is that the luminous plasma slows and falls behind the shock wave just before the shock begins to expand as a Taylor-von Neumann-Sedov blast wave. This fact suggests that the target plasma is no longer supplying energy to the shock front and, therefore, $\alpha \rightarrow 2/5$.

Figures II-2 and -3 show interesting features with respect to a variable-energy blast wave assumption. The target mass initially must go through a period of acceleration against the lower density surrounding air. This is particularly true for target mass directly in the laser beam. As long as the denser mass is accelerated against the ambient air, Rayleigh-Taylor instabilities would be expected to form and grow. The possible remnants of such instabilities are

indicated by the lobes on the left of the image in Fig. II-3 and by the overall mottling of the shock surface in Fig. II-2.

The general variable-energy blast-wave solutions have been studied by Freeman (1968). The special case of the energy input proportional to t^3 was examined earlier by Taylor (1946) with regard to the air wave surrounding a constantly expanding sphere. Avedisova (1972) and Weaver et al (1977) considered the shocking of a circumstellar medium by a strong stellar wind where E_s is supplied by the stellar wind and is proportional to t. Director (1975) purposely input laser energy to targets at a rate proportional to t for comparison with the variable-energy blast solution and Dabora (1972) considered a variable-energy interpretation of Hall's (1969) data that showed a very slight variation from the instantaneous point explosion expansion rate.

The variable-energy self-similar solution to the fluid equations is obtained as follows. The fluid equations of continuity, motion, and energy for spherical, adiabatic, inviscid flow are

$$\frac{\partial \rho}{\partial t} + u \frac{\partial \rho}{\partial r} + \rho \frac{\partial u}{\partial r} + 2 \frac{\rho u}{r} = 0 \quad , \tag{IV-22}$$

$$\frac{\partial u}{\partial t} + u \frac{\partial u}{\partial r} + \frac{1}{\rho} \frac{\partial p}{\partial r} = 0 \quad , \tag{IV-23}$$

and

$$\frac{\partial (p/\rho^{\gamma})}{\partial t} + u \frac{\partial (p/\rho^{\gamma})}{\partial r} = 0 \quad , \tag{IV-24}$$

where u is the flow velocity, p the pressure, ρ the density, and r the Eulerian radial coordinate. If the motion is self-similar, these equations reduce to separable ordinary differential equations (ODE) with the condition that the radius of the shock is given by $R_s = At^{\alpha}$, where A is a dimensional constant with length, L, and time, T, dimension $[A] = LT^{-\alpha}$. The reduction to ODEs proceeds as follows [e.g., Zel'dovich and Raizer (1967)]. Dimensionless functions of the similarity variable $\zeta = r/R_s$ can be defined with respect to the dependent variables $p(r,t)$, $\rho(r,t)$, and $u(r,t)$ by $p(r,t) = \rho_0 \dot{R}_s^2 \Pi(\zeta)$, $\rho = \rho_0 g(\zeta)$, and $u(r,t) = \dot{R}_s v(\zeta)$. For the conditions of this experiment, ρ_0 is constant. With the condition $R_s \propto t^{\alpha}$, and substitution of the newly defined dimensionless variables Π, g, and v, the PDEs convert to

$$g'(v - \zeta)/g + v' + 2v/\zeta = 0 \quad , \qquad \text{(IV-25)}$$

$$v(\alpha - 1)/\alpha + v'(v - \zeta) + \Pi'/g = 0 \quad , \qquad \text{(IV-26)}$$

and

$$2\Pi(\alpha - 1)/\alpha + \Pi'(v - \zeta) - \gamma\Pi g'(v - \zeta)/g = 0 \quad , \qquad \text{(IV-27)}$$

where the prime indicates a derivative with respect to ζ.

The boundary conditions at $\zeta = 1$ are given by the strong-shock Hugoniot relations Eqs. (III-21) and (-22) and $u = 2\dot{R}_s/(\gamma + 1)$ and are found to be $\Pi(1) = u(1) = 5/6$ and $g(1) = 6$ for $\gamma = 1.4$. Equations (IV-25) through (IV-27) have been numerically integrated and results for the density are plotted in Fig. IV-3 for several values

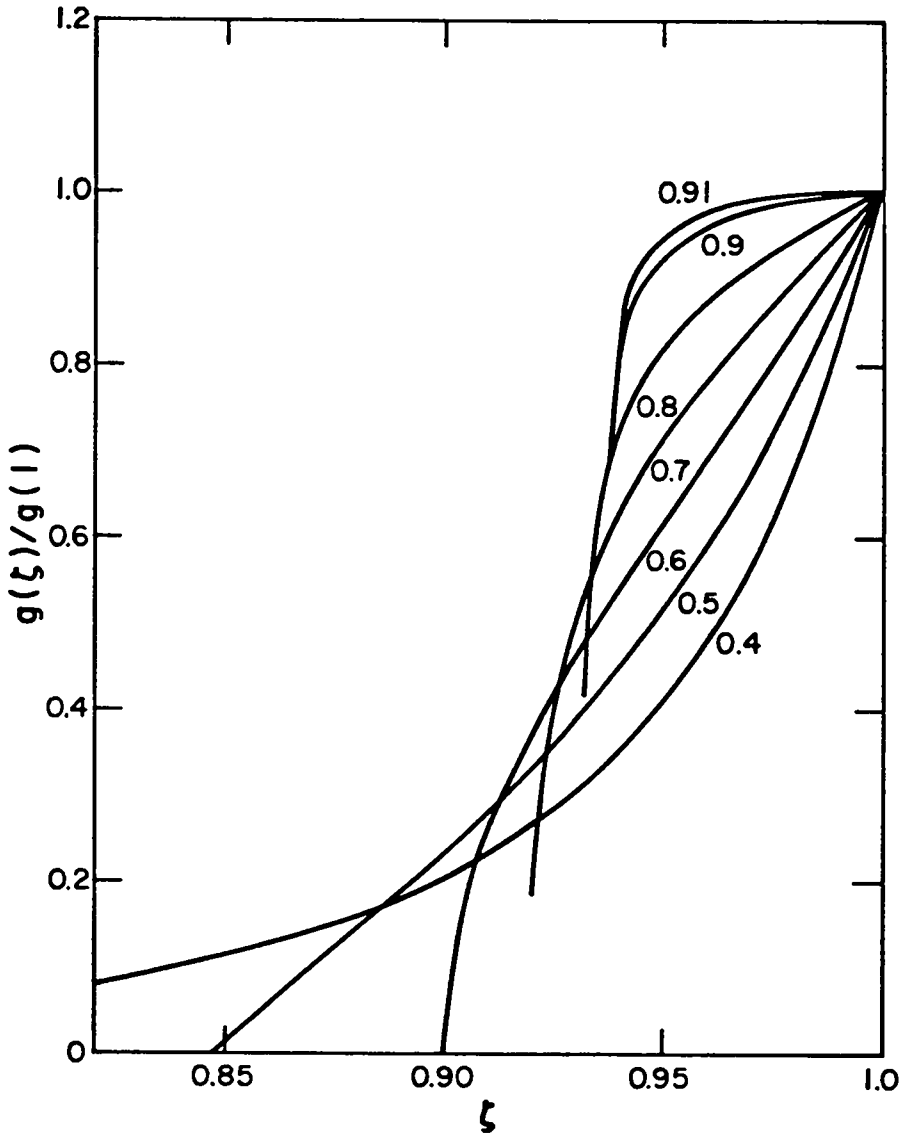

Fig. IV-3. Normalized self-similar variable-energy density curves for α - 0.4 to 0.91.

of α. It can be seen that for $\alpha > 0.4$, the density abruptly decreases. The apparent intersection of the curves with the ζ axis increases with α. However, for α = 3/5 to 1 (β = 1 to 3), the intersection only varies from 0.85 to 0.94. A shell of swept-up air of uniform density with a maximum $\rho = \rho_0(\gamma + 1)/(\gamma - 1)$ and $\gamma = 1.4$ would decrease to zero at $\zeta = 0.941$. Figure IV-4 gives the curves for the normalized density velocity and pressure functions for $\alpha = 0.9$. The pressure curve is finite and nearly uniform. It would therefore be expected from $T \propto p/\rho$ that a spike would occur in the temperature profile where the density decreases behind the front.

The constants A and α are partially determined from the dimensionality of the constants describing the problem; $[\rho_0] = ML^{-3}$ and $[W] = ML^2T^{-(2+\beta)}$, where M, L, and T indicate the dimensions of mass, length, and time, respectively. α is a pure number and $[A] = LT^{-\alpha}$. Therefore, $A = (W/\rho_0)^{1/5}F$ so that

$$R_s = F(W/\rho_0)^{1/5}t^{\alpha} \quad , \tag{IV-28}$$

where $\alpha = (2 + \beta)/5$. F is a numerical constant that in principle can be determined from the energy integral

$$E_s = 4\pi \int_0^{R_s} [\rho u^2/2 + p/(\gamma - 1)]r^2 dr \tag{IV-29}$$

$$= \rho_0 R_s^3 \dot{R}_s^2 4\pi \int_0^1 [2g(\zeta)v^2(\zeta)/(\gamma + 1)^2 + 2\pi(\zeta)/(\gamma - 1)(\gamma + 1)]\zeta^2 d\zeta$$

$$= \rho_0 R_s^3 \dot{R}_s^2 I \quad , \tag{IV-30}$$

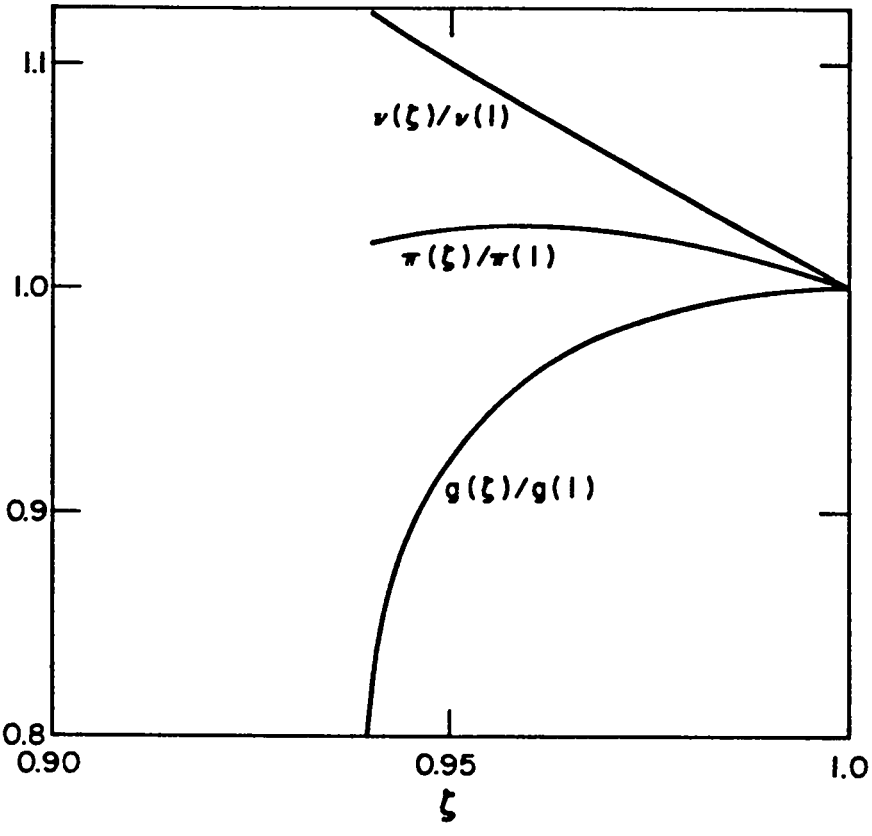

Fig IV-4. Normalized velocity, pressure, and density curves for variable-density self-similar solution with $\alpha = 0.9$.

and the relations $\dot{R}_s = \alpha R_s/t$ and $E_s = Wt^{\beta}$ to be

$$F = (\alpha^2/I)^{1/5} \quad . \tag{IV-31}$$

In practice, Eq. (IV-30) cannot easily be used to calculate F because there is a difficulty in obtaining solutions for g, Π, and v for $\zeta < 0.9$. Approximate forms for g, Π, and v on the interior of the shock will be determined by considering the heated target mass as an isentropic gas. This will provide insight into the problem; however, it will not provide functions suitable for integration in Eq. (IV-30). Instead, an approximate value of A can be determined empirically from the data for this particular experiment. In Chapt. V, a finite-difference scheme is employed to investigate ρ, p, and u over the entire range $0 \leq \zeta \leq 1$.

To approximate the interior of the shock, we will assume that the target is uniformly heated and soon afterwards expands self-similarly as an isentropic gas in vacuum. The presence of the surrounding air will be ignored for the moment. The assumption of self-similar expansion despite the initial non-self-similar density distribution is probably very good as long as it is assumed the target is evenly heated. The free molecular flow and numerical fluid calculations of Molmud (1960) indicate that an initially uniform gas allowed to expand spherically in vacuum quickly relaxes to an isentropic self-similar expansion. Molmud's results indicate that the relaxation occurs within the time the radius of the gas volume doubles. If the surrounding air is to be a negligible perturbation to the formation of a freely expanding self-similar

isentropic gas from the target material, we must have $32\pi\rho_0 R_T^3/3 \ll M_T$ where R_T is the target radius. For 50-torr data, $32\pi\rho_0 R_T^3/3 = 0.01\ M_T$.

The self-similar solution for isentropic gas expansion is outlined by Zel'dovich and Raizer (1967). The flow velocity, density, and pressure are given by

$$u = \dot{R}_I \frac{r}{R_I} \quad , \tag{IV-32}$$

$$\rho = \rho_c \left(1 - \frac{r^2}{R_I^2}\right)^{1/(\gamma-1)} , \tag{IV-33}$$

and

$$p = A\rho^{\gamma} \quad . \tag{IV-34}$$

R_I ($\dot{R}_I$) is the radius (velocity) of the boundary of the isentropic gas in vacuum. A is the isentropic constant and ρ_c is the central density calculated from the volume integral of ρ as

$$\rho_c = \frac{M_T}{4\pi R_I^3} \frac{1}{\int_0^1 (1 - x^2)^{1/(\gamma-1)} x^2 dx} \quad , \tag{IV-35}$$

where $x = r/R_I$ is the normalized radius. Substituting Eqs. (IV-32) through (-34) into the equation of motion [Eq. (IV-23)] yields

$$A\rho_c^{\gamma-1}/(\gamma - 1) = R_I \ddot{R}_I/2\gamma \quad . \tag{IV-36}$$

We solve the problem numerically as follows. Substituting Eqs. (IV-32) to (-34) into the energy integral, Eq. (IV-29), and using

Eqs. (IV-35) and (-36) to eliminate ρ_c and A, we obtain

$$E_I = \frac{M_T \dot{R}_I^2}{2 \int_0^1 (1 - x^2)^{1/(\gamma-1)} x^2 dx} \left[\int_0^1 (1 - x^2)^{1/(\gamma-1)} x^4 dx + \frac{R_I \ddot{R}_I}{\gamma \dot{R}_I^2} \int_0^1 (1 - x^2)^{\gamma/(\gamma-1)} x^2 dx \right] \qquad \text{(IV-37)}$$

where E_I is the energy of the isentropic gas. Assuming initial values of $R_I = 0.025$ cm and $\dot{R}_I = 0$, a value of R_I is calculated from Eq. (IV-37) and used to obtain new values of R_I and $\dot{R}_I$ assuming a time increment, Δt, chosen small enough so that R_I changes by a factor less than 0.001.

The last term in Eq. (IV-37), resulting from the internal energy, goes to zero at large R_I. Therefore, $\dot{R}_I(t \to \infty)$ becomes a constant $U_1 = c(\gamma) \sqrt{2E_I/M_T}$ where $c(\gamma) = 2.23$ for $\gamma = 6/5$, $c(\gamma) = 2.08$ for $\gamma = 5/4$ and $c(\gamma) = 1.64$ for $\gamma = 5/3$.

If we assume the laser-target energy coupling is the same in vacuum as in 1-torr air (~ 45%), then for $E_L = 21$ J, $E_I = 9.5$ J, and U_1 ($\gamma = 5/3$) $= 1.2 \times 10^7$ cm/s or $U_1(\gamma = 5/4) = 1.5 \times 10^7$ cm/s. Figure IV-5 shows the output from an ion detector 56 cm away from and transverse to the Nd:laser for a 21-J shot. The thermal ions begin to arrive at ~ 5 μs corresponding to $U_1 = 1.1 \times 10^7$ cm/s, in agreement with the $\gamma = 5/3$ value.

The two bumps at ~ 10 μs and ~ 22 μs are probably due to hydrogen and carbon respectively, indicating that the target gas is atomic and not molecular so $\gamma = 5/3$ is correct. The separate bumps

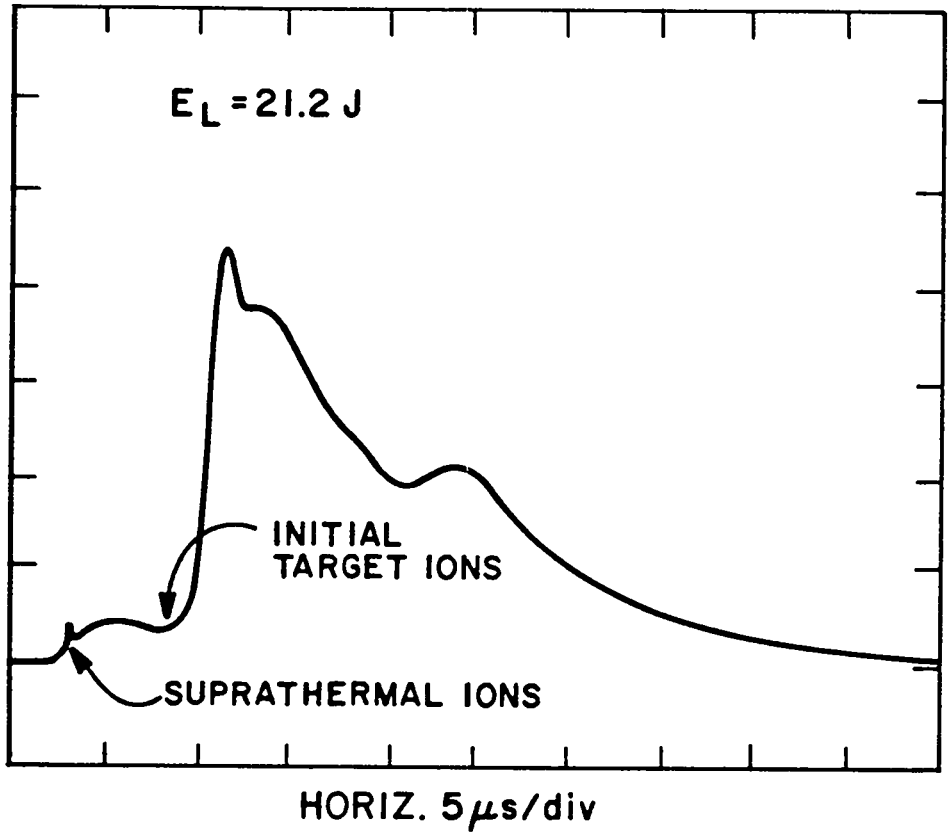

Fig. IV-5. Oscilloscope trace from an ion cup 56 cm from target and transverse to Nd:glass laser beam.

also show that the expansion is only approximately a single ideal isentropic gas expansion.

Equation (IV-37) can be used to calculate the radial energy density versus the normalized radius once $R_I(t)$, $\dot{R}_I(t)$ and $\ddot{R}_I(t)$ are calculated. Figure IV-6 is a plot of dE_I/dx vs x for $t = 10^{-12}$ s and t = 36 ns. The energy distribution changes only slightly after t = 36 ns. For the initial values indicated in the figure, R_I (36 ns) = 0.5 cm.

The 36-ns curve of Fig. IV-6 represents the distribution of energy available in the target material to supply a surrounding shock front in air at some value of $x < 1$.

For example, suppose that as the target material spreads and forms a self-similar isentropic gas, it also pushes the surrounding air into a shock front with outer radius $R_s(t)$ and velocity $\dot{R}_s(t)$. The disturbance of the isentropic gas near the boundary has little effect on the interior because signals cannot propagate from the boundary to the center of an isentropically expanding gas. The target material collides into the rear of the shock front supplying the front with energy. The curves in Fig. IV-3 indicate that for values of $\beta \gtrsim 1$ the rear of the shock front is always at $\sim 0.9\ R_s$ and therefore has a velocity of $\sim \dot{R}_s$.

Suppose at t = 37 ns, $R_s = 0.8\ R_I$ and, for the moment, $\dot{R}_s$ is constant. The rear of the shock front is at $\sim 0.7\ R_I$. Figure IV-6 shows that the energy density at $r = 0.7\ R_I$ is increasing approximately linearly towards the center of the shock. The relative velocity of the isentropic gas and the shock front is momentarily

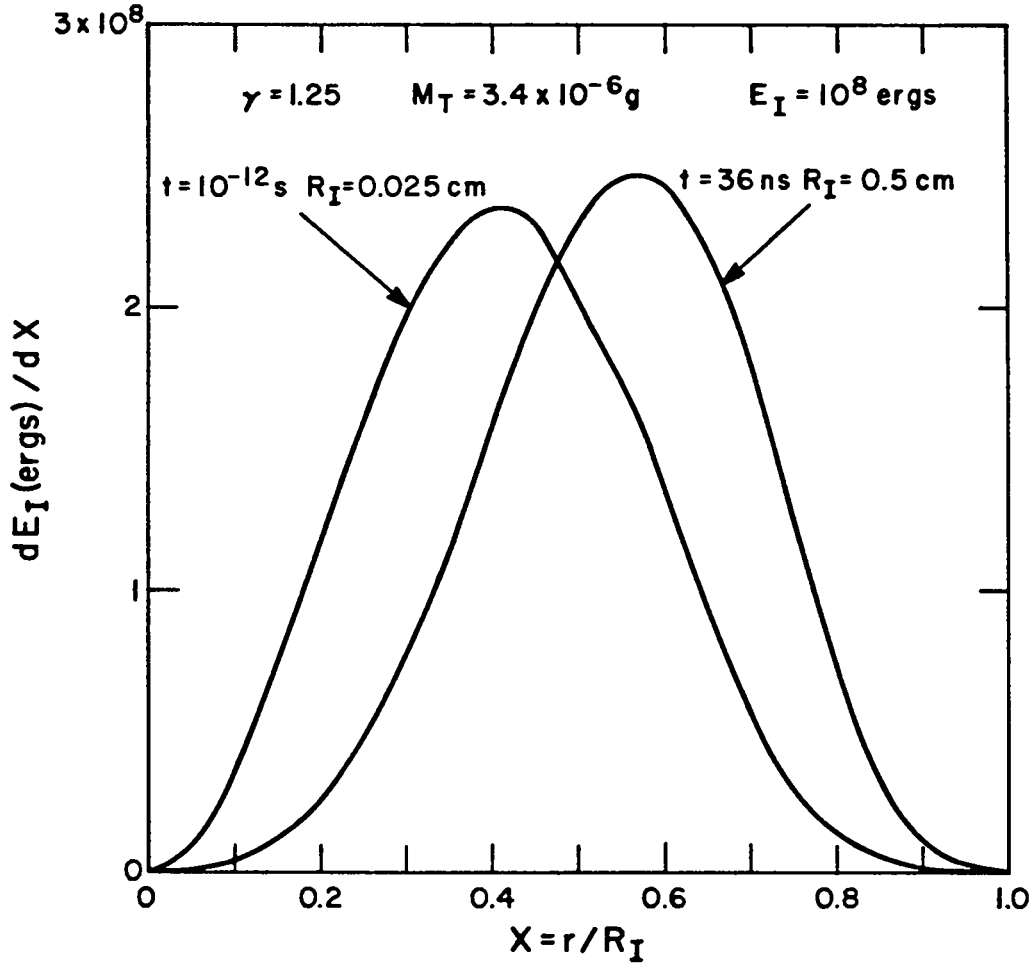

Fig. IV-6. Radial energy distribution in an ideal gas isentropically expanding into vacuum.

constant; therefore, the energy is being supplied linearly with time or $\beta = 1$. However, if $\beta = 1$, $\alpha = 3/5$, and the shock must decelerate. This in turn increases β, and it can be expected that as long as the energy supply rate to the shock does not change abruptly, β and α will approximately obey the relation $\alpha = (\beta + 2)/5$ and reach an equilibrium condition.

The situation is somewhat more complicated because the flow velocity u given by Eq. (IV-32) was used to calculate the curves in Fig. IV-6. Actually the kinetic energy supplied from the isentropic gas to the shock front is determined by using $u-\dot{R}_s$ for the velocity instead of just u. There is also the further modification of the supply rate to the transverse shock due to nonuniformities in energy distribution resulting in asymmetries in the shock geometry.

Once α is taken as ~ 1, the value of A in $R_s = At$ is empirically determined by the measured constant velocity of the early expansion, V_o.

Both the normalized velocity and pressure of the variable-energy blast wave increase behind the front instead of decreasing as in the case of the instantaneous $\alpha = 0.4$ solution. This reflects the piston-like nature of the problem. Material behind the front is traveling faster and decelerates into the front causing the increase in pressure that drives the front onward.

Summary

In Chapter IV we have examined the early expansion of the target and formation of the Taylor-von Neumann-Sedov shock wave. Calculations indicated that electron heat transport and differences between

the target EOS and the air EOS were not an important influence on the expansion rate. The effects of the source mass were then considered.

Two analytical approximations that included source mass were compared with the data. The approximations were spherical, and therefore it was difficult to directly compare the predicted expansion with the measured transverse expansion of the aspherically expanding targets. Both approximations exhibited features that were found in the data.

A model was presented that describes the expanding target as an isentropically expanding gas supplying energy to a surrounding shock wave. The model will be used to interpret numerical calculations in the following chapter.

CHAPTER V

NUMERICAL MODELING

In order to obtain better theoretical estimates of quantities such as the peak density and central electron density for comparison with the data, a detailed hydrodynamics/radiation transport code was employed to numerically model the experiment. The code results also provided a comparison with the approximate analytical models in Chapter IV.

Description of the Code

Development of a numerical method was not the aim of this thesis, and many fluids codes exist which only require modification for application to this problem. The code RADFLO developed by John Zinn (1973) was selected. It has successfully modeled the similar problem of a shock wave generated by a nuclear explosion in air. The code includes hydrodynamics and a spherical two-stream multi-group radiation transport scheme. RADFLO is a one-dimensional code and therefore lacks the ability to strictly model the laser-energy deposition and early target expansion. Laser effects codes such as LASNEX are suited to the early phase [e.g., Edwards et al. (1973)], but may not do as well as RADFLO during the period of interest when the detailed properties of air are important. The laser effects codes are also substantially more complicated, and separation of physical and numerical phenomena becomes more difficult.

RADFLO contains empirical equation-of-state data represented in Fig. III-2 and also an empirically based air opacity table for radiation transport.

Hydrodynamics

The code uses a standard explicit Lagrangian finite-difference scheme for hydrodynamics calculations. A form of von Neumann-Richtmyer (1950) artificial viscous pressure is used to prevent collapse of the mesh cells at the shock front.

The cell pressure is interpolated from the EOS tables using the cell's specific internal energy and density. The time step is the minimum of the time step determined from the Courant condition and the time step determined from the maximum permissible fractional energy change per cell due to transport. At each step, the cell-boundary acceleration, change in cell size, specific internal energy, cell-boundary velocity and position are computed. Finally, a new cell volume and density are calculated. The procedure is then repeated.

Radiation Transport

The radiation transport calculation is carried out over a maximum of 43 frequency groups covering the region from 0.1 eV to 40.4 keV. The higher frequency groups are dropped from the calculation as they become unimportant. Four groups cover the visible from 312.2 to 678.6 nm.

The transport algorithm has been described in detail by Zinn. The first step in a calculation for each frequency group traces a

ray radially inward from the mesh boundary to an optical depth of 1. The radius at this point defines a "principal radiating source". It is assumed that a ray originating from the direction of the source has one value of intensity, I_a, while a ray originating from outside the source has a lesser value, I_b. The inward flux F^- and the outward flux F^+ at any boundary are related to the intensities by

$$F_\nu^{\pm} = \pm 2\pi \int I_\nu(\theta) \sin\theta\cos\theta d\theta \quad , \qquad \text{(V-1)}$$

where the integration limits are 0 to $\pi/2$ ($\pi/2$ to π) for F^+ (F^-). The intensity variation through a cell from point P1 to point P2, a distance ΔS apart, is calculated from

$$I_\nu(P_2) = I_\nu(P_1)e^{-\mu'\Delta S} + B_\nu(1 - e^{-\mu'\Delta S}) \quad , \qquad \text{(V-2)}$$

where μ' is the absorption coefficient at frequency ν, corrected for stimulated emission, and B_ν is the Planck function. It is then possible to derive six equations relating the four flux quantities of a cell, $F_1^{\pm}$ and $F_2^{\pm}$ (the outward and inward fluxes at the inner surface, 1, and outer surface, 2, of a cell) to the four intensities $I_{a1,2}$ and $I_{b1,2}$. The intensities are eliminated and the set of equations is closed by the continuity conditions across the boundaries (i.e., for cell i and i + 1, $F^+_{i,2} = F^+_{i+1,1}$, etc). The diffusion approximation ($F_\nu = -4/3\pi\nabla B_\nu/\mu'$) is used for the special case of two adjacent optically thick ($\mu'\Delta R \geq 2$) cells.

Once the fluxes are known, the change in the ith cell's energy due to radiation transport in a time step of length Δt is calculated

from

$$(\Delta E_r)_i = -\Delta t(\nabla \cdot F)_i$$
$$= \Delta t\{-4\pi \sum_{\nu} [R_1^2(F^+_{1,\nu} - F^-_{1,\nu}) - R_2^2(F^+_{2,\nu} - F^-_{2,\nu})]\}_i \quad \text{(V-3)}$$

where R_2 (R_1) is the outer (inner) cell boundary.

Electron Heat Transport

Electron heat transport was added to the code in order to verify numerically the calculation in Chapter IV which shows that electron heat transport is negligible.

The use of Eq. (V-3) for the calculation of $(\Delta E_r)_i$ due to radiation makes the inclusion of electron heat transport possible by a simple addition. That is, the total energy change in a cell $(\Delta E)_i$ is $(\Delta E_r)_i + (\Delta E_e)_i$, where

$$(\Delta E_e)_i = -\Delta t(\nabla \cdot F_e)_i = -4\pi(F_{e2}R_2^2 - F_{e1}R_1^2)_i \quad . \quad \text{(V-4)}$$

The quantity F_{e2} (F_{e1}) is the total flux due to electron transport passing through the outer (inner) cell boundary and is defined to be positive if outward and negative if inward with respect to the mesh center. The value of F_e is taken to be

$$\frac{1}{F_e} = \frac{1}{F_s} + \frac{1}{F_L} \quad , \quad \text{(V-5)}$$

where F_L is given by Eq. (IV-5) and F_s by Eq. (IV-3). The temperature dependence of the finite-difference equivalent of F_s between cell i and cell i+1 is

$$F_s \propto T_e^{5/2} \nabla T_e = \frac{2}{7} \nabla(T_e^{7/2}) \simeq \frac{2}{7} \frac{T_{i+1}^{7/2} - T_i^{7/2}}{\Delta R} \qquad \text{(V-6)}$$

where ΔR is the distance between the center points of the cells. The constant from Eq. (IV-3) is taken to be the average of the constant calculated for cell i and cell i+1. T_e in Eq. (IV-5) is taken to be $(T_{i+1} + T_i)/2$, and n_e is similarly averaged.

The value of n_e for cells with $T_e \geq 11000$ K is calculated assuming total dissociation and using $p = (n_e + n_p)k_B T$, where n_p is the heavy particle density. Below 11000 K, the values of n_e for each cell are determined from approximate analytic fits to ionization curves for air.

Modeling Results

Uniform ε

In the first set of modeling experiments, the shock wave energy, E_s, was distributed in the target so that the initial specific internal energy, ε (energy per unit mass), was constant.

The central cell had a radius of 2.5×10^{-2} cm and 50 torr (1 torr) density of 0.787×10^{-4} g/cm^3 (1.57×10^{-6} g/cm^3). The 4-μm target shell was divided into 43 cells with outer radii of 2.50012×10^{-2} cm, 2.50025×10^{-2} cm, 2.5005×10^{-2} cm, 2.501×10^{-2}cm, 2.502×10^{-2} cm, 2.503×10^{-2} cm . . . 2.54×10^{-2} cm and a density of 1.18 g/cm^3. The 75 ambient air cells were then spaced

at 0.03-cm intervals resulting in a 119-cell mesh with an outer boundary of 2.29 cm.

To start the problem, an ambient specific internal energy of 2.15×10^9 ergs/g, from the EOS tables for T ~ 300 K, was supplied to all the cells. A specific internal energy value of $\varepsilon = E_S/M_T$ was then added to each of the cells in the shell as well as the central cell, where E_S is the energy deposited by the laser and M_T is the target mass.

The numerical results for central electron density and peak gas density at times later than 1-μs for shocks in 50-torr air were insensitive to the spatial distribution of the initial energy. Figs. V-1a,b are plots of these values for the case of uniform ε (E_S = 2.5 J), together with a corresponding set of interferometry data from Figs. III-5a and b. The irregularities in the peak gas density curve are due to numerical noise resulting from the mesh coarseness. The numerically calculated central electron density curve in Fig. III-5b also has a finite width due to noise. The computed electron spatial distribution in the center of the shock shows numerical oscillations about an essentially constant value. The width of the curve represents the maximum excursion.

Plots of the same quantities for the energy distribution described in the next section were similar. A 50-torr calculation was also done with identical energy distribution but with a three-times-finer mesh. Again the results were nearly identical for $t \gtrsim 1$ μs. The interferometry data points for the peak density fall slightly below the numerical calculation for $t \lesssim 2.5$ μs. This may be due to error resulting from the Abel inversion. Agreement between data and

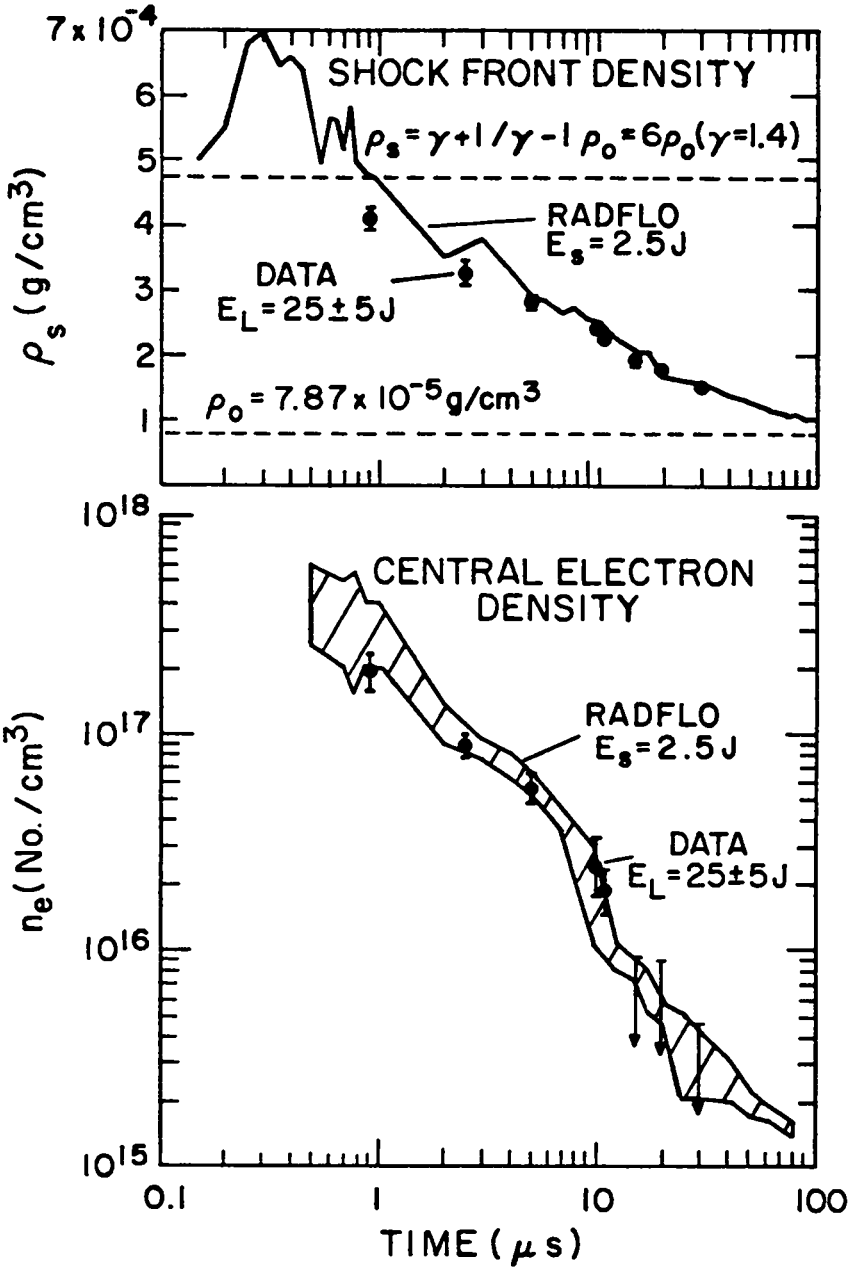

Fig. V-1. Comparisons of numerically calculated and measured peak gas densities (a), and central electron number densities (b).

model results is quite good for the remainder of the peak density curve and over the entire electron density plot.

Figure V-2 is an R_s vs t plot for simulations with energy inputs of 2.5 and 12.1 J and respective pressures of 50 and 1 torr. The experimental data of Fig. IV-2 are plotted for comparison. The curves labeled "Unif. ε" are the results of the uniform initial ε distribution described here. The curves labeled "Cent. ε" are described in the following section.

The computer simulations of the 1-torr shocks begin to show the $\alpha = 2/5$ (where $R_s \propto t^{\alpha}$) expansion at $\sim$ 500 ns and the 50-torr shocks at $\sim$ 300 ns. At earlier times, the value of α is larger. It is about 0.7 for the 1-torr data at about 10 ns. The transition to $\alpha = 2/5$ is gradual, but the radius at which it occurs seems to agree with the data. In the 1-torr and 50-torr simulations, the radius at which the shock breaks away from the emission profile is in good agreement with the data, as is the computed shock radius for $t > 400$ ns.

According to the discussion at the end of Chapt. IV, the density profile should show a minimum value at $\zeta = r/R_s \simeq 0.9$ whenever $0.4 \lesssim \alpha \lesssim 1$. Figures V-3 through V-6 are plots of computed radial profiles of density, pressure, velocity, and temperature, respectively, for a variety of times during the early expansion when $\alpha > 0.4$ for a shock in 1-torr air. The density does show a minimum at $\zeta \sim 0.9$. The arrows mark the contact surface between the target mass and shocked air mass.

The central density decreases approximately as $1/t^3$, as predicted by the isentropic gas calculation at the end of Chapter IV. The

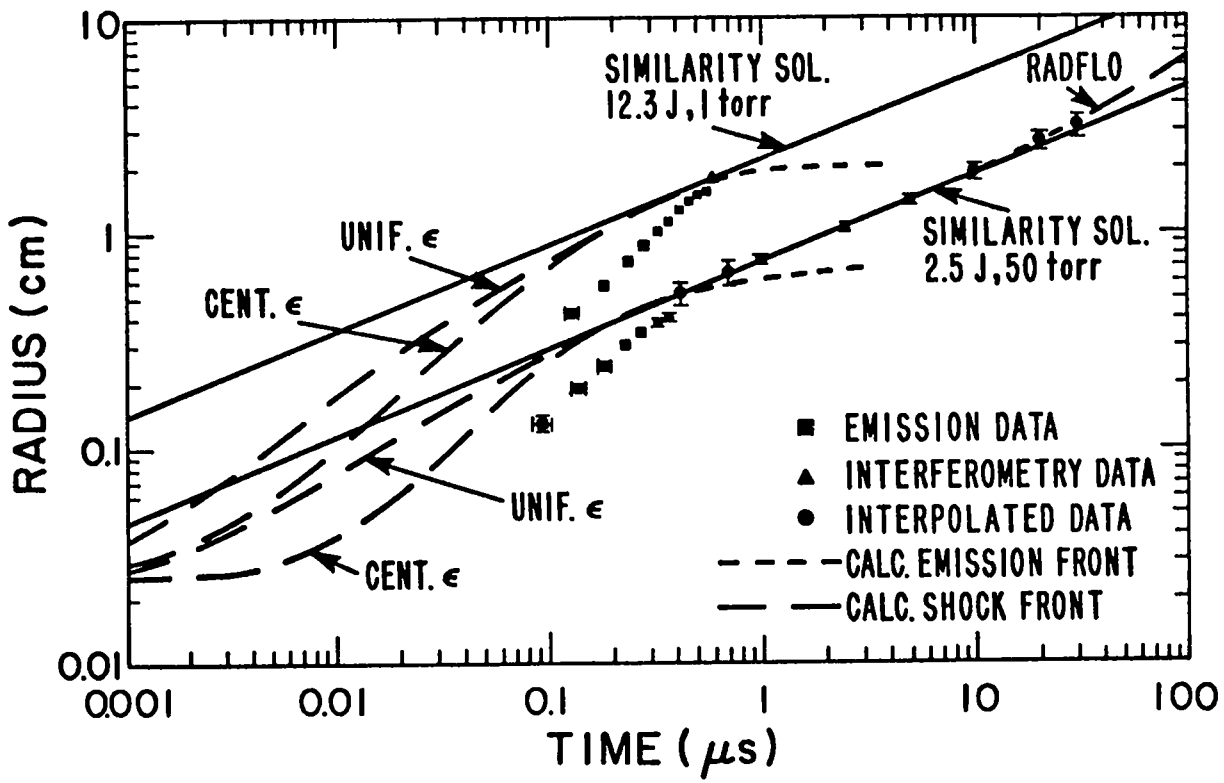

Fig. V-2. Comparison of numerically calculated and measured radii vs time. UNIF. ε refers to a numerical model with E_s initially evenly distributed through the target mass. CENT. ε refers to a model with E_s initially within the target shell. Data are the same as in Fig. IV-2.

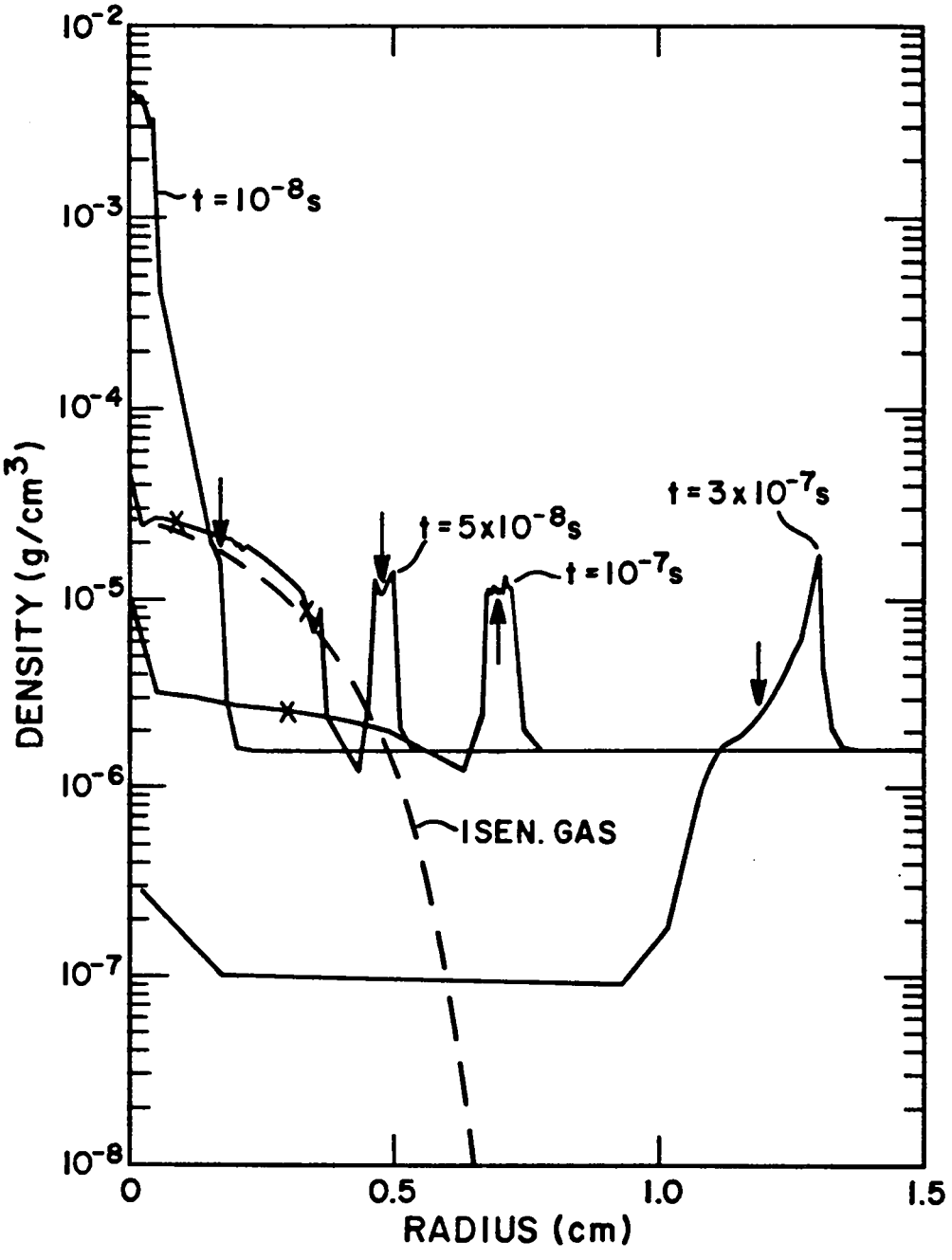

Fig. V-3. Numerically calculated density profiles for the 1-torr, E_s = 12.1 J, UNIF. ε calculated described in Fig. V-2. Arrows indicate interface between target material and shocked air. Xs indicate points where $p\rho^{-\gamma}$ was calculated in text. Dashed curve is the density profile of an ideal gas isentropically expanding into vacuum at t = 50 ns with E = 10 J, M = 3.4 μg, and γ = 1.2.

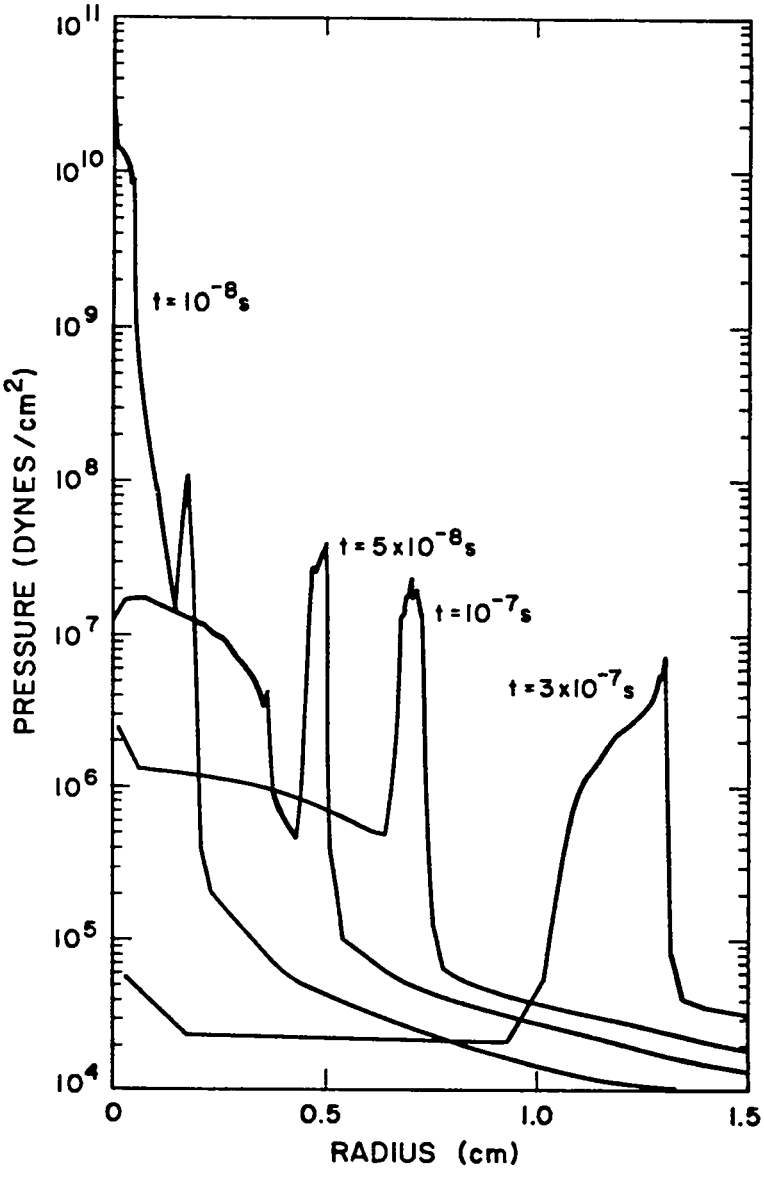

Fig. V-4. Pressure profiles that accompany the numerically calculated density profiles of Fig. V-3.

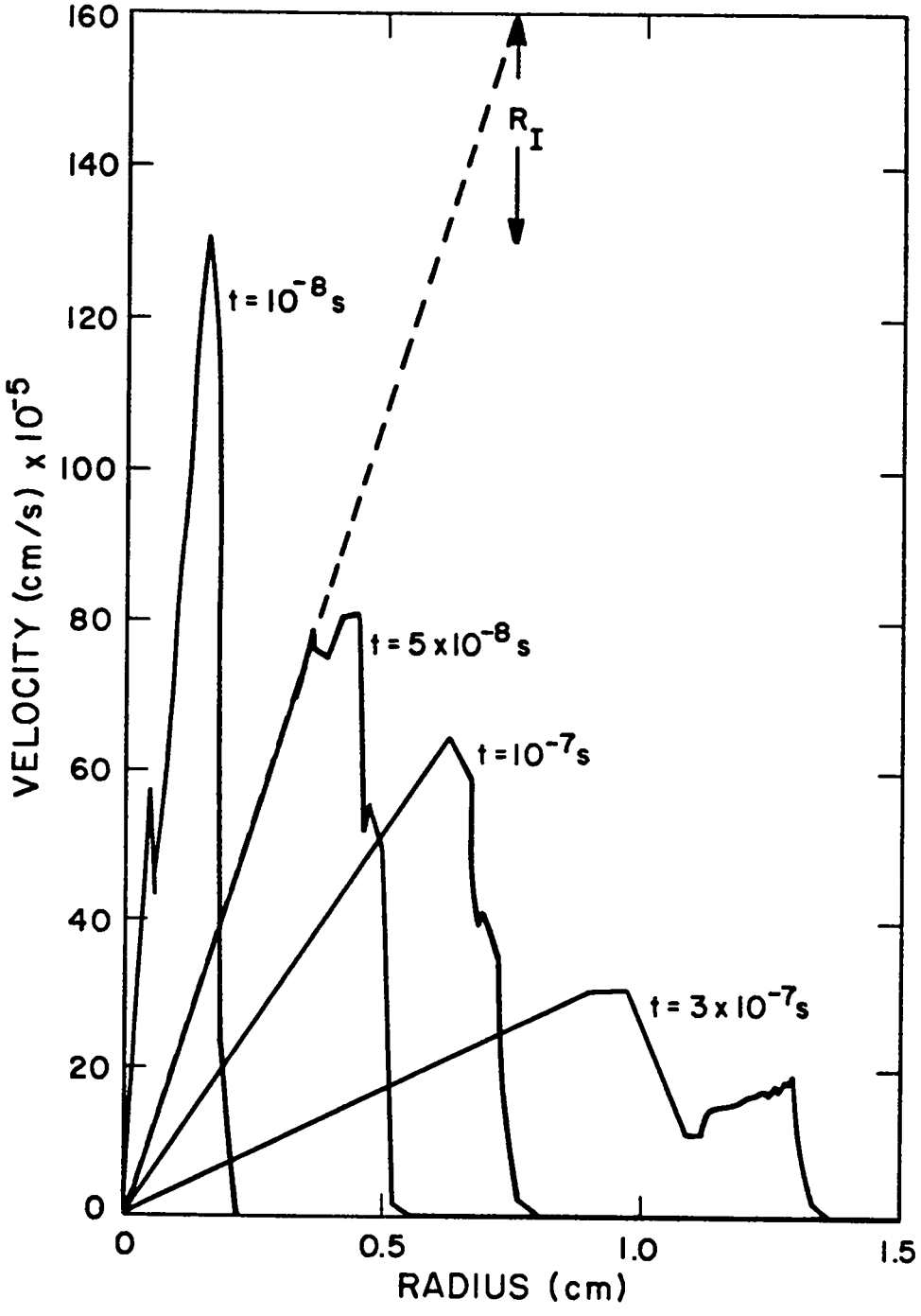

Fig. V-5. Velocity profiles that accompany the numerically calculated density profiles of Fig. V-3.

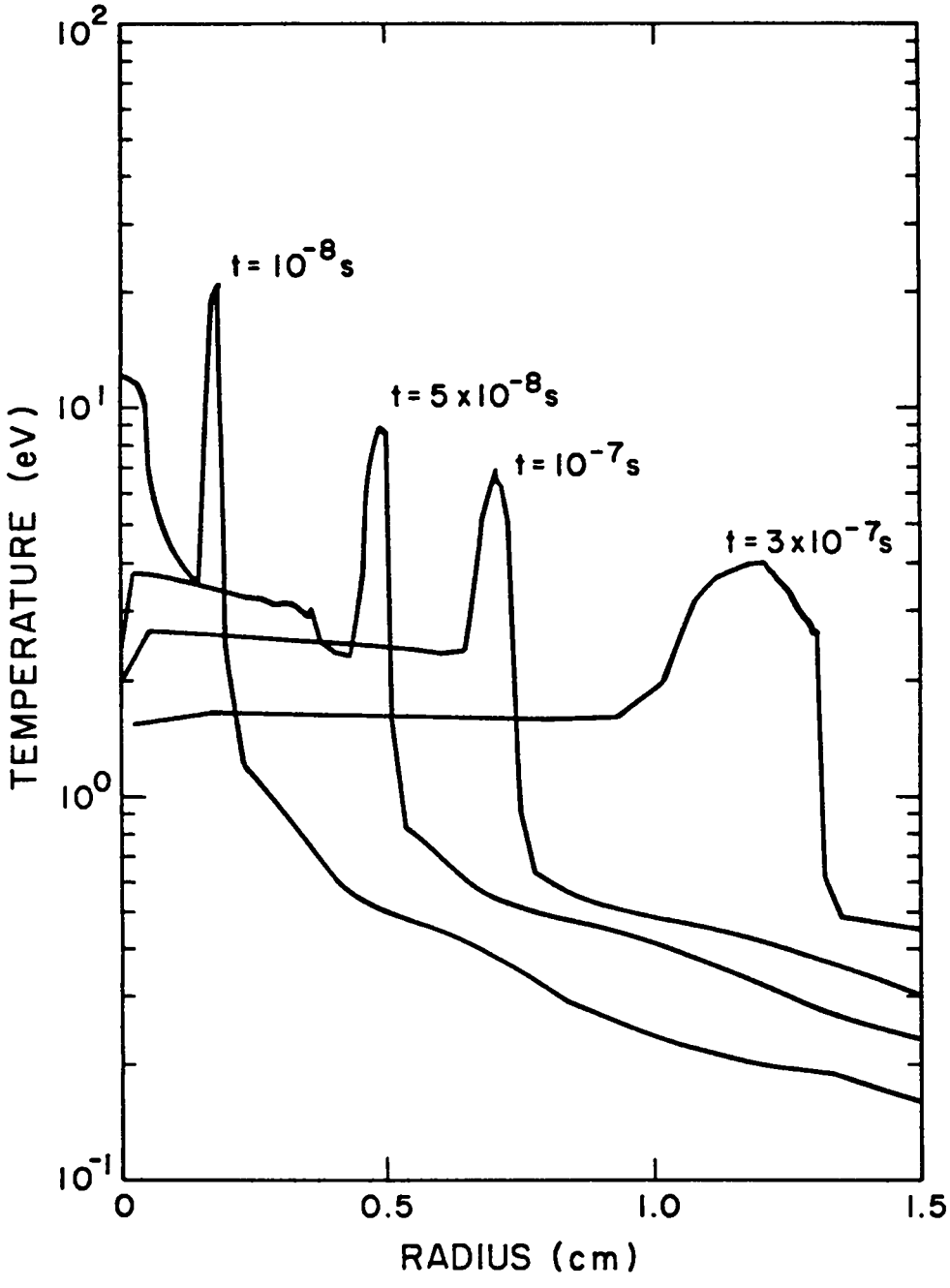

Fig. V-6. Temperature profiles that accompany the numerically calculated density profiles of Fig. V-3.

value of p/ρ^{γ} was calculated at the three points marked by the x's in Fig. V-3. It was found that if $\gamma = 1.2$ was used, the values were in good agreement (5.2 to 5.5 x 10^{12}). Therefore, p/ρ^{γ} is approximately constant, and the shock interior appears highly isentropic. The value of $\gamma \sim 1.2$ is consistent with the EOS data of Fig. III-2 and the model values of ρ, p, and T. The isentropic gas equations at the end of Chapt. IV were solved with $\gamma = 1.2$, $M_T = 3.4 \times 10^{-6}$, $E = 1. \times 10^{8}$, and initial values of $R_i = 0.025$ and $\dot{R}_I = 0$. The dashed curve in Fig. V-3 is a plot of the density at t = 50 ns when $R_I = 0.73$ cm. The dashed curve in Fig. V-5 gives the velocity distribution from the isentropic gas calculation at 50 ns. The isentropic gas velocity and density values agree well with the numerical calculations in the interior to 0.5 R_I. The 50-torr calculations gave similar results.

Centrally Deposited Energy

RADFLO is a one-dimensional code, so it can not be used to model the two-dimensional energy deposition and shock-wave expansion. However, the energy can be deposited with a nonuniform radial distribution to see if the expansion can be appreciably altered from that resulting when the energy deposition is uniform.

The cell radii in centimeters were 0.025, 0.02508, 0.02516, 0.02524, 0.02532, 0.0254, 0.0554, 0.0854, ... The target material extended from 0.025 to 0.0254 cm. The central cell had a density of 7.87×10^{-4} g/cm^3 in both the 1- and the 50-torr calculations. The next five cells had densities of 1.18 g/cm^3 and the remaining 113 cells had densities of 7.87×10^{-4} g/cm^3 (1.57×10^{-6}

g/cm^3) for 50-torr (1-torr) calculations. In this set of simulations, the entire energy was deposited in the central cell. The central energy distribution results in the heating of a small amount of mass, which creates a large E/M in the central cell.

The curves in Fig. V-2 labeled Cent. ε show the radius-vs-time dependence for a 2.5-J, 50-torr and 12.1-J, 1-torr calculation. By centrally depositing the energy, we obtain values of α for the early expansion which have increased over the values from the uniform E/M calculations. The agreement with the data, although better than in the previous sections, is still not good.

As mentioned, there is little difference between the calculations of the previous section and this section for late time when $\alpha = 2/5$. The Unif. ε and the Cent. ε curves go over to the $\alpha = 2/5$ expansion and show a separation of the shock from the luminous region at about the same time and radius.

Several density profiles for the 1-torr, 12.1-J calculation are plotted in Fig. V-7 for comparison with those of Fig. V-3. The arrows again mark the outer bondary of the target material. The calculation shows that the interior cell expands and pushes the target ahead plowing the ambient air into a shock wave. Some of the energy is radiatively transferred to the target material which also expands slightly. The division between the target and ambient air again remains at about 0.9 R_s. At 300 ns, a secondary density increase of shocked target material is apparent behind the shocked air.

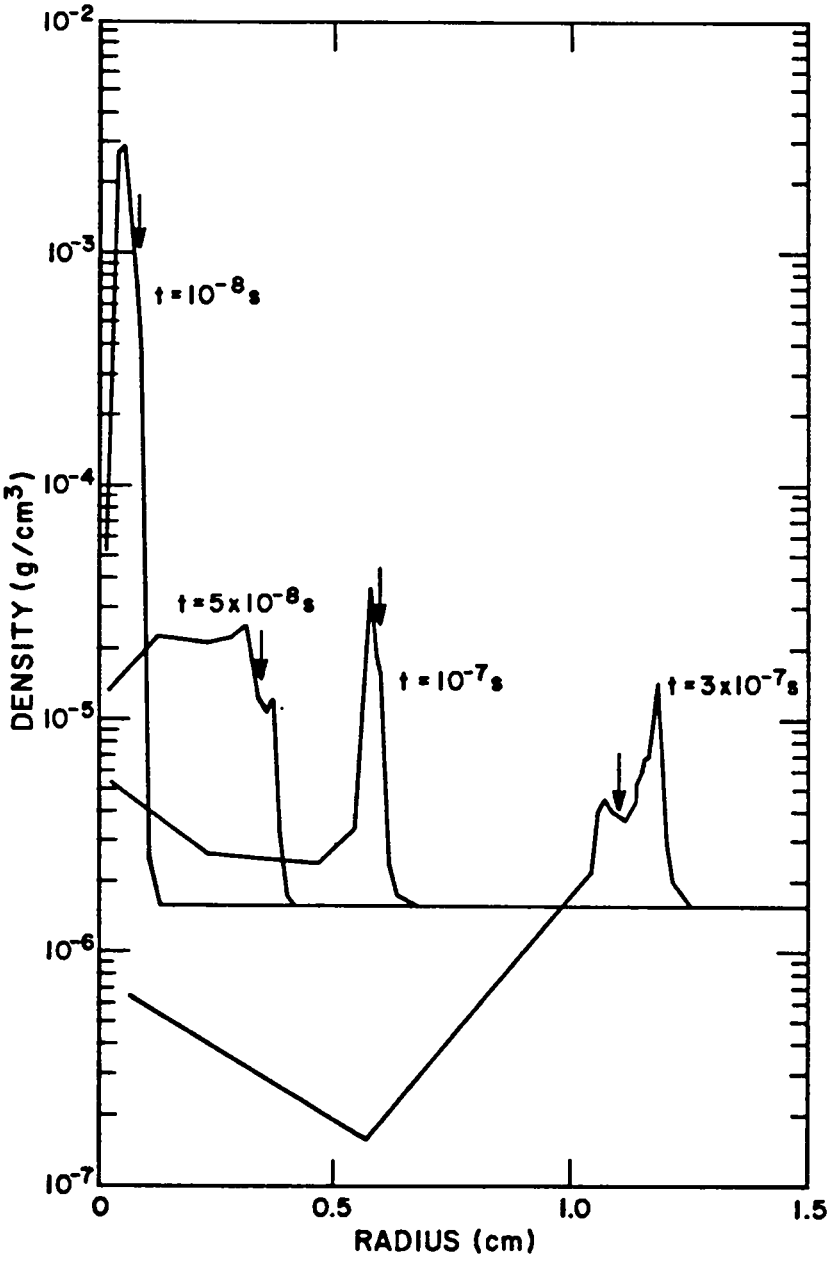

Fig. V-7. Numerically calculated density profiles for a 1-torr, 12.1-J, CENT. ε calculation.

Discussion

The results of the "uniform ε" model calculations for the density and velocity distributions indicate that the semiqualitative model at the end of Chapter IV is basically correct for a special case when the laser energy is evenly deposited through the target mass. In the experiment, the irradiance of the target is highly non-uniform because a single beam is used with a small spot-size relative to the target diameter. The results of the "central ε" model show that the early expansion rates can be significantly affected by non-uniformity in the initial energy distribution even though the energy distribution is still spherically symmetric.

In the experiment, the energy is distributed in the laser spot region and is therefore highly aspherical. The early-time observations of radius as a function of time are essentially measurements of the transverse radius. The transverse radius at a given time is less than the average radius of the shock. It would therefore be expected to show a slower expansion rate than that given by the spherical calculation.

It would be interesting to measure the early expansion of targets in a background gas with the targets uniformly illuminated by a multibeam laser. One would expect such measurements to match the "uniform ε" results.

Finally, we note that the ion measurements showed little difference between the transverse and the longitudinal plasma expansions. This could be due to a better distribution and transport of the laser energy through the target in the absence of the background

air. Another possible explanation is that the detectors were far enough away so that the plasma expansion may have become uniform by the time the measurements were made.

Density Profile Comparisons

The "central ε" simulation showed that nonuniform distribution of energy in the target could modify the expansion of the shock wave at early times. Because of the two-dimensional nature of the actual experiment, there is no reason to believe that either of the two simulations strictly models the early expansion. It is, however, interesting to see if the density data show any features that may distinguish between the models.

The earliest 1-torr interferometry data are at 600 ns when both model calculations indicate that the expansion is Taylor-von Neumann-Sedov. However, the numerical calculations of electron distributions still show some differences between the "central ε" and "uniform ε" distributions. The numerically calculated electron distributions and the gas density distributions can be used to calculate the index of refraction in a manner similar to that used to generate the calculated curve of Fig. III-11. The data of Fig. III-11 are plotted in Fig. V-8, along with η - 1 curves calculated from the numerically calculated density profiles assuming E_s = 12.1 J. The E_s for the data is 8 to 9 J, not 12.1 J. However, numerically calculated density profiles with E_s = 5 J differed only slightly from those with E_s = 12.1 J. There are no convincing similarities between either of the calculated curves and the data.

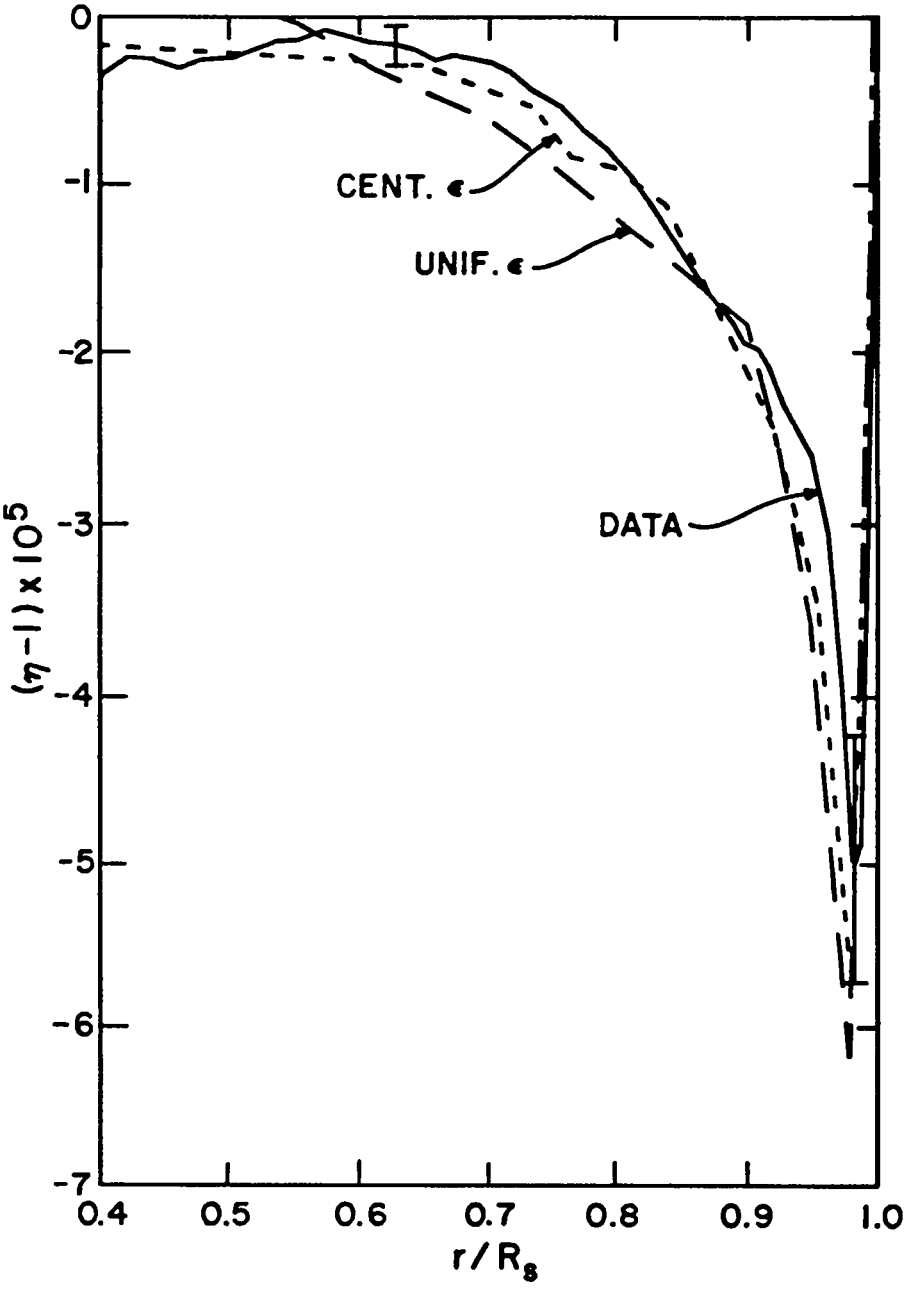

Fig. V-8. Comparison of numerically calculated $\eta - 1$ profiles, assuming E_S = 12.1 J and 1 torr, with measured profile of an E_L = 18.7 J, 1-torr shock at t = 600 ns.

The "central ε" curve in Fig. V-8 shows a finite $\eta - 1$ for small r/R_s as do the data, and the value of $\eta - 1$ at the shock front appears to be in agreement with the data. The "uniform ε" curve has a more negative value of $\eta - 1$ at the shock front that falls outside the data error bars. The central value of $\eta - 1$ for the "uniform ε" curve falls below measurable limits; however, the error bars in the data are large enough to cover this.

It has been noted in Chapt. III that the early 50-torr data show peaked electron densities and possibly secondary gas density spikes for profiles measured transverse to the beam. The earliest 50-torr data were at 425 ns when the R_s-vs-t is approaching TVS behavior. Figures V-9a and b are plots of the electron number density and gas density profiles from Fig. III-7, along with the numerical calculations for uniform and central energy deposition. The peak densities do not agree in either case. This may again be due to the loss of spatial resolution in the data at early times, exacerbated by the Abel inversion.

The secondary gas density increase is apparent on the Cent. ε curve of Fig. V-9a, and there is a suggestion of an increase in the data, but it is not convincing. The major difference between the two numerical calculations of electron density is the finite value of n_e at small normalized radii for the Cent. ε calculation. The Unif. ε calculation decreases near the center of the shock. Once again, the data agree with the Cent. ε calculation, but the agreement is far from convincing.

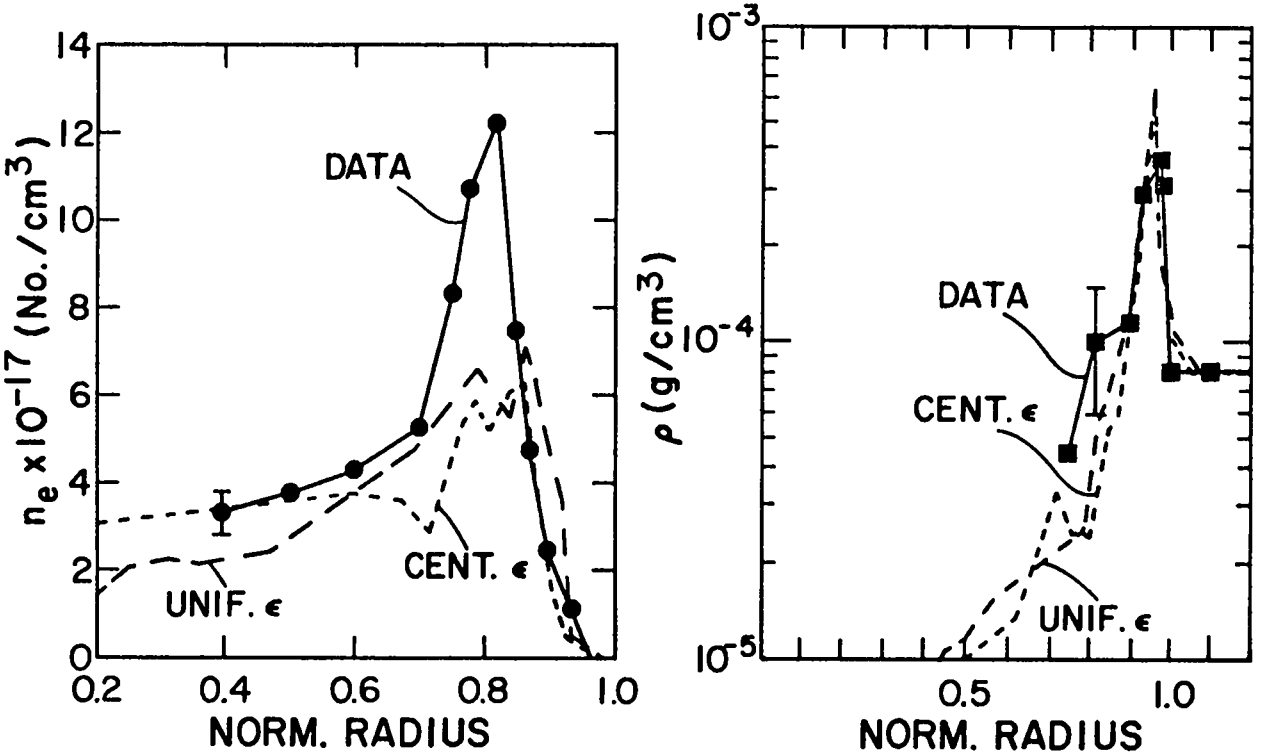

Fig. V-9. Comparison of numerically calculated electron number density and gas density profiles for 50-torr, E_l = 25 J shock with measured profiles described in Fig. III-6.

Summary

Chapter V describes the use of a nuclear effects hydrodynamic/ radiation transport code for modeling the data. The code was modified to include electron heat transport; however, this was found to have little significance, as predicted in Chapt. IV.

The code reproduces the Taylor-von Neumann-Sedov (TVS) phase of the data very well, including radius vs time, electron number density at the shock center, and peak gas density. The results for the TVS phase were independent of how the energy was deposited in the target.

When the code was started with the energy uniformly deposited in the target material, the early density and velocity profiles agreed with the isentropic gas description given at the end of Chapt. IV. The code was also started with the energy deposited in the central cell to test whether the early expansion rate could be influenced by non-uniformity in the energy deposition. The central-energy result showed a slower, more nearly constant initial velocity, in better agreement with the data than the result for the uniform-energy calculation. Data were compared with predicted density profiles for both the central- and uniform-energy calculations. However, at the time of the earliest data, the differences between the two calculations were not significant enough for either calculation to fall outside the error bars of the data.

Both calculations gave radius and time values for the transition to TVS expansion that agreed with the data. Both calculations also predicted correctly the time and radius at which the shock broke free from the luminous region.

It was concluded that comparisons of data and calculations are difficult because of the asymmetric laser illumination of the targets in this experiment.

CHAPTER VI

TWO-DIMENSIONAL SHOCK WAVES

In the previous chapter it was found that, for 50-torr shocks, the period during which $R_s \propto t^{2/5}$ (self-similar flow) could be accurately modeled on the computer. The numerical calculations agreed with the data, not only for R_s vs t, but for peak gas density and central electron density as well. The region of agreement covered $t \gtrsim 0.5$ μs and $R_s \gtrsim 0.6$ cm, and extended to late times when the shock was becoming sonic.

Two-dimensional 50-torr shocks are considered in this chapter. The spherical shocks are allowed to collide either with a reflecting plane or with a nearly identical shock to produce shock structures that are cylindrically symmetric. In the surface reflection experiment, the targets are 0.9 cm from a plane, while in the two-target experiments the targets are 1.8 cm apart. Thus, in both kinds of experiment, the two-dimensional period of expansion occurs when the individual shock wave properties are predictable. If the reflecting plane is an ideal surface, then a shock of say E_s = 2.5 J and centered 0.9 cm from the plane is equivalent to two identical, simultaneous shocks of E_s = 2.5 J each, with their shock centers separated by 1.8 cm. The reflecting plane and the symmetry plane perpendicular to the line joining the shock centers are then equivalent.

The interferograms in Fig. VI-1 are examples of the two types of experiments. Figure VI-1a shows a shock at 10 μs in 50-torr air generated by irradiating a target with a 16.8 J beam from the right, 45^{o} out of the plane of the page. The shock has collided with a clear acrylic plastic block suspended 0.9 cm above the target. The clear block was used in order to obtain a qualitative idea of the shock coupling to the plane. A density wave can be seen propagating through the block away from the surface. Figure VI-1b shows two colliding shock waves at 20 μs. The right shock was generated by a 26.0-J pulse from the right 45^{o} out of the plane of the page and the left was generated by a 22.4-J pulse from the left 45^{o} into the plane of the page. The targets are 1.8 cm apart.

At 10 μs and 20 μs, the shocks are very nearly spherical. However, the shock center does not coincide with the target because of the combined effects of air breakdown and asymmetric laser irradiation (see Chapt. II). The shock center is located away from the target toward the Nd:glass laser. The separation of the shock center and target in the plane of the interferogram is typically 0.15 cm at 20 μs. Therefore, even though the targets in Fig. VI-1b are 1.8 cm apart, the shock centers are farther apart and the line separating the shock centers is at a slight angle to the plane of the interferogram. The reflecting shock center is still 0.9 cm from the reflector because the shift is parallel to the surface.

Early comparisons [Wilke and Stone (1979)] were made between the individual radii of two near-identical interacting shock waves at a given time and the radius of a single spherical shock of the same

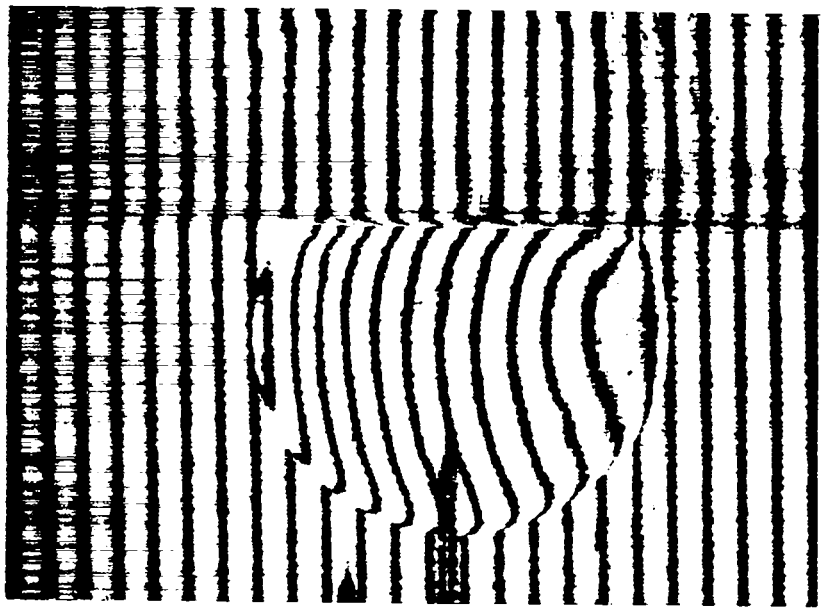

(a) A 50-torr, E_L = 16.8 J shock at 10 μs reflecting from an acrylic plastic block 0.9 cm above target. Beam was from the right and out of the page.

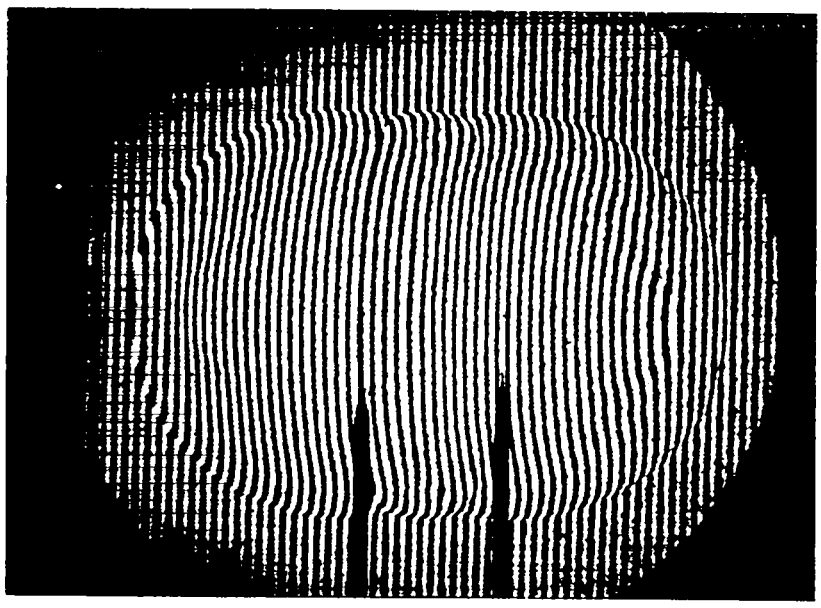

(b) Two 50-torr interacting shocks at 20 μs. The targets were 1.8 cm apart. E_L was 26.0 J for the right shock and 22.4 J for the left shock.

Fig. VI-1. Examples of the two types of two-dimensional shock experiments:

energy. These comparisons initially showed a difference, but many repetitions of the experiment since indicate the radii are equal within experimental error.

Terminology and Scaling

When a spherical shock collides with a plane, the angle α_I between the incident shock and the plane is initially oblique, and the shock reflects regularly. At larger shock radii, the angle becomes larger, and the interaction between the incident and reflected shocks forms a third shock, called the Mach stem. The value of α_I at which the Mach stem develops is the critical angle, α_c. The intercept of the three shocks is called the triple point, and it follows a path of increasing distance from the plane. Figure VI-2 defines the variables and shock features. The value of R_Z (the distance from "ground zero" to the shock-plane intercept) at which the Mach stem begins to form is a function of the shock Mach number M_S and height of shock center D. The value of M_S is a function of R_S and is determined by the shock energy E_S and the ambient conditions. The path of the triple point and the time-history of the angle θ are then also determined.

Various more complicated Mach structures are possible and several have been investigated in planar geometry by Ben-Dor (1978). Analytical descriptions of planar Mach reflections also exist, but the spherical equivalents do not.

The question arises as to how the two-dimensional laser shock waves compare with large-scale two-dimensional shock waves produced

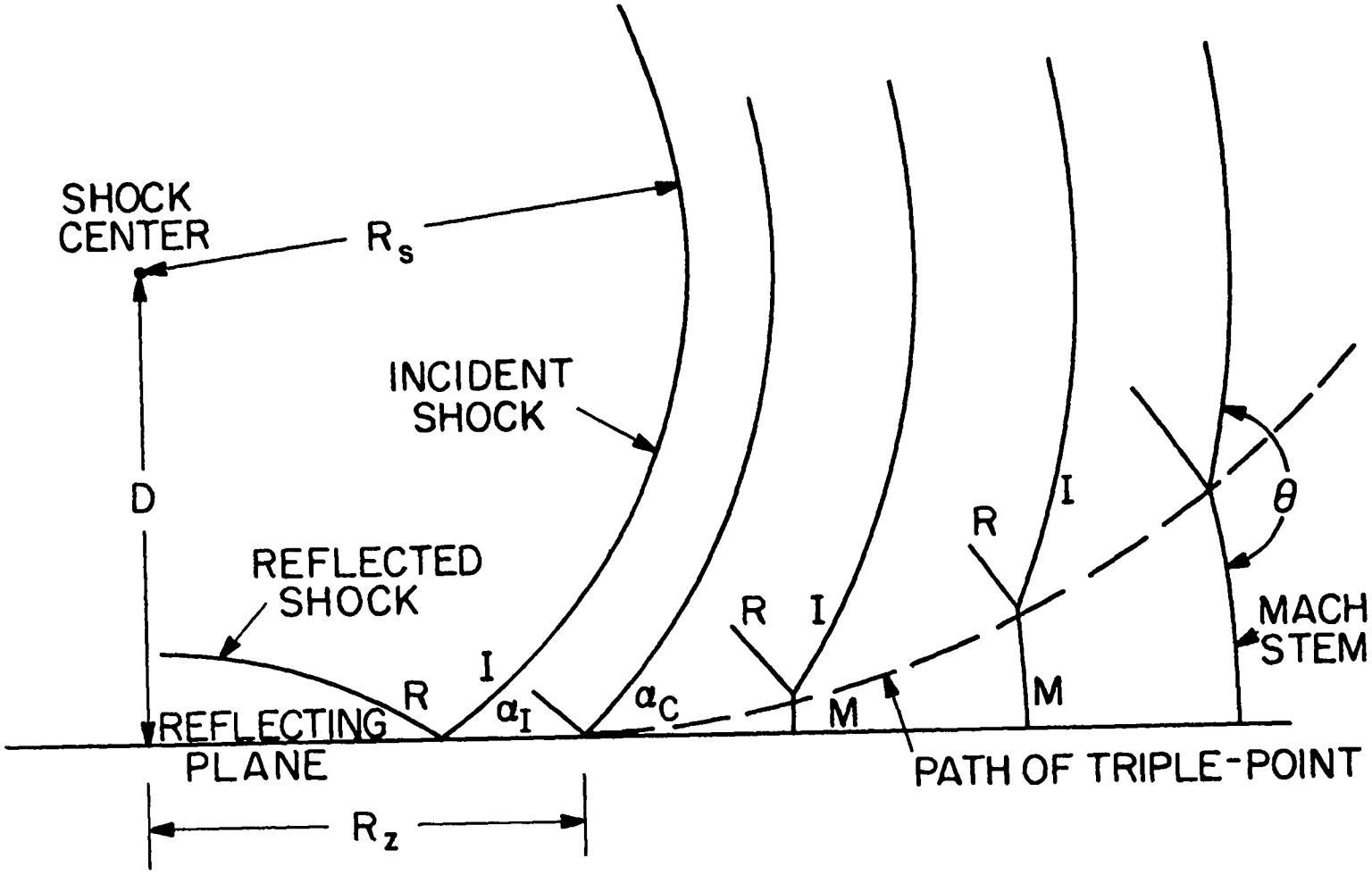

Fig. VI-2. Schematic of a reflecting spherical shock wave.

by high explosives or nuclear detonations. High-explosive and nuclear two-dimensional shock wave data exist for shocks reflected from a ground plane. The ambient conditions of such shocks are different as well as the energy and height D. In order to make such comparisons, it is necessary to employ scaling laws that account for the differences in a manner consistent with the equations describing the flow. In this case, Sachs scaling is used [see Baker (1973)].

Any scaled set of dependent and independent variables that are solutions to an equivalent scaled problem must satisfy the differential Eqs. (IV-22) to (IV-24). If (assuming constant scaling)

$$r = \bar{r}\, r' \qquad \text{(VI-1)}$$

and

$$t = \bar{t}\, t' \quad , \qquad \text{(VI-2)}$$

then the scaled (primed) solutions given by

$$p(r,t) = \bar{p}\, p'(r',t') \quad , \qquad \text{(IV-3)}$$

$$u(r,t) = \bar{u}\, u'(r',t') \quad , \qquad \text{(IV-4)}$$

and

$$\rho(r,t) = \bar{\rho}\, \rho'(r',t') \qquad \text{(IV-5)}$$

must satisfy Eqs. (IV-22) to (IV-24), where the barred quantites are dimensionless constants. If Eqs. (VI-1) to (VI-5) are used to

replace r, t, p, u, and ρ in Eq. (IV-23), then an identical primed version of Eq. (IV-23) is obtained, provided that

$$\bar{p} = \bar{\rho}\,\bar{u}^2 \quad . \tag{VI-6}$$

Similarly, both Eq. (IV-22) and Eq. (IV-24) scale if

$$\bar{r} = \bar{u}\,\bar{t} \quad . \tag{VI-7}$$

The internal variables are matched across the shock boundary to the ambient conditions using the Hugoniot conditions and shock front values of the variables R_s, ρ_s, p_s, and u_s. We have previously assumed the strong-shock Hugoniot relations at the boundary. However, the experimental results and numerical calculations show that the period of self-similar expansion extends to times when the shock front density is much lower than $\rho_o(\gamma + 1)/(\gamma - 1)$. Therefore, we will use the exact Rankine-Hugoniot relations for an ideal gas

$$\dot{R}_s(\rho_s - \rho_o) = \rho_s u_s \quad , \tag{VI-8}$$

$$p_s - p_o = \rho_s u_s \dot{R}_s \quad , \tag{VI-9}$$

and

$$\left(\frac{p_s}{\rho_s} - \frac{p_o}{\rho_o}\right)(p_s - p_o) = \frac{\gamma - 1}{2}\, u_s^2 (p_s + p_o) \quad . \tag{VI-10}$$

The results of this section, however, are identical even if the strong-shock relations are used. Substituting Eqs. (VI-3) and (VI-4) and using

$$\dot{R}_s = \frac{dR_s}{dt} = \frac{\bar{r}}{\bar{t}} \frac{dR_s'}{dt'} \qquad \text{(VI-11)}$$

as well as Eqs. (VI-6) and (VI-7) in Eqs. (VI-8) to (VI-9), we get equivalent and therefore scaled forms of Eqs. (VI-8) to (VI-10) in the primed variables, provided the ambient conditions p_0 and ρ_0 are scaled as

$$p_0 = \bar{p}\, p_0' \qquad \text{(VI-12)}$$

and

$$\rho_0 = \bar{\rho}\, \rho_0' \,. \qquad \text{(VI-13)}$$

The scaling of the shock wave energy (E_s) is determined from the normalization integral given in Eq. (IV-29). Eq. (IV-29) asssumes $p_0 << p(r,t)$, as do the strong shock Hugoniot relations. The exact form of Eq. (IV-29) is

$$E_s = 4\pi \int_0^\infty [\rho u^2/2 + (p - p_0)/(\gamma - 1)] r^2 dr \,. \qquad \text{(VI-14)}$$

Substituting for ρ, u, p, p_0, and r and using Eq. (VI-6) yields

$$E_s = 4\pi\, \bar{r}^3\, \bar{p} \int_0^\infty [\rho' u'^2/2 + (p' - p_0')/(\gamma - 1)] r'^2 dr' \,. \qquad \text{(VI-15)}$$

Therefore, the E_s scaling law is

$$E_s = \bar{r}^3\, \bar{p}\, E_s' \,. \qquad \text{(VI-16)}$$

For the specific problem considered here, it is assumed that the ambient temperatures T_o and T'_o are the same. Therefore, because $p_o \propto \rho$, $p_o/p_o' = \rho/\rho'$ so that

$$\bar{p} = \bar{\rho} \quad . \tag{VI-17}$$

This, together with Eq. (VI-6) requires that

$$\bar{u} = 1 \quad . \tag{VI-18}$$

Then by Eq. (VI-7),

$$\bar{r} = \bar{t} \quad . \tag{VI-19}$$

Substituting from Eqs. (VI-1) and (VI-12) for $\bar{r}$ and $\bar{p}$ in Eq. (VI-16) yields the scaling law

$$\frac{r'}{r} = \left(\frac{E_s'}{E_s}\frac{p_o}{p_o'}\right)^{1/3} \tag{VI-20}$$

and by Eq. (VI-19),

$$\frac{t'}{t} = \left(\frac{E_s'}{E_s}\frac{p_o}{p_o'}\right)^{1/3} \quad . \tag{VI-21}$$

That is, the primed and unprimed problems are equivalent when both the radial dimensions and the times are scaled by the ratio $(E_s'p_o/E_sp_o')^{1/3}$. In this event, it also follows that $p'(r',t') = p_o p(r,t)/p_o'$, $\rho'(r',t') = \rho_o\rho(r,t)/\rho_o'$, and $u'(r',t') = u(r,t)$.

A laser shock originating at a distance D from a plane with energy E_s in ambient air of pressure p_o is equivalent to a large-scale shock wave with energy E'_s a distance D' from the ground in an ambient atmosphere of pressure p'_o, provided Eq. (VI-20) holds with r and r' replaced by D and D'. Then laser-shock measurements taken at radius r and time t correspond to large-scale measurements taken at radius r' and time t' given by Eqs. (VI-20) and (VI-21). Typical values of p_o = 50 torr, p'_o = 700 torr, E_s = 2.5 J ($E_L \simeq 25$ J) and D = 0.9 cm imply that the equivalent large-scale shock must have

$$\frac{D'}{(E'_s)^{1/3}} = 44.4 \quad , \qquad \text{(VI-22)}$$

where D' is in meters and E_s' in kiloton TNT equivalent (1 kiloton = 4.19×10^{12} J). This value is much smaller than is possible in high-explosive experiments [Dewey McMillin and Classen (1977)], and corresponds to nominal-yield nuclear explosions tens of meters above the ground.

The Teapot/Met event of 1955, with a yield of 22 kt, was initiated on a 122-meter tower [Glasstone (1962)]. Therefore, the value of $D'/(E'_s)^{1/3} = 43.5$ m/(kt)$^{1/3}$ closely matches the laser experiments.

A picture (Fig. VI-3a) of the Teapot/Met nuclear test at 170 ms shows the Mach stem traveling along the ground surface ahead of the incident spherical shock. The spherical shock radius at this time was 285 m, or 2.34 times the tower height. According to Eq. (VI-20), the equivalent burst height for a 2.5-J laser shock at 50 torr is 0.92 cm. The scaled time for the laser shock, equivalent to the

(a) Teapot/Met event (22 kt, 122 m above the ground) at t = 170 ms. Arrow indicates Mach stem and precursor ahead of the shock front.

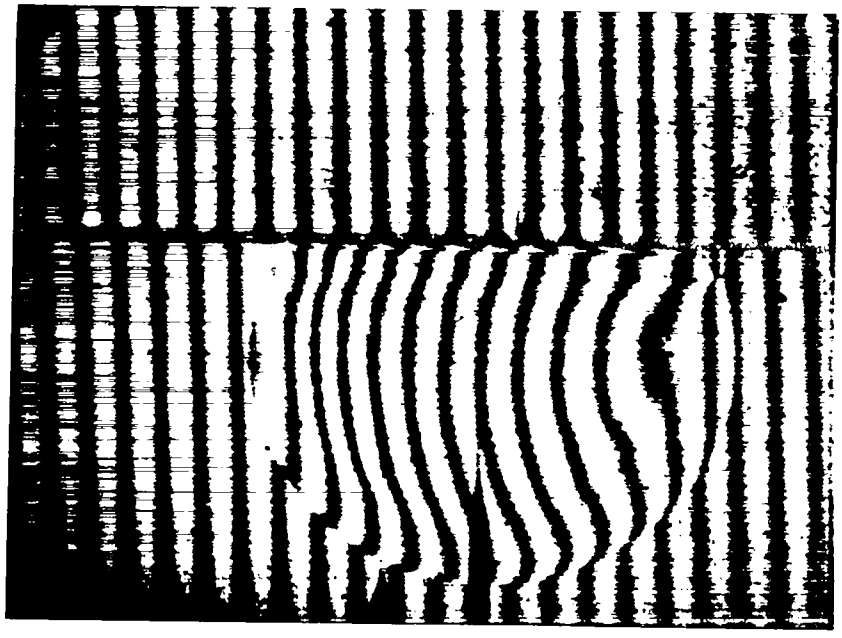

(b) 50-torr, E_L = 20.1 J laser shock wave at t = 15 μs.

Fig. VI-3. Comparison of a large-scale, low-altitude nuclear shock with a reflected laser shock:

170-ms Teapot/Met time, is 12.3 μs. It was shown in Chapt. V that numerical computations for a 2.5-J spherical shock at 50 torr corresponded to a spherical shock data set with a laser energy E_L of 25 J. A corresponding set of reflected shock experiments was run at 50 torr with $E_L \simeq 25$ J (and therefore $E_s \simeq 2.5$ J) with a burst point-to-plane separating distance of 0.9 cm. Thse experiments are therefore closely comparable with the Teapot/Met test. The measured Teapot/Met spherical shock radius of 285 m at 170 ms scales to a shock radius of 2.15 cm for the equivalent 50-torr, E_s = 2.5 J, laser experiment at 12.3 μs. If we interpolate from the compiled individual shock wave data of Chapt. II for E_L = 25 J at 12.3 μs, the shock radius is 2.15 cm, in excellent agreement.

Figure VI-3b is an interferogram of a reflecting shock with E_L = 20.1 J (and therefore $E_s \simeq 2$ J) taken at 15 μs. Figure VI-4 is a schematic comparing the left side of Fig. VI-3b with the Teapot/Met shock. The comparison was done by superimposing the reflecting plane and shock centers [note the target is to the left of the laser-shock center] and tracing the shock wave boundaries. The agreement is qualitatively good, however, the nuclear shock triple-point is higher and θ is less than the corrresponding values of the laser shock.

The ground plane in a nuclear explosion is far from a perfect reflector. Visible and infrared radiation from first the isothermal sphere and later the fireball pass through the surrounding air and strikes the ground, heating it to high temperatures. Dust from the hot ground is thrown into the air by steam from the ground moisture and also by convection. An underground density wave generated from

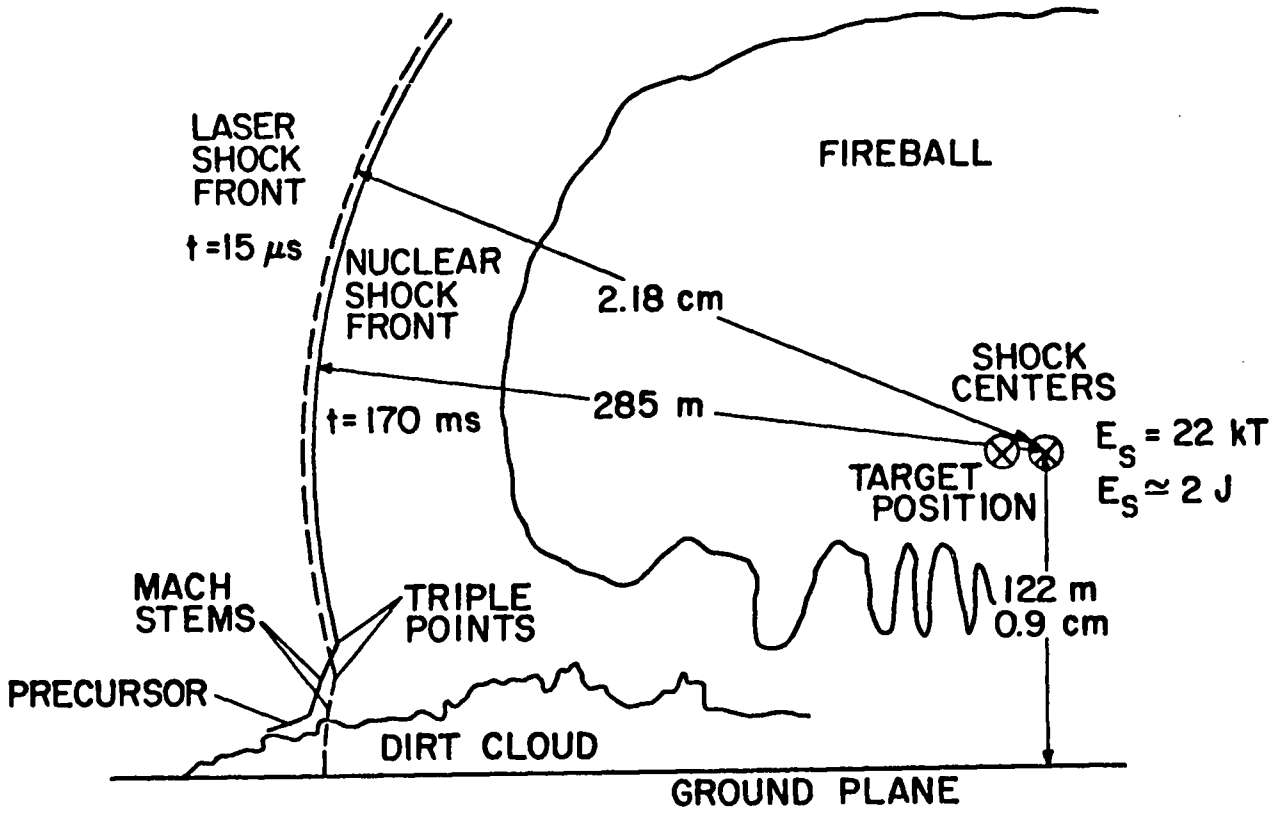

Fig. VI-4. Schematic comparison of left side of the laser shock in Fig. VI-3 with the Teapot/Met shock. Comparison was made by superimposing shock centers and reflecting planes, and then tracing shock boundaries.

coupling of the early air-shock to the ground plane eventually outruns the air-shock and also throws heated dust into the air ahead of the shock wave. The small dust particles transfer heat by conduction to the surface layer of air. The base of the Mach stem propagates at a higher velocity through this heated air. This leads to the precursor and dirt cloud shown in Fig. VI-3. It may be that the upper portion of the Mach stem is actually riding on the precursor. This would result in a higher triple-point and smaller θ.

Two-Dimensional Numerical Modeling

A two-dimensional hydrodynamics code [Sandford et al (1975)] was adapted to model the laser reflected shock experiments. The two-dimensional computation starts from the one-dimensional output of RADFLO at the time when the spherical shock just begins to collide with an ideal reflecting plane. An "ideal" reflecting plane is one that does not move or conduct heat and the air at the interface can only move along the plane without friction.

The current version of the code uses YAQUI [Hirt et al (1974)], an implicit two-dimensional arbitrary Lagrangian-Eulerian hydrodynamics code, and an automatic rezoner [Horak et al (1978)]. The code includes S_n radiation transport [Lathrop and Brinkley (1973)], but radiation transport is of little significance in the laser-shock problems at the times of interest.

The two-dimensional problem was set up with a cylindrical mesh of cells extending 2.1 cm in the radial direction and 3.0 cm in the z-direction. The plane was assumed to be along the bottom of the

mesh and the shock center was 0.9 cm above this on the left border of the mesh. The cells were initially 0.03 x 0.03 cm.

The RADFLO run used for input to the two-dimensional code was the "Uniform ε" run described in Chapter V for 50-torr ambient conditions with E_s = 2.5 J. The two-dimensional code picked up the run at $t \simeq 1$ μs when the shock was about 0.8 cm in radius and ran to about 24 μs when the shock radius was about 2.9 cm.

The results of the numerical calculation indicate that the Mach stem begins to form at about 5.5 μs. Figure VI-5 is a composite of shadowgraphy sequences of double shocks with $E_L \simeq 25$ J for both laser beams. The Mach stem is just becoming visible in the 6.5-μs shadowgraph. The shock centers in the experiment are $\simeq$ 1.05 cm from the plane of symmetry instead of 0.9 cm as in the calculation. This would result in a slightly later Mach formation in the experiment. Thus, the overall agreement is excellent.

At 5.5 μs, when the Mach stem begins to form, R_s = 1.47 cm for a 2.5 J shock in 50-torr air. The relation between α_I and R_s in Fig. VI-2 is given by

$$\cos \alpha_I = D/R_s \quad . \tag{VI-23}$$

Therefore, α_c is 52^0 for R_s = 1.47 cm.

We define the ratio of ambient pressure to shock front pressure as ψ; that is,

$$\psi = p_o/p_s \quad . \tag{VI-24}$$

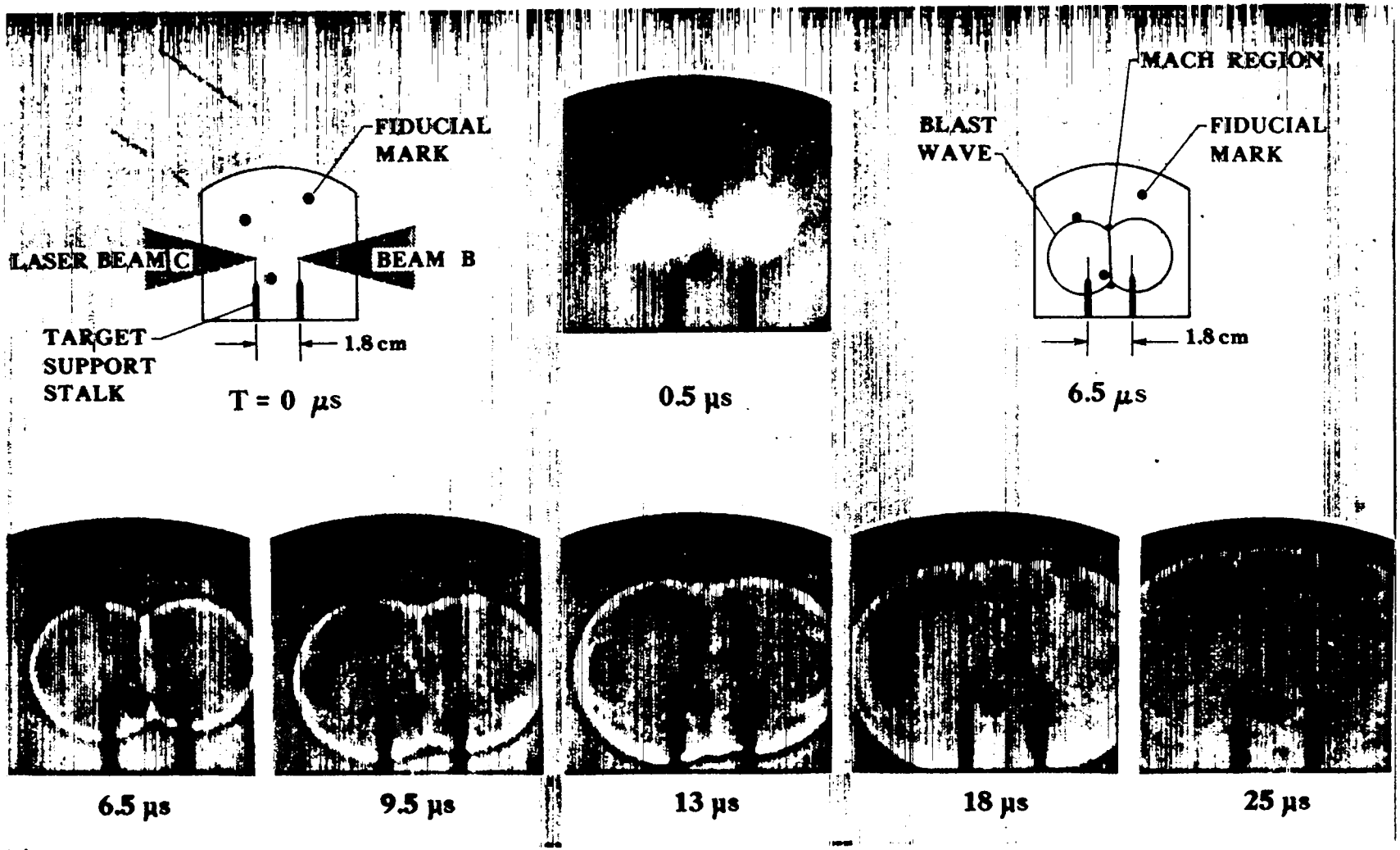

Fig. VI-5. Composite of shadowgraphy sequences of double shocks, with E_L = 25 J for each shock.

In the reflecting planar-shock case, α_c is a unique function of ψ. α_c shows a strong decrease from 90^o at $\psi = 1$ to 42.5^o at $\psi = 0.5$ for $\gamma = 1.4$ [Harlow and Amsden (1971)]. For increasingly smaller values of ψ, α_c asymptotically approaches 40^o. Therefore, no matter how strong a planar shock is, α_c will never be less than $\sim 40^o$.

It is useful to compare our value of α_c versus ψ with the planar case. For 50 torr, the cgs value of p_o is 6.8×10^4 dynes/cm^2. We can calculate the self-similar value of p_s, using Eqs. (II-7), (III-22), and (III-24) and assuming $\gamma = 1.4$ and $\xi = 0.85$. This yields

$$p_s = 0.157\ E_s\ R_s^{-3} \quad . \qquad \text{(VI-25)}$$

With $E_s = 2.5$ J (2.5×10^7 ergs) and $R_s = 1.47$ cm, $p_s = 1.2 \times 10^6$ dynes/cm^2 and $\psi = 0.06$. The one-dimensional numerical calculations yield $p_s = 7 \times 10^5$ dynes/cm^2, so that $\psi = 0.1$.

The planar value of α_c for $\psi \sim 0.1$ is very close to the limiting value of $\sim 40^o$. It is interesting to note that our experimental value of $\alpha_c = 52^o$ for the spherical case and $\psi \sim 0.1$ is greater than the planar value of α_c for $\psi \sim 0.1$.

Figure VI-6 shows the numerically calculated shock boundaries, as long dashed lines, for several times. The triple-point path was fitted by eye, and the dashed portion of the path is an estimated extrapolation. Several measured reflecting-shock interferograms were projected on the plot, so that the shock centers and reflecting planes were superimposed on the corresponding center and plane from

the numerical model. The boundaries were then traced and are indicated by the short dashed lines. The radii of the small circles about the triple points are an estimate of the uncertainty of the location of the triple point. Table VI-1 describes the numbered curves. The long-short-dashed lines are boundaries measured from interferograms of the double-shock experiments. The double shocks were projected so that the plane of symmetry was superimposed on the numerical reflecting plane and the target position was at 0.9-cm height. The shock center was then at 1.05 cm above the plane, as indicated in Fig. VI-6.

Table VI-1 indicates that E_L varied from 16.8 to 28.3 J for the reflected-shock data. Equation (VI-20) shows there is only a one-third root dependence on energy. Therefore, there is at most only a 10% effect due to the variation in the E_L about 25 J, the E_L-value equivalent to the E_S = 2.5 J that was assumed in the numerical calculation.

Because the shock-center-to-reflecting-plane distance is greater for the double-shock experiment, the Mach effect should occur at a larger R_Z and the triple-point path should fall below the reflecting shock triple-point path. Curve number 5 has a triple point falling below the triple-point path of the reflecting-shock data and calculations and is therefore in qualitative agreement with predictions.

It can be concluded that the agreement between the nuclear-shock and the scaled laser shock is qualitatively good. The agreement between the laser shocks and the computer-simulated shocks is excellent.

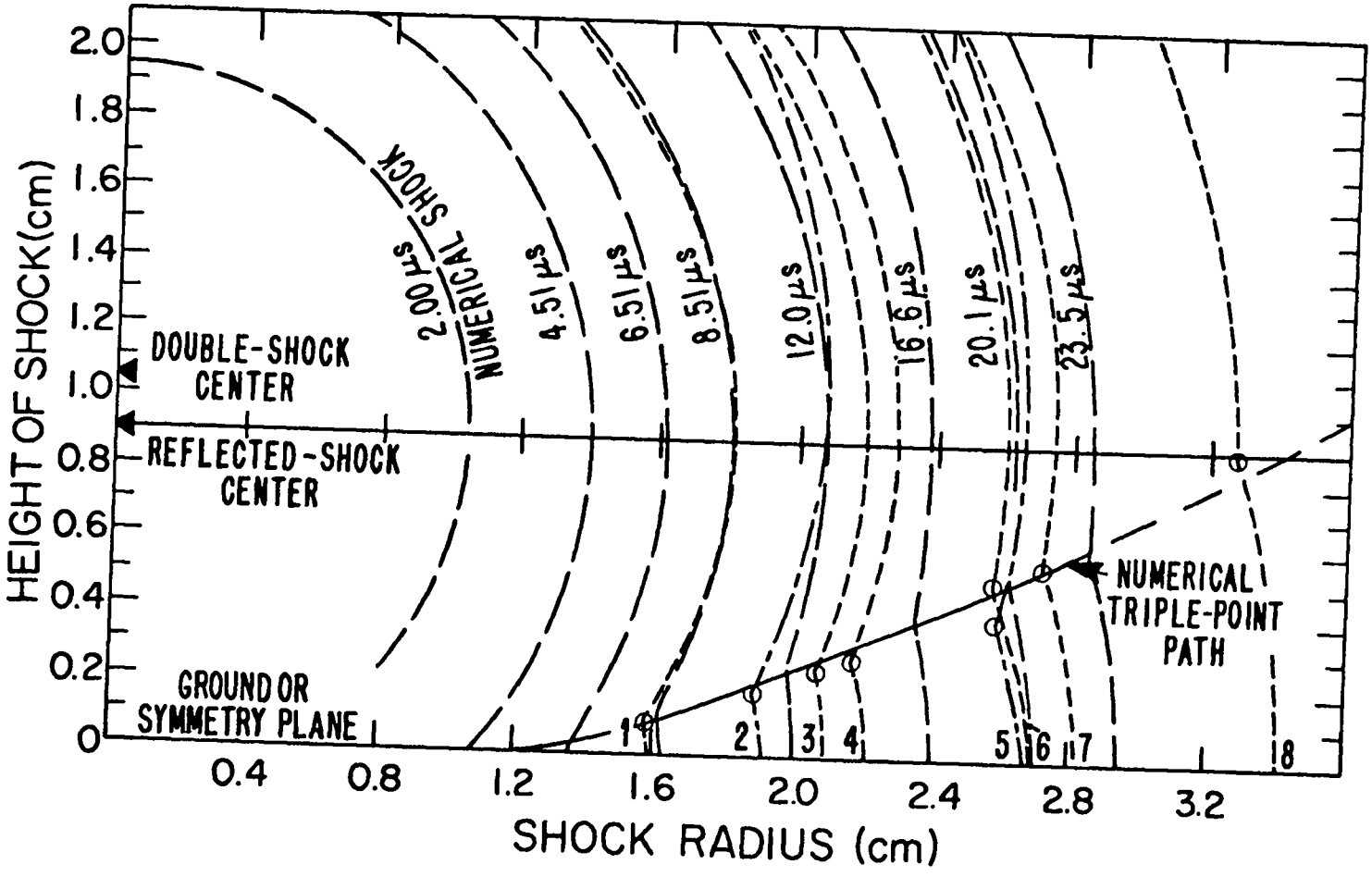

Fig. VI-6. Comparison of numerically calculated shock boundaries (long dashes) with experimental shock boundaries (short dashes and long-short dashes). See Table VI-1 for descriptions.

TABLE VI-1

TWO-DIMENSIONAL SHOCK INFORMATION FOR FIG. VI-6

No.	Time (μs)	Energy (J)	Description
1	10.0	16.8	Shock and reflecting plane
2	10.5	28.8	B-shock of double-shock experiment E_L(C-beam) = 30.7 J
3	15.0	20.1	Shock and reflecting plane
4	15.0	22.4	Shock and reflecting plane
5	20.0	26.0	B-shock of double-shock experiment E_L(C-beam) = 22.4 J
6	20.0	22.1	Shock and reflecting plane
7	20.0	28.3	Shock and reflecting plane
8	30.0	24.8	Shock and reflecting plane

Summary

In this chapter, we have described two-dimensional experiments involving the reflection of a spherical laser shock wave from a plane or the interaction of two spherical shock waves.

The laser shocks were compared to a reflected nuclear shock, using scaling laws. The scaled nuclear shock geometry and the laser shock geometry were nearly identical, with differences attributable to the non-ideal reflecting surface of the ground.

Two-dimensional computer modeling of the laser shocks was then conducted. The computer calculations closely matched the laser shock geometry.

CONCLUSIONS

This thesis has investigated laser-target generated shock waves in low-pressure air. The experimental results can be divided into two categories: results from approximately one-dimensional near-spherical individual shock wave experiments, and results from two-dimensional shock wave experiments involving the collision of a spherical shock wave with a plane or the interaction of two spherical shock waves.

The individual spherical shock wave experiments were performed both because of interest in the individual shocks themselves and in order to gain a detailed understanding of the single shock waves before they were used for the two-dimensional experiments. The individual shock waves were observed to go through two phases of expansion. During the first phase, the shock waves expanded with a near-constant radial velocity in the direction transverse to the laser beam. The second phase was defined to begin when the radius-vs-time relation for the shock waves became that of a Taylor-von Neumann-Sedov (TVS) shock wave where $R_s \propto t^{2/5}$. The R_s-vs-t data from the beginning of the second-phase expansion were used to assign a shock-wave energy based on the energy dependence of the TVS relation and also on comparisons with R_s-vs-t predictions from numerical models.

The early-phase deviation from TVS expansion was attributed partly to the presence of non-negligible target mass and partly to the initial non-uniform distribution of energy in the target material following laser irradiation. Non-linear electron heat transport was found to have a negligible influence on the early expansion, contrary to suggestions by others cited in the introduction.

Several one-dimensional spherical analytical approximations that include source mass were investigated, but none showed convincing agreement with the data. The points of comparison between the data and approximations were R_s vs t, and the gas density and electron number density profiles obtained from Abel-inverted interferograms of the shock wave.

The most promising model of the early expansion is that of an isentropically expanding gas supplying energy to the surrounding shocked air, driving the air shock as a variable-energy blast wave. One-dimensional numerical calculations using a nuclear-effects hydrodynamics code tended to agree with this model. Calculations predicted a somewhat different initial expansion rate than was observed; however, the difference might be attributed to the initial asphericity of the shcok waves resulting from the non-uniform laser irradiation.

The measured density profiles also tended to agree with the isentropic gas model, but the agreement was only suggestive. Due to triggering requirements, it was impossible to obtain interferograms, and therefore density profiles, at times early enough to conclusively confirm the validity of the isentropic gas model.

A more detailed investigation of the effects of target mass would require multi-beam, near-symmetric laser irradiation of the targets and shock-wave diagnostics specifically designed to observe early-phase expansion.

During the later phase, the shocks were found to expand as TVS blast waves, finally slowing to sonic velocities. Interferometric measurements of the density during the TVS phase showed that the peak gas density fell quickly below the predicted value of $\rho_s = \rho_o (\gamma + 1) / (\gamma - 1)$, even though the shocks still expanded with $R_s \propto t^{2/5}$ for some time afterwards. The one-dimensional numerical calculations showed excellent agreement, through the sonic transition, with the later-phase experimentally measured time dependence of R_s, the peak gas density, and the central electron density. The self-similar expansion is apparently not strongly dependent on the strong shock assumption.

Two kinds of two-dimensional shock interaction experiments were conducted. The first consisted of reflecting a spherical shock from a plane 9 mm away in 50-torr air. The second involved the collision of two nearly identical, spherical shock waves whose centers were about 18 mm apart. The distances were chosen (based on the one-dimensional results) so that two-dimensional interactions began when the shocks had entered the second (TVS) phase.

A reflected laser shock wave was compared with a scaled nuclear shock wave. The triple-point height and Mach stem geometry compared favorably. Differences could be attributed to the non-ideal

reflecting ground surface in the nuclear case. These results indicate that the scaling laws for two-dimensional experiments can be applied over a factor of 4×10^{13} in energy.

Two-dimensional numerical calculations were compared with the observations. The Mach stem formation and triple-point path gave excellent agreement with the data.

ACKNOWLEDGMENTS

I am indebted to Dr. Guy Barasch and Dr. John Zinn: Guy for providing me with this thesis project and the opportunity to work on it at Los Alamos under a NORCUS fellowship, and John for the technical direction he provided and the many hours he spent helping me with the writing. I am very thankful for help from Dr. Sidney Stone during the experimental phase. I thank Dr. Rodney Whitaker for information regarding Appendix C, Dr. H. Grady Hughes for information regarding the scaling laws, and John Kodis for running the two-dimensional computer code. I thank all of the above, and Dr. Henry Horak and Dr. Herman Hoerlin, for many useful discussions. I am also grateful for the advice and training given me by Dr. Roy Garstang, Dr. John Cooper, and Dr. Earl Mossberg during my years at graduate school. A special thanks to Jan Stelzer and Luella Button for many helpful editorial comments concerning the writing, and again to Lue for her expert preparation of this thesis. Finally, I cannot express my appreciation to or thank enough my mother Virginia Wilke, my wife Deborah, and my son Jason for their sacrifices and for providing me with moral encouragement during my undergraduate and graduate years.

BIBLIOGRAPHY

Alpher, R. A., and White, D. R., "Optical Refractivity of High-Temperature Gases, I. Effects Resulting from Dissociation of Diatomic Gases," Phys. of Fluids, 2 (1959), p. 153.

Avedisova, V. S., "Formation of Nebulae by Wolf-Rayet Stars," Sov. Astr., 15 (1972), p. 708.

Baker, W. E. Explosions in Air, Austin Texas, University of Texas Press, 1973.

Basov, N. G., Gamaly, E. G., Krokhin, O. N., Mikhailov, Yu. A., Sklizkov, G. V., and Fedotov, S. I., "Investigation of Plasma Parameters at the Spherical Heating of the Isolated Solid Target by High-Power Laser Radiation," in Laser Interaction and Related Plasma Phenomena (edited by Schwarz & Horn), Vol. 3b, New York, Plenum Press (1973), p. 553.

Basov, N. G., Krokhin, O. N., Sklizkov, G. V., and Fedotov, S. I., "Plasma Heating and Neutron Generation Resulting from Spherical Irradiation of a Target with High-Power Laser Radiation," in Lasers and Their Applications (edited by Basov), Vol. 76, Proc. of P. N. Lebedev Inst., Consultants Bureau, New York (1976), p. 145.

Ben-Dor, G., "Regions and Transitions of Nonstationary Oblique Shock-Wave Diffractions in Perfect and Imperfect Gases," University of Toronto Institute of Aerospace Studies (UTIAS) report No. 232, CN ISSN 0082-5255 (1978).

Bennett, B. I., Johnson, J. D., Kerley, G. I., and Rood, G. T., "Recent Developments in the Sesame Equation-of-State Library," Los Alamos Scientific Laboratory report LA-7130 (February 1978).

Bethe, H. A., "Blast Wave," Los Alamos Scientific Laboratory report LA-2000; TID-4500, 13th ed. (1958), Chapt. 4.

Bevington, P. R., Data Reduction and Error Analysis for the Physical Sciences, New York, McGraw-Hill (1969).

Booth, L. A., Freiwald, D. A., Frank, T. G., and Finch, F. T., "Prospects of Generating Power with Laser-Driven Fusion," Proc. of the IEEE, 64, (1976), p. 1460.

Box, G. E. P., and Muller, M. E., "A Note on the Generation of Random Normal Deviates," Annals of Math. Stat., 29 (1958), p. 610.

Chandler, J. P., Computer Science Dept., Oklahoma State Univ., Stillwater, Oklahoma 74074, Program STEPIT, Version 7.4, available from Quant. Chem. Prog. Exchange, Dept. of Chemistry, Indiana University, Bloomington, Indiana (1975).

Dabora, E. K., "Variable Energy Blast Waves," AIAA Journ., 10 (1972), p. 1384.

Dewey, J. M., McMillin, D. J., and Classen, D. F., "Photogrammetry of Spherical Shocks Reflected from Real and Ideal Surfaces," J. Fluid Mech., 81 (1977), p. 701.

Director, M. N., An Investigation of Variable Energy Blast Waves, Ph.D. Thesis, Univ. of Connecticut (1975), Univ. Microfilms Int., Ann Arbor, Mich.

Edwards, A., Ferriter, N., Fleck, J. A. Jr., and Winslow, A. M., "Theoretical Description of the Interaction of a Pulsed Laser and a Target in an Air Environment," Lawrence Livermore Laboratory report UCRL-51489 (1973).

Fan, L. S. and Squire, W., "Inversion of Abel's Integral Equation by a Direct Method," Comp. Phys. Com. 10 (1975), p. 98.

Forsythe, W. E., Smithsonian Physical Tables, 9th Rev. Edition, Smithsonian Institute Publication 4169 (1956).

Freeman, R. A., "Variable-Energy Blast Waves," Brit. J. Appl. Phys. (J. Phys. D), 1 (1968), p. 1697.

Freiwald, D. A., and Axford, R. A., "Approximate Spherical Blast Theory Including Source Mass," J. Appl. Phys. 46, No. 3 (1975), p. 1171.

Fuchs, K., Blast Wave, Vol. 7, Part II, Chapt. 6 (edited by H. A. Bethe), Los Alamos Scientific Laboratory report LA-1021 (1947).

Gilmore, F. R., Equilibrium Composition and Thermodynamic Properties of Air to 24,000 K, RAND report RM-1543, ASTIA Document Number AD 84052 (1955).

Gilmore, F. R., Thermal Radiation Phenomena Vol. I: The Equilibrium Thermodynamic Properties of High Temperature Air, Lockheed Palo Alto Research Laboratory report DASA 1917-1, LMSC-3-27-67-1 (1967).

Glasstone, S., The Effects of Nuclear Weapons, U.S. Atomic Energy Commission (1962).

Gorenflo, R., and Kovetz, Y., "Solution of an Abel-Type Integral Equation in the Presence of Noise by Quadratic Programming," Numerische Math. 8 (1966), p. 392.

Griem, H. R., Stark Broadening of Isolated Spectral Lines in a Plasma, NRL report 6084 (1964).

Griem, H. R., "Semiempirical Formulas for the Electron-Impact Widths and Shifts of Isolated Ion Lines in Plasmas," Phys. Rev. 165 (1968), p. 258.

Guenther, A. H., Pendleton, W. K., Smith, C., Skeen, C. H., and Zivi, S., "Pulsed Interferometric Holography of Laser-Produced Air Breakdown," Opt. Laser Tech. (February 1973), p. 20.

Hall, R. B., "Laser Production of Blast Waves in Low-Pressure Gases," J. Appl. Phys. 40 (1969), p. 1941.

Harlow, F. H., and Amsden, A. A., "Fluid Dynamics, A LASL Monograph," Los Alamos Scientific Laboratory report LA-4700 UC-34 (1971).

Hey, J. D., "Estimates of Stark Broadening of Nitrogen Ion Lines," J. Quant. Spect. Rad. Trans. 16 (1976), p. 575.

Hey, J. D., and Bryan, R. J., "Estimates of Stark Broadening of Oxygen Ion Lines," J. Quant. Spect. Rad. Trans. 17 (1977), p. 221.

Hirt, C. W., Amsden, A. A., and Cook, J. L., "An Arbitrary Lagrangian-Eulerian Computing Method for all Flow Speeds," J. Comp. Phys. 14 (1974), p. 227.

Horak, H. G., Jones, E. M., Kodis, J. W., and Sandford, M. T. II, "An Algorithm for the Discrete Rezoning of Lagrangian Meshes," J. Comp. Phys. 26 (1978), p. 277.

Hugenschmidt, M. and Vollrath, A. K., "Interferometry of Rapidly Varying Phase Objects Using the Fundamental and the Harmonic Wavelengths of a Ruby Laser," 9th Int. Cong. on High-Speed Phot., Denver, CO (1970).

Hughes, T. P., Plasmas and Laser Light, John Wiley and Sons, New York (1975).

Jahoda, F. C., and Seimon, R. E., "Holographic Interferometry Cookbook," Los Alamos Scientific Laboratory report LA-5058-MS (1972).

Lampis, G., and Brown, C., "Afterglow Measurements of a Laser Breakdown Plasma," Phys. of Fluids 11 (1968), p. 1137.

Lathrop, K. D., and Brinkley, F. W., "TWOTRAN-II: An Interfaced, Exportable Version of the TWOTRAN Code for Two-Dimensional Transport," Los Alamos Scientific Laboratory report LA-4848-MS (1973).

Leonard, T. A., and Hammerling, P., "Spherical Shock Development Near Laser-Heated Microshell Targets," to be published.

Leonard, T. A., and Mayer, F. J., "Helium Blast-Wave Measurements of Laser-Heated Microshell Targets," J. Appl. Phys. 46 (1975), p. 3562.

McCall, G. H., "High-Speed Inexpensive Photodiode Assembly," Rev. Sci. Inst. 43, (1972), p. 865.

Minerbo, G. N., and Levy, M. E., "Inversion of Abel's Integral Equation by Means of Orthogonal Polynomials," Siam. J. Numer. Anal. 6, (1969), p. 598.

Molmud, P., "Expansion of a Rarefied Gas Cloud into a Vacuum," Phys. of Fluids 3 (1960), p. 362.

Moore, C. E., "Atomic Energy Level as Derived from the Analyses of Optical Spectra," NSRDS-NBS 35, Vol. I (1971).

Mukherjee, P. K., and Moitra, R. K., "Coupled Hartree-Fock Calculations of the Dynamic Polarizabilities of the Beryllium Sequence," J. Phys. B: Atom. Molec. Phys. 11 (1978), p. 2813.

Nesbet, R. K., "Atomic Polarizabilities for Ground and Excited States of C, N, and O," Phys. Rev. A 16 (1977), p. 1.

Pikalov, V. V., and Preobrazhenskii, N. G., "Abel Transformation in the Interferometric Holography of a Point Explosion," Fiz. Gor. Vzryva (transl.) 10 (1974), p. 923.

Pressley, R. J., Handbook of Lasers with Selected Data on Optical Technology, Chemical Rubber Co., Cleveland, OH (1971).

Ramsden, S. A., and Savic, P., "A Radiative Detonation Model for the Development of a Laser-Induced Spark in Air," Nature 203 (1964), p. 1217.

Reinsch, C. H., "Smoothing by Spline Functions," Numerische Mathematik 10 (1967), p. 177.

Sandford, M. T. II, Anderson, R. C., Horak, H. G., and Kodis, J. W., "Improved, Implicit Radiation Hydrodynamics," J. Comp. Phys. 19 (1975), p. 280.

Sedov, L. I., Similarity and Dimensional Methods in Mechanics, (M. Holt, Ed.), New York, Academic Press (1959).

Taylor, G., "The Formation of a Blast Wave by a Very Intense Explosion: I. Theoretical Discussion," Proc. Roy. Soc. 201 (1950), p. 159.

Taylor, G. I., "The Air Wave Surrounding an Expanding Sphere," Proc. Roy. Soc. 186 (1946), p. 273.

Thorne, A. P., Spectrophysics, Chapman and Hall & Science Paperbacks, London (1974).

von Neumann, J., and Richtmyer, R. D., "A Method for the Numerical Calculation of Hydrodynamic Shocks," J. Appl. Phys. 21 (1950), p. 232.

Weaver, R., McCray, R., Castor, J., Shapiro, P., Moore, R., "Interstellar Bubbles. II. Structure and Evolution," Ap. J., 218 (1977), p. 377.

Werner, H. J., and Meyer, W, "Finite Perturbation Calculations for the Static Dipole Polarizabilities of the First-Row Atoms," Phys. Rev. A, 13 (1976), p. 13.

Wiese, W. L., Smith, M. W., and Glennon, B. M., Atomic Transition Probabilities, Vol. I, NSRDS-NBS4 (1966).

Wilke, M. D., and Stone, S. N., "Optical Diagnostic System for Observation of Laser Produced Shock Waves," SPIE Vol. 190 (LASL Optics Conference) (1979).

Zel'dovich, Ya. B., and Raizer, Yu. P., Physics of Shock Waves and High-Temperature Hydrodynamic Phenomena (Hayes and Probstein, Eds.), Academic Press, New York (1967).

Zinn, J. "A Finite Difference Scheme for Time-Dependent Spherical Radiation Hydrodynamics Problems," J. Comp. Phys. 13 (1973), p. 569.

Zinn, J., and Anderson, R. C., "Structure and Luminosity of Strong Shock Waves in Air," Phys. of Fluids 16 (1973), p. 1639.

Zinn, J., and Sutherland, C. D., "Chemical Equilibria in Hot Air with Moisture, Salt, and Vaporized Metal Contaminants," Los Alamos Scientific Laboratory report LA-5850-MS (February 1975).

APPENDIX A

INTERFEROMETER DESIGN CONSIDERATIONS AND QUALITATIVE SHADOWGRAPHY EVALUATION

Interferometer Design

When analyzing interferograms, it is generally assumed that effects depending on the gradient of the index of refraction are negligible. This is a good approximation when the lens system of the receiving optics places the virtual plane of the recording medium (film in this case) at the center of the region of variable index of refraction as is done in this experiment. When the receiving optics are located at large distances from the disturbed region and are of limited aperture, it is necessary to consider possible problems introduced by Schlieren effects. Although lenses L1 and L2 (see Fig. I-1a) focus the disturbed region on the photographic plates and minimize distortion of the interferograms, if any optical component between the target and film vignettes the refracted beam, an unexposed area will result and data will be lost. The following computer analysis was performed to choose components large enough to avoid this.

The region of variable index of refraction is assumed to be at least cylindrically symmetric. Fig. A-1a illustrates the geometry of rays in the central symmetry plane. The incoming beam of the interferometer is assumed to be parallel and propagates along the

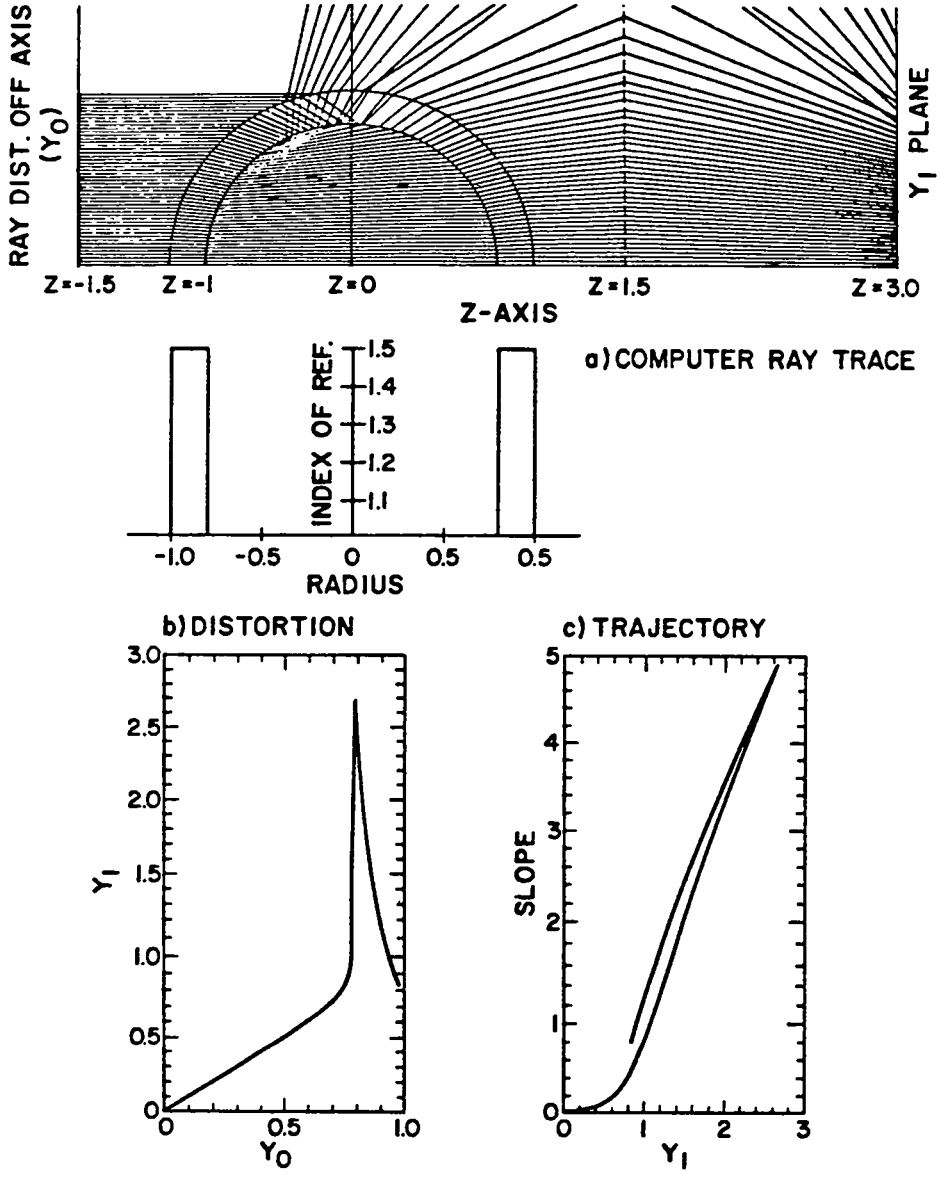

Fig. A-1. (a) Computer ray trace scheme applied to a hollow glass cylinder, with resulting (b) distribution and (c) ray trajectory.

z-axis. A ray originally at position y_o in the y-z plane at $z = -1.5$ is propagated in constant increments of length $|d\vec{s}|$, initially in the z direction. The cylindrically symmetric variable index is represented by $n(r)$, which may or may not have a continuous first derivative. Here, $r^2 = z^2 + y^2$. Upon encountering a change in the index from n_1 to n_2, the ray is refracted by holding $n \sin \theta$ constant. That is, by Snell's law,

$$n_1 \frac{d\ell_1}{|d\vec{s}|} = n_2 \frac{d\ell_2}{|d\vec{s}|} , \qquad \text{(A-1)}$$

where $d\ell$ is the projection of $d\vec{s}$ along a line perpendicular to ∇n in the y-z plane, and $d\ell/|d\vec{s}| = \sin \theta$. After checking for complete internal reflection, Eq. (A-1) is used to calculate $d\ell_2$ and a new $d\vec{s}$. This is repeated until the ray has propagated the desired distance. Two computer arrays of y and z keep track of the history of the ray's progress.

In Fig. A-1a, the region of variable index is normalized so that its maximum radius is 1. Once the ray passes through the variable region and strikes a plane at $z = 1.5$, its direction, $d\vec{s}$, is changed by setting $d\vec{z} = d\vec{z}$, and $d\vec{y} = -d\vec{y}$. It then propagates in a straight line to $z = 3.0$. The $z = 1.5$ plane represents a perfect 0.75 focal length lens, and the $z = 3.0$ plane is the equivalent of a film plane. A record of the y-value and negative of the slope at the $z = 3.0$ plane is kept for each ray representing the trajectory. Figure A-1a shows this process applied to a glass tube with $|d\vec{s}|$ taken to be 0.001. Computations with $|d\vec{s}| = 0.0005$ showed no significant difference. Fifty rays were propagated with initial

values of y running evenly from 0.0 to 0.98. The index of refraction for the glass was 1.5, and the ambient medium was assumed to be air at STP. The inner radius of the tube was 0.8.

An estimate of the distortion is obtained by plotting the y-value of the incoming parallel ray (y_0) versus the y-value of the same ray at the z = 3.0 plane (y_1). This is the equivalent position on the film plane for a magnification of 1. The plot is shown in Fig. A-1b. There is little distortion for rays with initial y-values less than 0.75, despite heavy refraction of the beam.

Figure A-1c plots the y-value at the z = 3.0 plane versus the negative slope, s. This plot describes the trajectory of the ray as it leaves the region of variable index. Each exiting ray can be represented by a vector (y_1,s_1), which is transformed as it propagates through the optical system into (y_T,s_T). The transformation of a ray traveling a distance D through a uniform medium is given by matrix Δ. For a simple lens of focal length f, the transformation is L, where

$$\Delta = \begin{pmatrix} 1 & D \\ 0 & 1 \end{pmatrix} \qquad L = \begin{pmatrix} 1 & 0 \\ -1/f & 1 \end{pmatrix} . \qquad \text{(A-2)}$$

The appropriate products of Δ and L can be used to transfer a ray through the optical system. By knowing the aperture of the components, it is possible to tell which rays leaving the object at a given trajectory will be vignetted by comparing the value of y_T at the position of each component with the aperture radius of that component. Figure A-2 is a plot of y_1 vs s_1 showing the effects of

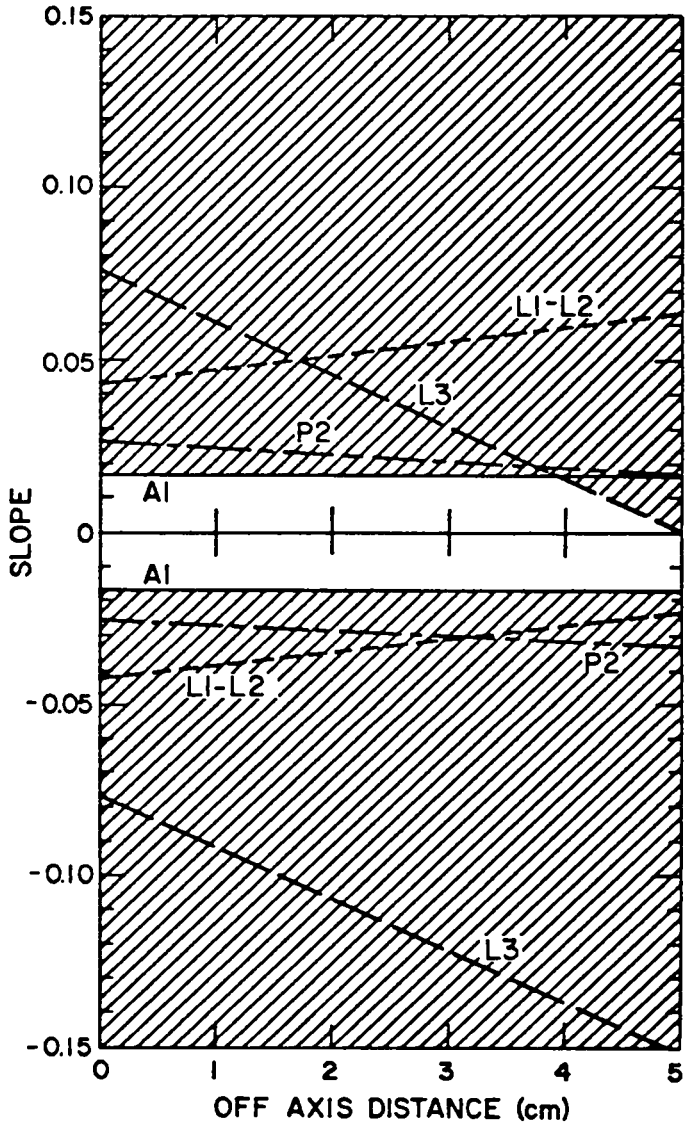

Fig. A-2. Vignetting effect of optical components in Figs. I-1(a) and I-2 on rays with various trajectories leaving the shocked region. Rays with trajectories in the shaded region will not pass through the optical system.

the apertures of the various components labeled in Figs. I-1a and I-2. Any ray with (y_1,s_1) in the shaded region will be vignetted. Lens L3 and aperture A1 are the most constraining components; and, because A1 is at the focal distance from L3, its effect is independent of y_1. A comparison of Figs. A-1c and A-2 shows that only a very small central section of the glass tube would be visible.

To determine the extent that rays passing through a shock-wave image would be vignetted, Taylor's (1950) approximate formula for the density was used:

$$\rho = \rho_0 \exp\left[\ell n \frac{\gamma + 1}{\gamma - 1} + \frac{3}{\gamma - 1} \ell n r - 2 \frac{\gamma + 5}{7 - \gamma} \ell n \frac{\gamma + 1 - r^{h-1}}{\gamma}\right]. \quad \text{(A-3)}$$

Here $0 \leq r \leq 1$ is the fraction of the shock radius, while $h = (7\gamma - 1)/(\gamma^2 - 1)$. A worst-case estimate can be made, using an ambient density $\rho_0 = 1.29 \times 10^{-3}$ g/cm^3 and $\gamma = 1.2$. The index is related to the density by $\eta = 0.2247\rho + 1$. Fifty rays were traced with uniformly distributed initial y-values of 0.95 to 1. and $|d\vec{s}|$ was set to 0.001. The region of 0.95 to 1. produces the greatest refraction, as might be expected.

The results are shown in Figs. A-3a and b. The distortion curve is very straight, with unity slope, indicating that the shock wave image will show little distortion. Fig. A-2 shows that for shocks with radii less than ~ 4 cm, rays leaving the shocked region with slopes of absolute value $\gtrsim$ 0.017 will be vignetted. Fig. A-3b shows that the outer 0.6% of the shock wave deflects the rays so that the slope is less than - 0.017, and therefore rays passing through this region are vignetted.

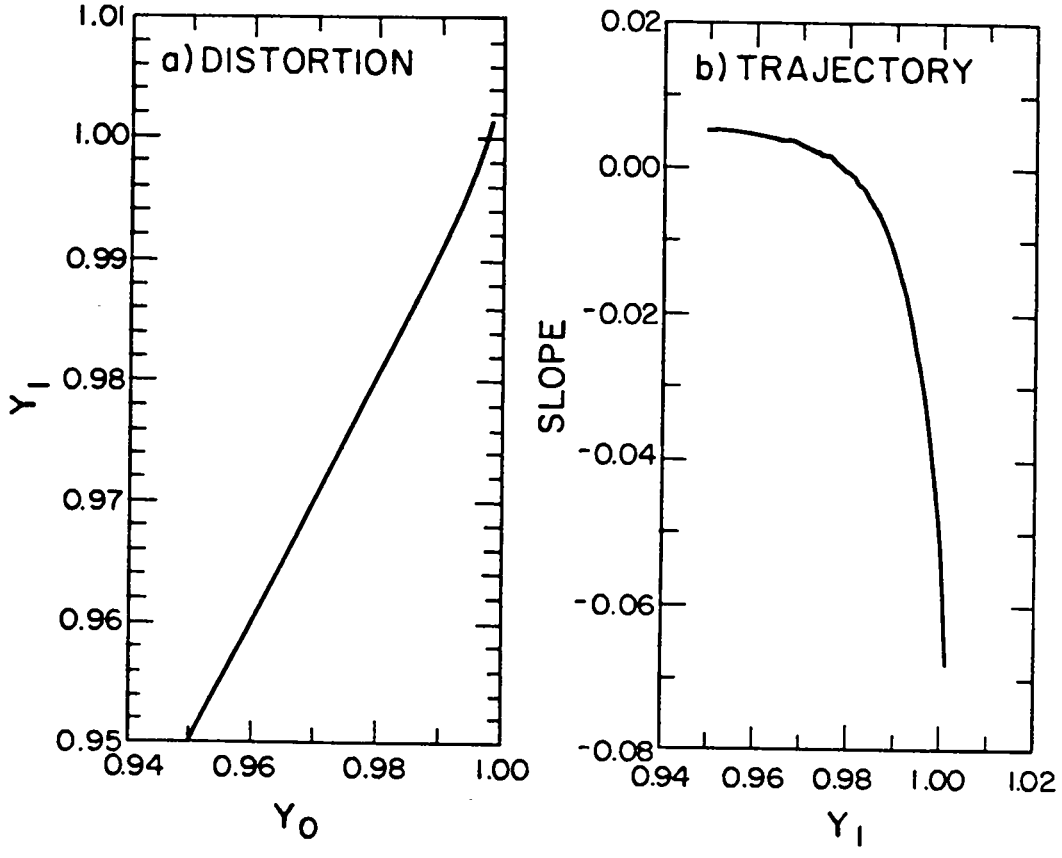

Fig. A-3. (a) Distribution, and (b) trajectory, due to a strong shock wave in $\rho_0 = 1.29 \times 10^{-3}$ g/cm^3 air.

For R_s = 1 cm, the rays passing through the outer 60 μm of the shock would not reach the film plane, and information would be lost. The effect is much less at 50 torr (7.87×10^{-5} g/cm^3) and lower ambient pressures. The resolutions of the 694.3 nm interferograms are 50 to 100 μm. Therefore, the apertures of the optics are sufficiently large to cause no degradation of the interferograms.

Shadowgraphy

The numerical method just described can be extended to generate shadowgraphs for comparison with the data. The rays are again propagated through the shock-density profile given by Eq. (A-3). The trajectories of the rays exiting from the plasma are obtained in the same manner that they were in the previous section. Each ray is transported through the shadowgraphy optical system. The y-position of the ray is checked as it passes through each component and propagation is discontinued if the ray is vignetted. The film is represented by an array of 100 "bins" evenly spaced from r = 0 to the edge of the field of view. The field-of-view radius was taken as 1.5 cm. The final position of each ray is multiplied by a constant so an opaque disc 1 cm in radius at the shock center would yield a shadow on the image 1 cm in radius. A one is added to the bin corresponding to the position where the ray strikes the film.

As $\gamma \to 1$, the shock becomes increasingly more like a thin shell (see Appendix C). Comparison with the glass-tube example shows that a shell would act as a negative lens. As γ increases, the shock

behaves less as a negative lens, and eventually has a net positive focusing effect.

Figure A-4a shows two computer-generated shadowgraph-exposure profiles for shocks in 50-torr air. Equation (A-3) was used to calculate the shock densities with γ = 1.2 and 1.4. Five thousand rays with equally spaced initial radii from 0.0 to 1.5 cm were traced to produce a background "exposure" of 50 per bin. The shock profile with γ = 1.2 has a negative focusing effect that results in a heavier-than-background exposure at the edge. Negative focusing makes the scaled image appear larger than the shock. For γ = 1.4, the shock has a net positive focusing effect, and the image has the correct dimensions. The edge in this case has a weaker-than-background exposure.

We now compare computer-generated and experimental shadowgraphs. The third frame of the shadowgraphy set in Fig. II-1 was scanned along a diameter with a densitometer. The densities were converted to relative exposures using step-wedge data. The exposures were normalized by setting the background exposure equal to those of the computer-generated shadowgraph. The outer radius was normalized to 1 for comparison with computed profiles. A plot of the data is given in Fig. A-4b. The time of the exposure is 8.5 μs. This is in the regime of self-similar expansion (1 to 10 μs). Interferometry data (Chapt. III) and computer calculations (Chapt. V), however, show that the peak density has already fallen below the value given by the strong-shock Hugoniot relation $\rho_s = \rho_0[(\gamma + 1)/(\gamma - 1)] = 6\rho_0$ with γ = 1.4. The numerical calculation yields $\rho_s/\rho_0 \simeq 3$. The data tend to confirm a weaker shock profile,

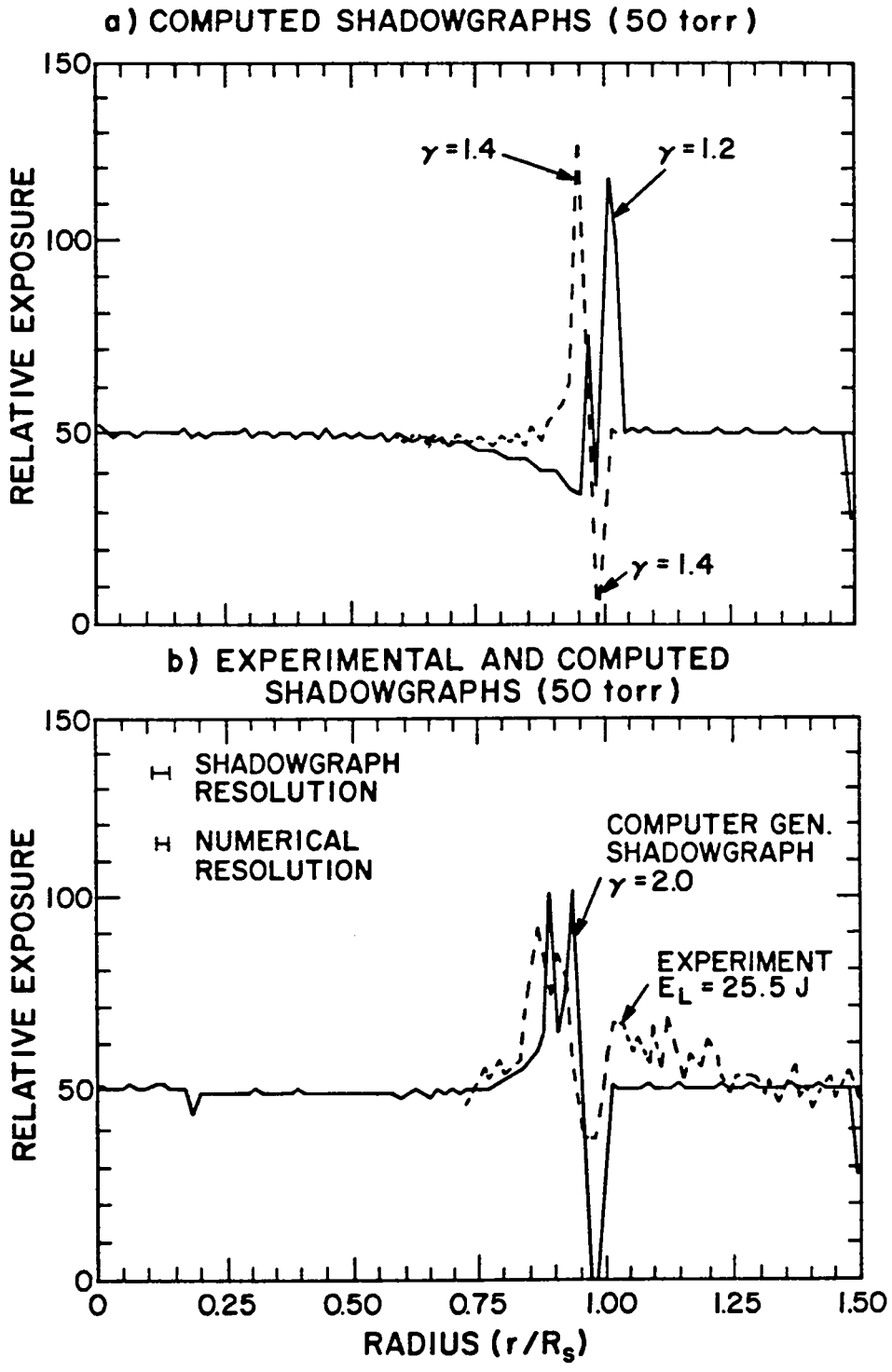

Fig. A-4. (a) Computer-generated shadowgraphs of shock waves in 50-torr air, assuming γ = 1.4 and 1.2.

(b) Comparison of computer-generated shadowgraph with experimental shadowgraph profile.

evidenced by a broader region of low exposure at the shock edge than that given by the computer-generated shadowgraph for $\gamma = 1.4$. Equation (A-3) is not valid for weak shocks. However, it can be used to generate an approximate profile by assuming an artificially large value of γ to produce the correct ρ_s/ρ_o. If $\gamma = 2$ is used, then $\rho_s/\rho_o = 3$. A computer-generated shadowgraph with $\gamma = 2$ is plotted in Fig. A-4b. The qualitative comparison is good, including the double exposure-maxima.

Two points are clear from this qualitative analysis of the shadowgraphs. The shadowgraphs can be used for radius measurements if the outer edge of the shock image shows a below-background exposure. The shadowgraphs provide a qualitative estimate of the shock strength, but cannot be easily used to obtain quantitative density profiles.

APPENDIX B

ABEL INVERSION FOR INTERFEROGRAMS

Digitizing the fringe pattern results in a set of array pairs. One member of the pair consists of N non-evenly spaced r_z values in strictly increasing order; the other contains the N corresponding fringe-shift values measured at each r_z. The radius r_z is the distance of the point of measurement from the center of the circular image of the spherical shocks. The object is to obtain a representation of g(r) from the data and Eqs. (III-13) and (-12). Several direct and indirect methods exist for doing this [see references in Minerbo and Levy (1969)]. I used a direct method, first fitting the data with a smoothing spline algorithm [Reinsch (1967)] and then integrating Eq. (III-13). The method is straightforward and the fitting routine can just as well be applied to a calculated g(r). Equation (III-11) can be integrated to yield a fringe-shift profile for comparison with the digitized data. The method has the disadvantage that estimating the error in the result is difficult, and determination of the amount of smoothing that yields the best result is a qualitative process.

Spline fitting has previously been used to invert Abel's equation [Fan and Squire (1975)]. The splines were used to interpolate between discrete points and no smoothing was provided. The results were very good for exact points, but the technique is unsuitable for real data due to the noise amplification produced by Eq. (III-13). Gorenflo and Kovetz (1966) showed that the noise amplification for one approximate inversion method with no smoothing is proportional

to the number of data points. Fan and Squire also trapezoidally integrated the spline fit to Eq. (III-13), instead of taking advantage of the functional form of the cubic spline equation, as is done here.

The N fringe-shift measurements made along a fringe at positions $r_{z1}, r_{z2}, \ldots r_{zN}$ are represented by $f_i = f(r_{zi})$. Application of Reinsch's smoothing algorithm results in a set of cubic splines

$$u(r_z) = u_i = a_i + b_i p_i + c_i p_i^2 + d_i p_i^3 \quad , \tag{B-1}$$

where $p_i = r_z - r_{zi}$ when $r_{zi} \leq r_z < r_{zi+1}$. Cubic splines have the property that u, u', and u" are continuous at the r_{zi}, and $u'''(r_z)_i = 0$. A further boundary specification is supplied by $f''_{1-} = f'''_{1-} = f''_{N+} = f'''_{N+} = 0$. Reinsch's splines meet the constraints of minimizing the quantity

$$\int_{r_{z1}}^{r_{zN}} u''(r_z)dr_z \quad , \tag{B-2}$$

while at the same time satisfying

$$\sum_{i=1}^{N} \left(\frac{u(r_{zi}) - f_i}{\delta f_i} \right)^2 \leq S \quad . \tag{B-3}$$

$S \geq 0$ determines the degree of smoothing, and there is no smoothing if $S = 0$. The $\delta f_i \geq 0$ are arbitrary weights for the f_i. If δf_i is an estimate of the standard deviation of f_i, natural values of S are within the confidence interval corresponding to the left-hand side of Eq. (B-3), that is

$$N - (2N)^{1/2} \leq S \leq N + (2N)^{1/2} \quad . \tag{B-4}$$

For the problem at hand--i.e., inversion of the Abel equation--replacing $f'(r_z)$ in Eq. (III-13) with the derivative of $u(r_z)$ yields

$$g(r_j) = -\frac{1}{\pi} \sum_{i=j}^{N-1} \int_{r_{zi}}^{r_{zi+1}} \frac{u'_i}{\sqrt{r_z^2 - r^2}} \, dr_z \quad , \tag{B-5}$$

where $r_j \equiv r_{zj}$ and $r_{zN} = R_s$ (the shock radius). Integrating the explicit representation of u'_i from Eq. (B-1) gives

$$g(r_j) = -\frac{1}{\pi} \sum_{i=j}^{N-1} \Bigg\{ [b_i - 2c_i r_{zi} + 3d_i r_{zi}^2][\ell n(r_z + \sqrt{r_z^2 - r_j^2})]$$

$$+ [2c_i - 6d_i r_{zi}] \sqrt{r_z^2 - r_j^2} + 3d_i \Bigg[\frac{r_z}{2} \sqrt{r_z^2 - r_j^2}$$

$$+ \frac{r_z^2}{2} \ell n(r_z + \sqrt{r_z^2 - r_j^2}) \Bigg] \Bigg\} \Bigg|_{r_z = r_{zi}}^{r_z = r_{zi+1}} \quad . \tag{B-6}$$

For $r_1 \simeq 0$, $g(0)$ can be extrapolated using the even function

$$g(r) = \alpha + \beta r^2 + \gamma r^4 \quad , \tag{B-7}$$

where α, β, and γ are determined from $g(r_1)$, $g(r_2)$, and $g(r_3)$.

It is sometimes useful to generate a fringe profile that would result from an analytically calculated density distribution for comparison with measured fringe profiles. In this case, g(r) is known and can be fit using the Reinsch algorithm. Then, by Eqs. (III-11) and (B-1), $f(r_{zj})$ is given by

$$f(r_{zj}) = 2 \sum_{i=j}^{N-1} \left\{ (A_i + C_i r_{zj}^2) \cdot P_j + (B_i + \frac{3 r_{zj}^2 D_i}{4}) \right.$$

$$\left. \cdot [\frac{r}{2} P_j + \frac{r_{zj}^2}{2} \ell n(r + P_j)] + \frac{C_i}{3} P_j^3 + \frac{D_i r^3}{4} P_j \right\} \Bigg|_{r=r_i}^{r=r_{i+1}} , \quad \text{(B-8)}$$

with

$$\begin{aligned} A_i &= a_i - b_i r_i + c_i r_i^2 - d_i r_i^3 \\ B_i &= b_i - 2c_i r_i + 3d_i r_i^2 \\ C_i &= c_i - 3d_i r_i \\ D_i &= d_i \\ P_j &= \sqrt{r^2 - r_{zj}^2} \end{aligned} \quad \text{(B-9)}$$

Comparison with Existing Methods

The first test of the spline technique was a comparison with a published method [Minerbo and Levy (1969)] that has compared favorably with other methods.

The test curves and their analytic inverses considered by Minerbo and Levy were

Curve A

$$f(r_z) = -\frac{2}{3}\left(\frac{1}{4} - r_z^2\right)^{1/2}(1 + 8r_z^2) + \frac{4}{3}(1 - r_z^2)^{1/2}(1 + 2r_z^2)$$

$$-4r_z^2 \log \frac{1 + (1 - r_z^2)^{1/2}}{\frac{1}{2} + \left(\frac{1}{4} - r_z^2\right)^{1/2}} \quad , \; 0 \leqq r_z \leqq 1/2 \qquad \text{(B-10)}$$

$$f(r_z) = \frac{4}{3}(1 - r_z^2)^{\frac{1}{2}}(1 + 2r_z^2) - 4r_z^2 \log \frac{1 + (1 - r_z^2)^{\frac{1}{2}}}{r_z} \quad , \; \frac{1}{2} \leqq r_z \leqq 1$$

$$g(r) = \begin{cases} 1 - 2r^2, & 0 \leqq r \leqq 1/2 \\ \\ 2(1 - r)^2, & 1/2 \leqq r \leqq 1 \end{cases} \quad . \qquad \text{(B-11)}$$

Curve B ($\beta = 1.1$)

$$f(r_z) = \frac{\sqrt{\pi}}{\beta}(1 - r_z^2)^{-1/2} \exp\left[\beta^2\left(1 - \frac{1}{1 - r_z^2}\right)\right] \qquad \text{(B-12)}$$

$$g(r) = (1 - r^2)^{-3/2} \exp\left[\beta^2\left(1 - \frac{1}{1 - r^2}\right)\right] \qquad \text{(B-13)}$$

Minerbo and Levy first considered the "absolute accuracy" of several methods as applied to these curves. They used values of $f(r_z)$ calculated at 21 values of r_z; namely, $r_z = 0.00, 0.05, 0.10, \ldots, 1.0$ using Eqs. (B-10) and (B-12) without a noise component. Then they applied various methods, in addition to their own, to calculate $g(r)$ from $f(r_z)$ and compared the results with the $g(r)$ calculated from Eqs. (B-11) and (B-13).

To test the spline-fit inversion technique, I followed the same procedure. The smoothing parameter S was set to zero (S = 0 gave the best results). The standard deviation (σ_g) between the inverted and calculated g for the spline technique and the standard deviations for the methods tested by Minerbo and Levy are given in Table B-I. The spline fit for curve A was comparable in overall accuracy to the Minerbo-Levy method and superior in the case of curve B. The spline method gave poorest accuracy over $0.0 \leq r_z \leq 0.1$, where it was about five times worse than the Minerbo-Levy method. However, it was 10 to 100 times more accurate over the rest of the curve.

Minerbo and Levy tested their method against random errors by rounding the calculated $f(r_z)$ to two decimal places, corresponding ideally to a standard deviation in f of $\sigma_f \simeq 0.00289$. The actual values were $\sigma_f = 0.00278$ for curve A and 0.00293 for curve B. The mesh was identical to that used in the accuracy test. The δf_i were arbitrarily set equal to 0.00289 in the spline-fitting procedure. If this was a correct value for the δf_i, Eq. (B-4) predicts that $S = 21 \pm 6$ would give the best fit to the exact f, because the number of data points is 21. Figs. B-1a and b are plots of σ_f-vs-S and σ_g-vs-S for curves A and B, respectively. The minimum values of

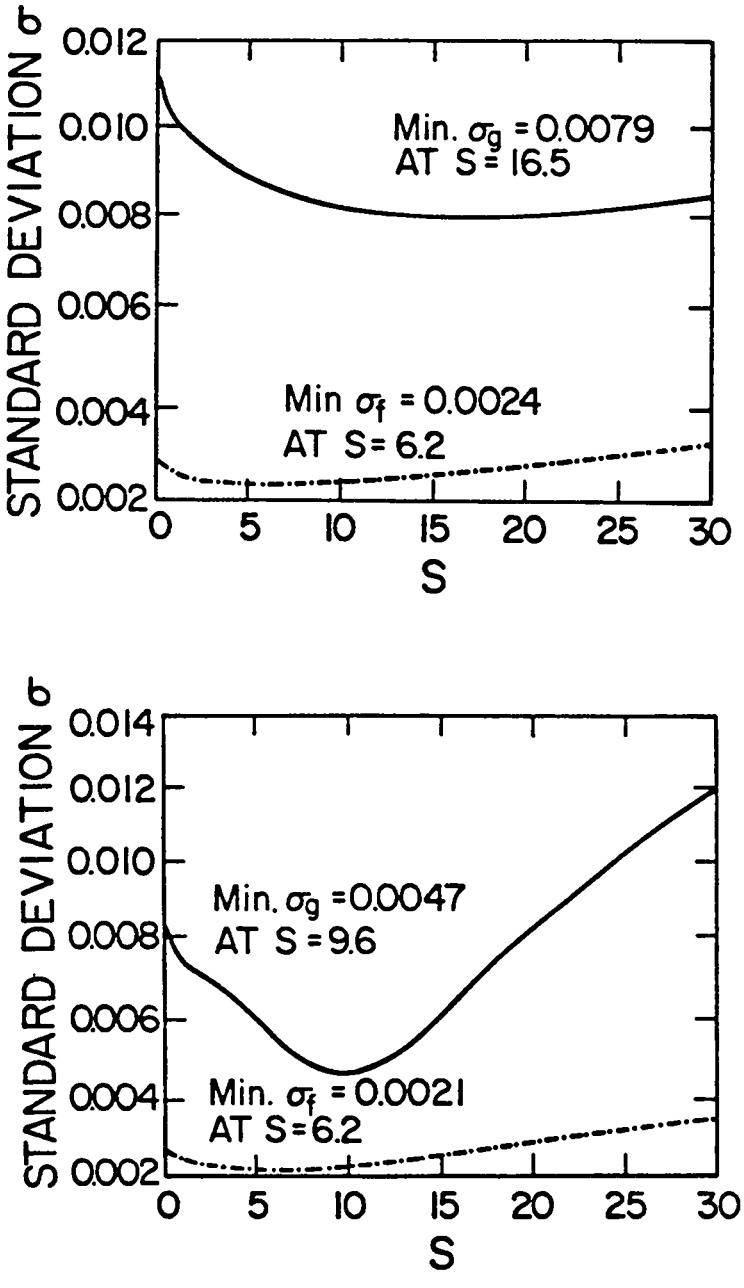

Fig. B-1. Standard deviation between the input function with rounding error and the exact input function (σ_f), and between the resulting inverted function and the exact inverted function (σ_g), vs the smoothing parameter S for (a) curve A and (b) curve B.

σ_g and the corresponding S values are given on the plots. The optimum Minerbo and Levy values are σ_g (curve A) = 0.0026 and (curve B) = 0.0053. The spline technique gives comparable results to Minerbo and Levy's method for the two cases discussed.

Minerbo and Levy's method has an advantage over other methods in that it is possible to estimate statistically when an increase in the number of polynomials used to describe the solution no longer significantly improves the accuracy of the result and may be detrimental to the accuracy. It is not clear in the case of very noisy data if this estimate for the number of polynomials would result in a more accurate g than an estimate made by simply eyeing the fit.

Test Using Simulated Data

The fringe-shift data resulting from the digitization process described in Chapter III have several distinguishing characteristics. The g(r) obtained from inverting the data is strongly peaked at $r \simeq R_s$. The data points are taken at approximately uniform increments of distance along the fringe, rather than uniformly along r_z. For the simulation it will be assumed that the points have a distribution about the center of the fringe determined along a line perpendicular to the background fringe (perpendicular to the r_z axis). There is a tendency to trace the fringe along the center measured perpendicular to the disturbed-fringe direction, resulting in a systematic error near the shock boundary. However, this error has been estimated to be small. There is also a systematic error in the r_z values due to the conversion from the digitized Cartesian coordinates, to polar radii with the assumption

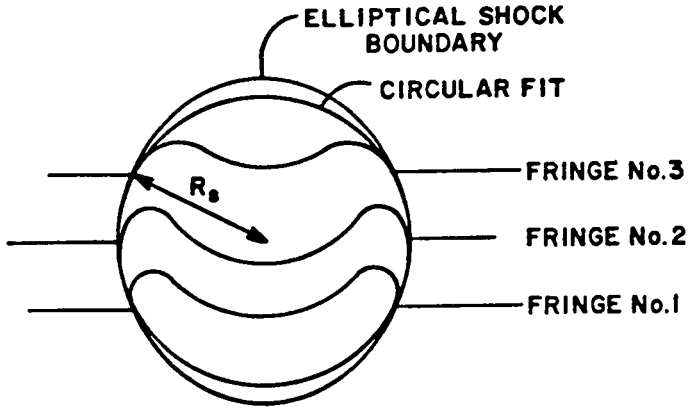

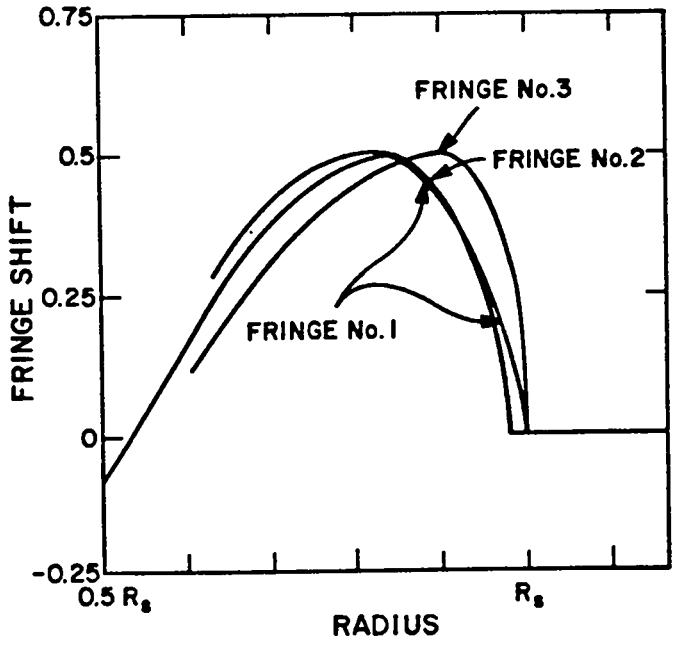

Fig. B-2. Example of the effects of the ellipticity of the shock wave images on the measurement of the fringe shift.

that the shock images are circular. The magnitude of the error depends on the asphericity of the shock profile, as illustrated in the exaggerated example of Figs. B-2a and b.

The shock in Fig. B-2a is elliptical. The four boundary points on Fringes #1 and #3 were fit to a circle of radius R_s; and the calculated location of the center was used to convert the (x,y) coordinates to radial coordinates. Figure B-2b shows a plot of the fringe shift vs radius after the conversion. A critical problem is the variation of slope near R_s, which, by Eq. (III-13), translates into a variation in the peak index of refraction. This problem becomes more severe at early times when the shock is more elliptical; and it is complicated by internal asymmetric structure in the shock profile and by the viewing angle, which is 45^o to the axis of symmetry of the shock (Fig. I-1a). The size of the error can be seen by comparing the unfolded value of the peak index of refraction for fringes above and below the central fringe (Fringes #1 and #3 in Fig. B-2). The central fringe yields the most accurate results. Coordinate conversion by circular fits to the shock profiles, as done here, yields greater accuracy than using the distance from the elliptical shock-profile axis for r_z as has been done in some past works [e.g., Hugenschmidt and Vollrath (1970)].

Figure B-3 shows an approximate curve for $f(r_z)$ resulting from a hypothetical Taylor-von Neumann-Sedov shock wave. The curve was generated using Eq. (A-3) for $\rho(r)$ with $\rho_o = 0.787 \times 10^{-4}$ g/cm^3 (50 torr) and $\gamma = 1.4$. Then, using $n(r) = 0.2247\ \rho(r) + 1.$ and Eq. (III-12) to calculate g(r) with $\lambda = 694.3 \times 10^{-5}$ cm, $f(r_z)$ was calculated numerically using Eq. (B-8) after spline fitting g(r) with S = 0.

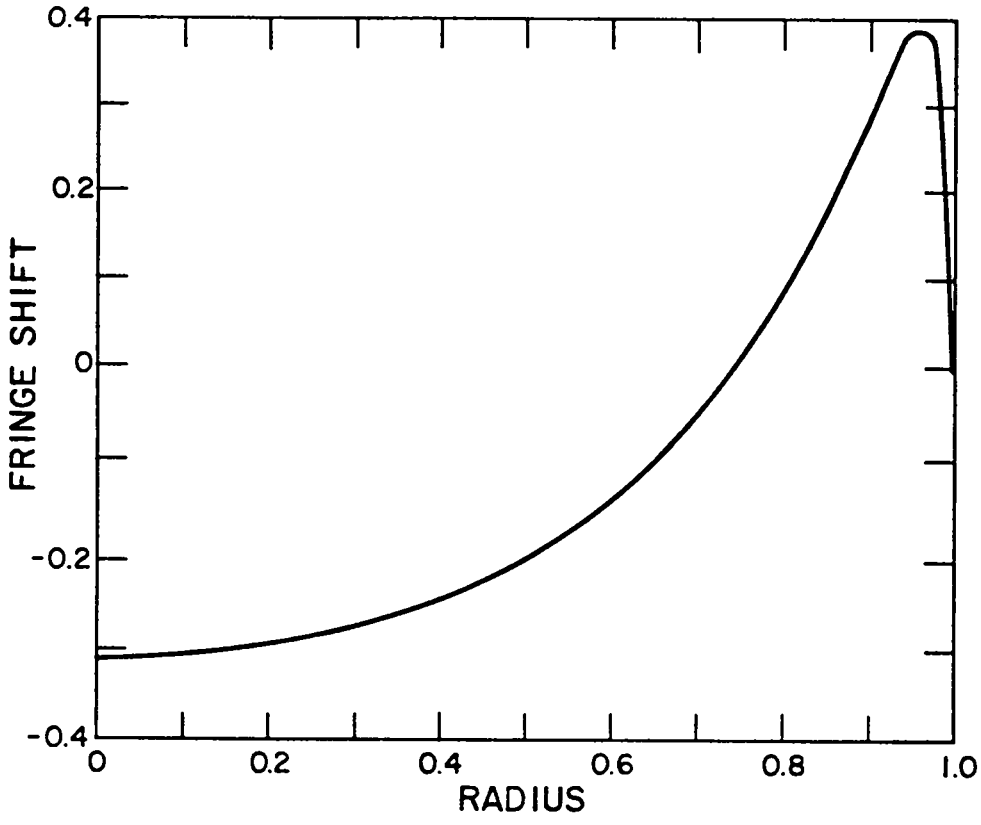

Fig. B-3. Fringe shift as a function of normalized radius which would result from Taylor's approximate density profile.

There is no simple analytical expression for the curve in Fig. B-3, so it is not suitable for simulation of the data. However, curve B [Eq. (B-12)] appears qualitatively similar to the curve in Fig. B-3 if $\beta = 0.3$ is used and Eqs. (B-12) and (B-13) are multiplied by 0.05. The curve for $f(r_z)$ is shown as the solid line in Fig. B-4a, and the corresponding g(r) is shown as the solid line in Fig. B-4b.

Values of $f(r_z)$ were calculated at 101 values over $0. \leq r_z \leq 1$ using Eq. (B-12) multiplied by 0.05 with $\beta = 0.3$. The standard deviation between the exact g(r) and the inverted g(r) (no noise) was $\sigma_g = 0.0011$. The fractional error of the peak value of g(r) was $\varepsilon_p = 0.0005$, where

$$\varepsilon_p = \frac{g(\text{inverted}) - g(\text{calculated})}{g(\text{calculated})} \qquad \text{(B-14)}$$

with the peak g values taken at r = 0.97.

Noise was added to the simulated data points using

$$\bar{f}_i = \bar{f}(r_{zi}) = f(r_{zi}) + N_i \quad . \qquad \text{(B-15)}$$

The N_i are a set of random normal deviates generated with a Box and Muller (1958) algorithm from random numbers evenly distributed over the interval [0,1]. The average of the N_i goes to zero as the number of N_i goes to infinity; the standard deviation of the 101 N_i was set to 0.004. The $\bar{f}_i$ are indicated by the dots in Fig. B-4a.

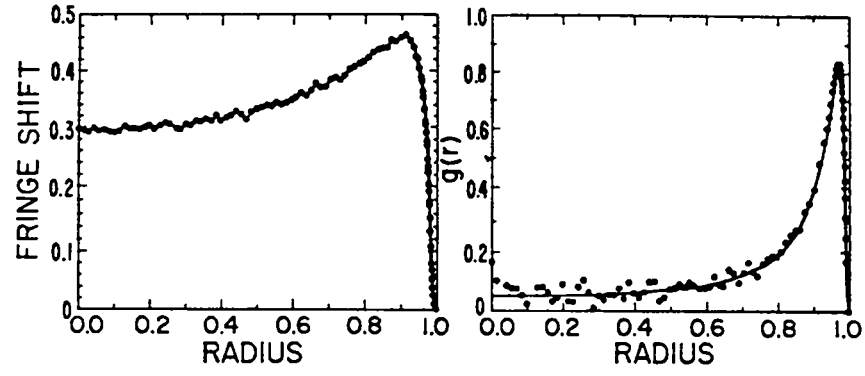

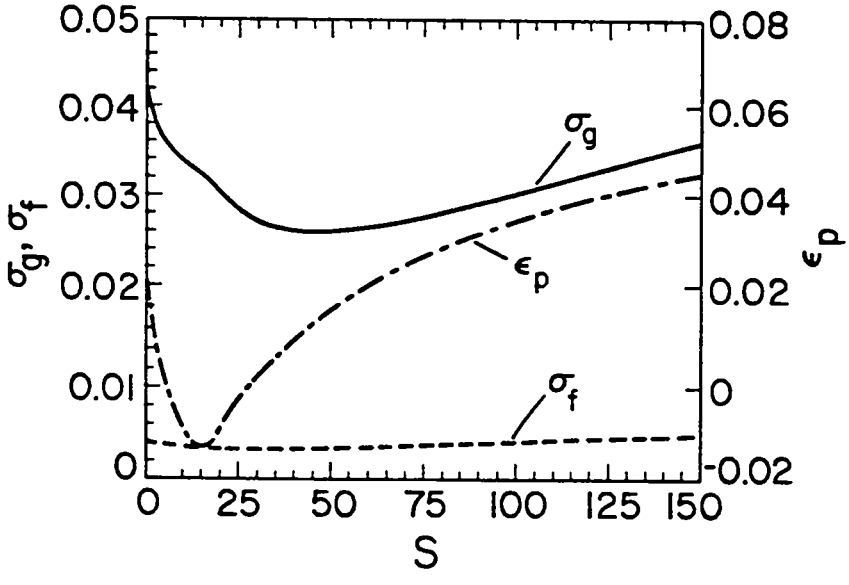

Fig. B-4. (a) Function f of curve B with $\beta = 0.3$ and added random noise with $\sigma = 0.004$.

(b) Comparison of the result of inverting the noisy f with S = 40 (dots) and the exact g (solid line).

(c) Standard deviation in smoothed f (σ_f), inverted f (σ_g), and fractional error between inverted peak value and exact peak value (ϵ_p).

Figure B-4c is a plot of σ_g, σ_f, and ε_p vs S resulting from inversion of the $\bar{f}_i$. The δf_i were set to 0.004. The dots in Fig. B-4b are the inverted data when S = 40.

The variation of σ_g with the number of data points for a given noise level is also of interest. A standard deviation in the N_i of 0.004 was again used and the minimum σ_g was found versus S for several different numbers of data points. The results were: for 11 points, σ_g = 0.035; 21 points, 0.013; 51 points, 0.021; 101 points, 0.026; 201 points, 0.023; and 501 points, 0.026. Twenty points produced a lower σ_g, but this was too few points to resolve the sharp peak in g(r). Fifty points appeared adequate to resolve the peak. It was further found by plotting σ_g and ε_p vs S that for the tests with fifty or more points, ε_p was smaller for a slightly "loose" fit in terms of S.

Several conclusions result. The spline technique produces results for optimum S that are comparable to results of other methods. Digitizing 50 to 100 points across the radius of the shock with a higher density of points per fringe length taken at $r_z \simeq R_s$ will produce the best results for g(r) in terms of overall accuracy and accuracy in g(r) at the peak values. The higher number is used for early shocks where the front is steeper. The fact that there is no formula for choosing S does not matter. It was found that by interactively fitting the data with various values of S, one could choose an S value that gave satisfactory results, and that plotting $f'(r_z)$ was an aid in choosing an optimum S value. Finally, by choosing a value of S that is slightly less than the apparent

optimum value, the general shape of g(r) is still clear and greater accuracy in the peak is more likely.

TABLE B-I

STANDARD DEVIATIONS OF OVERALL FIT FOR SEVERAL METHODS

	From Minerbo and Levy (1969)				
	Nester-Olsen	Borkasten	Maldonado et al.	Minerbo-Levy	Spline Fit
Curve A	0.00517	0.00123	0.00112	0.00110	0.00116
Curve B	0.0118	0.00281	0.00822	0.00078	0.00054

APPENDIX C

BETHE'S SMALL $\gamma - 1$ APPROXIMATION AND FUCHS' SOLUTION INCLUDING SOURCE MASS

Bethe (1958) realized that as $\gamma \to 1$, the Taylor-von Neumann-Sedov self-similar solution of an ideal point explosion shows several simplifying features which make possible the development of approximate solutions of the differential equations for nonideal, extended-source cases. From the strong-shock Hugoniot relation, the density behind the shock front is $\rho_s = \rho_o[(\gamma + 1)/(\gamma - 1)]$, where ρ_o is the density of the surrounding air. Therefore, as $\gamma \to 1$, the density jump across the shock front becomes very large; and the shock structure, which contains most of the mass originally contained in the shock interior, becomes infinitesimally thin. The flow velocity behind the shock, u_s, approaches the shock-wave velocity $\dot{R}_s$ according to the Hugoniot relation

$$u_s = \frac{2}{\gamma + 1} \dot{R}_s \xrightarrow{\gamma \to 1} \dot{R}_s \quad . \tag{C-1}$$

The shock front pressure is given by

$$p_s = \frac{2}{\gamma + 1} \dot{R}_s^2 \rho_o \xrightarrow{\gamma \to 1} \dot{R}_s^2 \rho_o \quad . \tag{C-2}$$

Furthermore, from the self-similar solution, the pressure of the interior, p_i, is approximately uniform and is very nearly half of p_s [see Chernyi's solution in Zel'dovich and Raizer (1966)].

With uniform internal pressure, the internal energy is

$$E_i = \frac{p_i}{\gamma - 1} \frac{4\pi R_s^3}{3} \simeq \frac{0.5\ p_s}{\gamma - 1} \frac{4\pi R_s^3}{3} \quad . \tag{C-3}$$

and the kinetic energy is approximately

$$E_k = \frac{4\pi R_s^3}{3} \rho_o \frac{\dot{R}_s^2}{2} \quad , \tag{C-4}$$

again assuming a thin shell.

Substituting Eq. (C-2) into (C-3) and comparing with (C-4) gives

$$E_k = (\gamma - 1)(\gamma + 1)E_i \xrightarrow{\gamma \to 1} 2(\gamma - 1)E_i \quad . \tag{C-5}$$

The total shock energy, E_s, is mostly internal energy:

$$E_s = E_i + E_k \simeq E_i = \frac{p(0,t)}{\gamma - 1} \frac{4\pi R_s^3}{3} \quad . \tag{C-6}$$

Bethe's "small $\gamma - 1$" approximation [used by Fuchs (1947)] therefore consists of the assumptions that the entire mass of entrained material is in a thin shell at the shock front and the interior pressure is uniform. These assumptions become more valid as $\gamma \to 1$ and are fairly good for very hot air where $\gamma \sim 1.2$.

The equation of motion is obtained by considering an arbitrary shell of constant mass. At time $t = 0$, the shell is at position r (the Lagrangian coordinate) with density $\rho(r)$ and thickness dr. After the passage of the shock, the shell is at position R (the Eulerian coordinate), with density ρ_1 and thickness dR. Conservation of mass implies

$$\rho_1 R^2 dR = \rho r^2 dr \quad , \tag{C-7}$$

giving

$$\frac{\partial R}{\partial r} = \frac{\rho}{\rho_1} \frac{r^2}{R^2} \quad . \tag{C-8}$$

The general equation of motion is

$$\frac{d^2R}{dt^2} = -\frac{1}{\rho_1} \frac{\partial p}{\partial R} = -\frac{R^2}{\rho r^2} \frac{\partial p}{\partial r} \quad , \tag{C-9}$$

where Eq. (C-8) was used to derive the expression on the right. We now use the small $\gamma - 1$ approximation to say that since all the material is at the shock front, $R = R_s$, $\dot{R} = \dot{R}_s$, and $\ddot{R} = \ddot{R}_s$. Substituting and integrating Eq. (C-9) gives

$$p(r,t) = p_s + \frac{\ddot{R}_s}{R_s^2} \int_r^{R_s} \rho(r) r^2 dr \quad . \tag{C-10}$$

At the center ($r = 0$),

$$p(0,t) = p_s + \frac{\ddot{R}_s}{R_s^2} M(R_s) \quad . \tag{C-11}$$

$M(R_s)$, given by

$$M(R_s) = \int_0^{R_s} \rho(r) r^2 dr \quad , \tag{C-12}$$

is the total mass per unit solid angle within the shock.

From $\dot{R}_s = \dot{R}_s(R)$, the equation

$$\ddot{R}_s = \dot{R}_s \frac{d\dot{R}_s}{dR_s} \tag{C-13}$$

can be used to eliminate $\ddot{R}_s$. Assuming that $\gamma \sim 1$ in Eq. (C-2), and substituting this and Eq. (C-13) into Eq. (C-11) yields

$$p(0,t) = \rho\dot{R}_s^2 + \frac{\dot{R}_s}{R_s^2}\frac{d\dot{R}_s}{dR_s} M = \frac{1}{2MR_s^2}\frac{d}{dR_s}(\dot{R}_s^2 M^2) \quad . \tag{C-14}$$

From Eq. (C-6),

$$\frac{d(\dot{R}_s^2 M^2)}{dR_s} = \frac{3(\gamma - 1)M}{2\pi R_s} E_s \quad , \tag{C-15}$$

which gives

$$\dot{R}_s^2 = \frac{3(\gamma - 1)E_s}{2\pi M^2} \int_0^{R_s} \frac{M(s)}{s}\, ds \quad . \tag{C-16}$$

The lower limit is zero because, for small enough R_s, ρ is approximately constant and Eq. (C-16) then becomes $\dot{R}_s^2 \propto E_s/\rho R_s^3$. This is in agreement with the Taylor-von Neumann-Sedov solution for an instantaneous point energy release in a uniform atmosphere, as it should be.

The target mass M_T is assumed to have an arbitrary density distribution out to radius R_1 and to be surrounded by air of uniform density ρ_o. Fuchs defines a physically descriptive radius R_o; this is the "excess material" radius related to M_T by the expression $M_T = 4\pi\rho_o (R_o^3 + R_1^3)/3$. Then, for $s \geq R_1$,

$$M(s) = \int_0^s \rho(r) r^2 dr = \frac{1}{3} \rho_o (s^3 + R_o^3) \qquad \text{(C-17)}$$

at $t = 0$, $s = 0$, so that

$$\frac{1}{3} \rho_o R_o^3 = \int_0^{R_1} [\rho(r) - \rho_o] r^2 dr \quad . \qquad \text{(C-18)}$$

Substituting Eq. (C-18) for $t > 0$ into Eq. (C-17) and the result into the integral of Eq. (C-16) gives

$$\int_0^{R_s} \frac{M(s)}{s} ds = \frac{1}{9} \rho_o R_s^3 + \int_0^{R_s} \frac{ds}{s} \int_0^s [\rho(r) - \rho_o] r^2 dr \quad . \qquad \text{(C-19)}$$

Integration by parts yields

$$\int_0^{R_s} \frac{M(s)}{s} ds = \frac{1}{9} \rho_o R_s^3 + \frac{1}{3} \rho_o R_o^3 (\ell n R_s - \ell n \bar{R}) \quad , \qquad \text{(C-20)}$$

where

$$\ell n \bar{R} \equiv \frac{\int_0^{R_1} \ell nr [\rho(r) - \rho_o] r^2 dr}{\int_0^{R_1} [\rho(r) - \rho_o] r^2 dr} \quad . \qquad \text{(C-21)}$$

Using Eq. (C-20) in Eq. (C-16) gives

$$\dot{R}_s^2 = \frac{3E_s(\gamma - 1)}{2\pi \rho_o R_s^3} f^2(R_s) \quad , \qquad \text{(C-22)}$$

with

$$f^2(R_s) = \frac{1 + 3(R_o/R_s)^3 \, \ell n(R_s/\bar{R})}{[1 + (R_o/R_s)^3]^2} \quad . \tag{C-23}$$

For large R_s, $f^2(R_s)$ goes to 1 and Eq. (C-22) reduces to the approximate solution for a point explosion in a uniform atmosphere derived by Bethe. Chapter II uses Chernyi's approximate solution to assign an E_s at later times, when the effect of the mass is no longer important. Chernyi's thin-shell approximation does not explicitly assume $\gamma = 1$, as was done by Bethe, and therefore the numerical constants differ slightly between the two approximations. To be consistent, we will normalize Eq. (C-22) at large radii to Chernyi's solution. That is,

$$\dot{R}_s^2 = \left(\frac{2}{5}\right)^2 \frac{1}{\xi} \left(\frac{E_s}{\rho_o}\right) R_s^{-3} \, f^2(R_s) \quad , \tag{C-24}$$

where ξ is defined in Eq. (II-7). The t-vs-R_s relation is obtained from

$$t = \int_0^{R_s} \frac{1}{\dot{R}_s(r)} \, dr = \frac{5}{2} \left(\xi \, R_o^5 \frac{\rho_o}{E_s}\right)^{1/2} \int_0^Z \frac{1 + z'^3}{\sqrt{z'^3 + 3 \, \ell n(z'/Z_o)}} \, dz' \tag{C-25}$$

where $Z = R_s/R_o$ and $Z_o = \bar{R}/R_o$. This converges to Chernyi's solution for large Z. The denominator of the integrand is imaginary for small z'. The lower limit must therefore be taken to be slightly greater than zero, representing only a small error in t.

☆U.S. GOVERNMENT PRINTING OFFICE: 1982-0-576-020/26

Printed in the United States of America
Available from
National Technical Information Service
US Department of Commerce
5285 Port Royal Road
Springfield, VA 22161
Microfiche $3.50 (A01)

Page Range	Domestic Price	NTIS Price Code	Page Range	Domestic Price	NTIS Price Code	Page Range	Domestic Price	NTIS Price Code	Page Range	Domestic Price	NTIS Price Code
001-025	$ 5.00	A02	151-175	$11.00	A08	301-325	$17.00	A14	451-475	$23.00	A20
026-050	6.00	A03	176-200	12.00	A09	326-350	18.00	A15	476-500	24.00	A21
051-075	7.00	A04	201-225	13.00	A10	351-375	19.00	A16	501-525	25.00	A22
076-100	8.00	A05	226-250	14.00	A11	376-400	20.00	A17	526-550	26.00	A23
101-125	9.00	A06	251-275	15.00	A12	401-425	21.00	A18	551-575	27.00	A24
126-150	10.00	A07	276-300	16.00	A13	426-450	22.00	A19	576-600	28.00	A25
									601-up	†	A99

† Add $1.00 for each additional 25-page increment or portion thereof from 601 pages up.

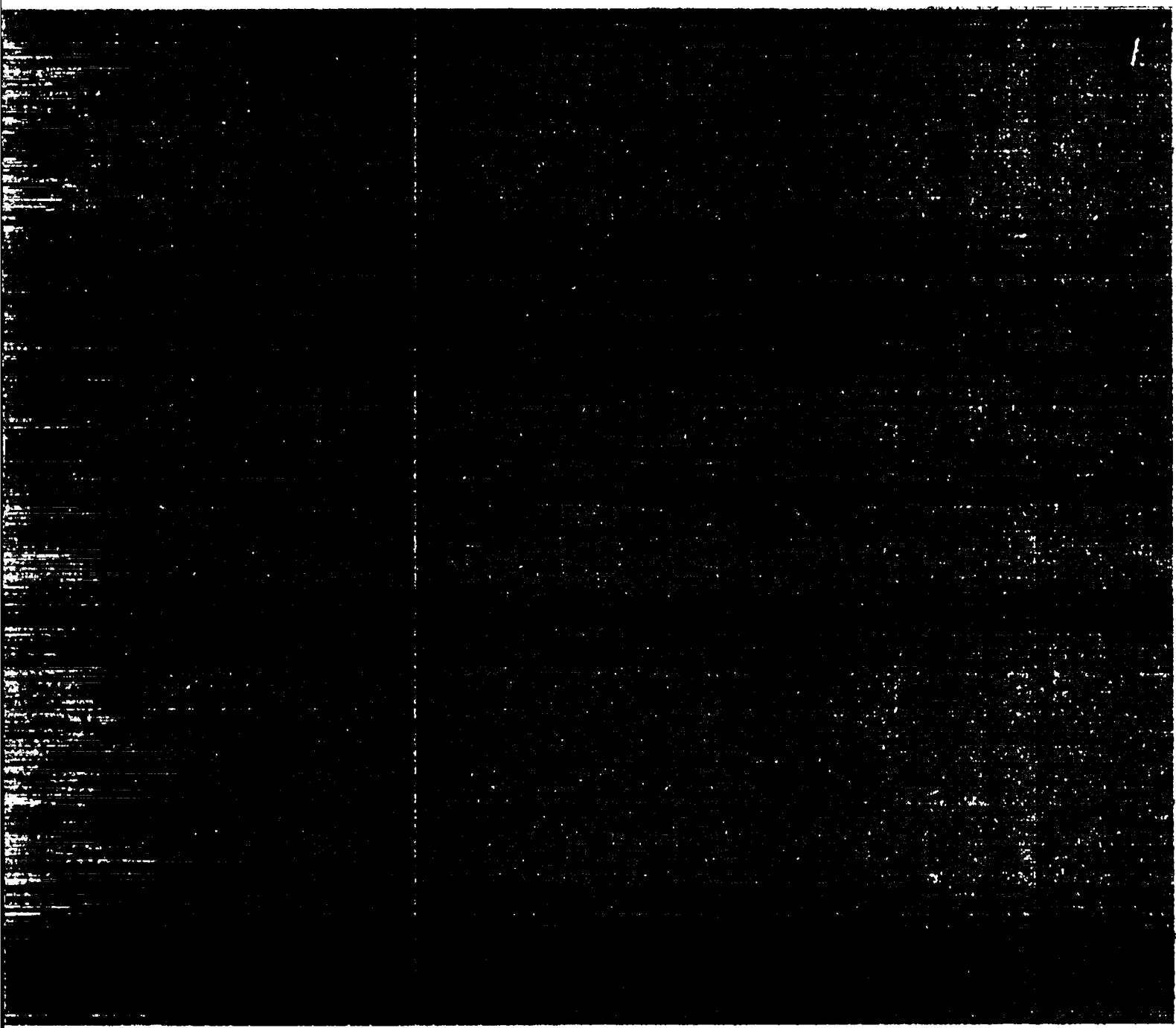

Los Alamos